Development of Multi-pass Thomson Scattering System with Delay Mechanism of Laser Pulses for Measuring Anisotropy of Electron Velocity Distribution Function on Heliotron J

（ヘリオトロンＪにおける電子速度分布関数の非等方性を観測するためのレーザーパルスの遅延機構を有するマルチパストムソン散乱システムの開発）

Dechuan Qiu

Abstract

In this thesis, a design of dual scattering angles multi-path Thomson scattering system with a signal separation function to solve the overlapping phenomenon of scattered light signals and increase the measurement accuracy for the investigation of anisotropic electron velocity distribution is proposed on Heliotron J. The design of the Multi-pass Thomson scattering system is based on the polarization control technique and developed from the original single-pass Thomson scattering system on Heliotron J, which includes the polarization optical system, trigger system, image relay system, and spectroscopic system. Except for the conventional function of Multi-pass Thomson scattering systems, this new system can solve the signal overlap problem existing on Heliotron J by its newly added signal separation system. Specifically, an optical path design is proposed to demonstrate how overlapping scattered light signals can be separated by setting the optical path in a limited room with a compact layout, which makes the incident interval between two overlapping scattered light signals 1.7 times longer than our current system. The specific position of each optical component existing in the system is determined via a Gaussian beam analysis to avoid damage caused by the over-expansion of spot size with the application of two cooperating image relay systems. Polychromators are optimized by resetting the pass waveband of the interference filter combination to reach high accuracy in electron temperature (T_e) measurement corresponding to two scattering angles simultaneously.

The phenomenon of overlapping scattered light signals is relieved by operating the signal separation system. A Raman scattering experiment is undertaken to verify the separation effect of the signal separation system. The incident interval between two scattered light signals corresponding to two adjacent incidences of one laser shot was extended to 104 ns. On the other hand, signal intensity is enhanced by the multi-pass operation. From the verification of

Raman scattering signals, at most 18 passes have been observed from a stray light signal, and signal intensity gets improved to over 2.5 times in a 4-pass operation. Moreover, we applied the multi-pass Thomson scattering system with the signal separation system to the electron temperature anisotropy measurement. No anisotropy was observed within the error bars in the initial experiment. These achievements will contribute to the design of multi-pass Thomson scattering systems for further anisotropy measurement.

Contents

Chapter 1
Introduction

1.1 Nuclear fusion

Power generated by nuclear fusion is a powerful source that may solve the energy problem of the world. Four realizable fusion reactions for the reactors are the following as[1,2]:

$$\mathrm{D} + \mathrm{T} \rightarrow {}^{4}\mathrm{He}(3.52\mathrm{MeV}) + \mathrm{n}(14.06\mathrm{MeV}) \quad (1.1)$$

$$\mathrm{D} + {}^{3}\mathrm{He} \rightarrow {}^{4}\mathrm{He}(3.67\mathrm{MeV}) + \mathrm{p}(14.67\mathrm{MeV}) \quad (1.2)$$

$$\mathrm{D} + \mathrm{D} \rightarrow {}^{4}\mathrm{He}(0.82\mathrm{MeV}) + \mathrm{n}(2.45\mathrm{MeV}) \quad (1.3)$$

$$\mathrm{D} + \mathrm{D} \rightarrow \mathrm{T}(1.01\mathrm{MeV}) + \mathrm{p}(3.03\mathrm{MeV}) \quad (1.4)$$

where *n*, *D*, and *T* stand for neutron, deuterium, and tritium. Among them, D-T fusion with the temperature required as $\sim 10\mathrm{keV}$ is expected to be adopted for fusion reactors because of their high-efficient rate of reaction. Deuterium is widely available by extracting

from seawater. However, tritium is few in the world. But it could still be generated within the fusion reactor by the reaction of lithium and neutrons. In nuclear fusion reactions, overcoming the Coulomb repulsion between ions is a crucial step. To realize this, the reacting particles must have large energy and a high probability of collision. The temperature needed is in the order of 10 keV, which leads the matter into a plasma state. For trapping the matter in a plasma state, many methods have been tried, such as magnetic confinement and inertial confinement. Magnetic confinement can trap the charged particles existing in a plasma along a produced magnetic field so that the high temperature of the plasma won't damage the vessel containing it. To sustain the fusion reaction without external heating, which means the energy produced by fusion surpasses the energy required to

sustain the plasma. This condition is expressed by the Lawson criterion, which states that the product of ion density and energy confinement time must exceed a critical value[3]. For the D-T reaction,

$$n_{\mathrm{i}} \times \tau_{\mathrm{E}} \geq 1.5 \times 10^{20} [\mathrm{s/m^3}] \tag{1.5}$$

where n_{i} is the ion density. The energy confinement time τ_{E} represents the time scale for the plasma to lose energy, and is defined as

$$\tau_{\mathrm{E}} = \frac{W}{P_{\mathrm{H}}} \tag{1.6}$$

where W is the energy stored in the plasma and P_{H} is the external heating power. In the field of magnetically confined plasma research, the generation of high-temperature and high-density plasmas is one of the main subjects.

1.2 Thomson scattering in nuclear fusion

Temperature anisotropy refers to the situation where the temperatures of plasma particles (such as electrons or ions) are not the same in all directions, leading to unequal thermal energies along different axes. In magnetized fusion plasma, the magnetic field plays a crucial role in maintaining plasma confinement. Temperature anisotropy can lead to differences in particle motion along and perpendicular to the magnetic field lines. This can create additional magnetic pressure gradients that interact with the plasma's equilibrium, potentially affecting the overall stability of the plasma. In addition, temperature anisotropy can affect the overall equilibrium conditions of a plasma. Anisotropic pressures contribute to the plasma's internal forces, which in turn influence the balance of forces and energy distribution within the plasma. Moreover, temperature anisotropy can have implications for plasma stability. In certain cases, large temperature anisotropies can lead to instabilities, where the plasma undergoes rapid and undesirable disruptions. These instabilities can alter the plasma's equilibrium configuration and lead to a loss of confinement or even a plasma disruption. Therefore, understanding

temperature anisotropy is crucial for achieving and maintaining stable and high-performance nuclear fusion plasmas.

As a diagnostic method, the Thomson scattering (TS) systems are capable of the measurement of plasma profiles such as electron temperature (T_e) and electron density (n_e), which are crucial for understanding plasma behavior, optimizing fusion performance, validating theoretical models, and implementing control strategies. The information of both T_e and n_e can be provided from the blue shift and intensity of the scattered light spectrum. Moreover, as an improved version compared with the conventional TS systems, the multi-pass Thomson scattering (MPTS) systems can enhance the signal intensity in a low-density measurement environment where scattered light is always too weak and corresponds to a poor signal-to-noise ratio. Besides, the MPTS systems are capable of measuring the T_e anisotropy, which can have significant effects on the behavior of a nuclear fusion plasma.

1.3 Survey of existing work

In the conventional single-pass Thomson scattering system, a laser beam is focused and guided into a plasma to produce scattered light and then collected by a beam dumper after passing through the plasma. Compared with single-pass Thomson scattering systems, MPTS systems can guide a laser beam into plasma more than once in one laser pulse. As a result, scattered radiation energy can be enhanced because photons of incident laser beam guided into plasma are repeatedly collected. Moreover, a laser beam can be guided into plasma from different directions by MPTS systems. The scattered light produced in this way can provide information on electron velocity distribution (EVD) corresponding to relative direction. With the merits of enhancing scattering photon numbers and being capable of measuring electron velocity distribution in different directions, MPTS

systems have been applied on many nuclear fusion devices, such as TEXTOR, GAMMA-10, and TST-2, for realizing different research purposes. MPTS scheme has been confirmed theoretically and experimentally that it has advantages in the measurement of low-density plasma environment and T_e anisotropy. Before MPTS systems were proposed, researchers also tried to realize anisotropic T_e measurement by the single-pass system. In the work of Broden et al, they measured temperature anisotropy by using a single-pass Thomson scattering in the low-density ECH plasma ($n_e \sim 10^{17} m^{-3}$). To realize the measurement of T_e reflected by different components of electron velocity distribution, the direction of the incident laser beam was changed in each shot. During their measurement, reproducible plasmas were produced to keep the reliability of the measurement because they can't realize the measurement of T_e corresponding to different components of electron velocity distribution in a short time interval. The T_e was measured both parallel and perpendicular to the magnetic field axis, and a small anisotropy of the electron velocity distribution was observed for low-pressure discharge conditions[4]. However, to realize such kind of measurement, beam alignment has to be done over once and so does the calibration work. Moreover, such kind of measurement can only be satisfied if the operation allows the ready accumulation of data. Therefore, The above two reasons have become limitations for applying this method in measurements of temperature anisotropy.

Kantor et al proposed and construct the MPTS systems on FT-2 tokamak and TEXTOR to increase the repetition frequencies of laser machines[5–7]. In their proposed MPTS system, the beam can be returned to the laser rod by a spherical mirror after the beam passes through the plasma volume. As a result, the optical connection between the laser rod and the multi-pass system forms a laser resonator cavity that contains the plasma volume inside it. In contrast to conventional TS systems, the radiation losses in this cavity can be significantly reduced

and the repetition frequency of laser passing through plasma has been enhanced from a few dozen Hz to around several kHz. Additionally, the multi-pass system allows for a manifold increase in the laser probing energy. The characteristic of this kind of system is that a slight relative shift of the centers of curvature along the observation axis appears as a larger pass number of the beam passes.

On the TST-2 spherical tokamak device, Ejiri et al developed a double-pass Thomson scattering system based on a confocal spherical mirror system[8–11]. The confocal mirror system consists of two concave mirrors with a common focal point and a common axis. Incident light parallel to the mirror axis will be reflected by the first mirror, passes through the focal point, and hits the second mirror. After hitting the second mirror, the light will be reflected and it becomes parallel to the mirror axis, then hits the first mirror. The above process continues and the light gradually approaches the mirror axis in this repeated process. In 2014, this system was developed into a MPTS system based on polarization control devices, which is familiar with the system developed on GAMMA 10[12,13].

On JT-60U, Hatae et al developed a double-pass Thomson scattering system and proposed a multi-pass Thomson scattering system with a core component as a phase conjugate mirror based on the stimulated Brillouin scattering[14,15]. Optical phase conjugation means the reversing of the phase front of the propagating light wave concerning the propagation direction. This means that the phase front of the reflected light is perfectly identical to the phase front of the incident light if the propagation direction is changed 180° in the phase conjugate mirror. The part of the nonlinear optical medium that causes phase conjugation is called a “phase conjugate mirror”. The phase conjugate mirror in the double-pass Thomson scattering system on JT-60U is filled with liquid named 3M Fluorinert, FC-75 in a glass tube of 300 mm in length and 40 mm in border surrounded by a stainless steel pipe with antireflection-coated windows at both ends. In this

system, a laser beam passing through the plasma is reflected by the phase conjugate mirror in place of a beam dumper of conventional single-pass Thomson scattering systems. The reflected beam passes the plasma again along the same path because of the phase conjugate effect. Compared with using a conventional mirror here, very precise beam alignment to let the beam return to a beam dumper is not necessary in the case of the phase conjugate mirror. After an initial simple positioning of the phase conjugate mirror, an alignment-free operation can be realized by the phase conjugate effect. The result shows that the phase conjugate mirror can achieve around 95% reflectivity at 145 W of a Nd:YAG laser during high-average power operation. Additionally, an increase of the scattered light by a factor of 1.6 compared with the single-pass scattering method in JT-60U is confirmed[15]. The relative error for the electron temperature was reduced by 2/3 in contrast to a single-pass scattering[14]. On the other hand, a MTPS system is proposed on JT-60U for more effective utilization of the laser beam energy. This MPTS system is an expansion of the previous double-pass system in that only an additional phase conjugate mirror, a thin film polarizer, and a large aperture Pockels cell are added. With these optical components added, the MPTS system is expected to generate scattered light more than twice the amount of the previous double-pass system by confining the laser beam between a pair of phase conjugate mirror. This new system also possesses the same advantages as the double-pass Thomson scattering system that alignment-free operation can be realized by the phase conjugate mirror after an initial adjustment. This new proposed system was not constructed before the cessation of the operation of JT-60U but it can be treated as the prototype of the MPTS system proposed on GAMMA-10 because only .

On GAMMA-10, Yasuhara and Yoshikawa et al proposed and constructed a MPTS system based on polarization control devices[16,17]. In this system, a laser beam of one laser shot is confined in a specific

optical path for several reciprocating trips within the operation period of a Pockels cell. During the reciprocating trips, the laser beam repeatedly passes through the plasma to produce scattered light within a coaxial optical path. The intensity of scattered light is gradually accumulated during this process, which brings about a higher signal-to-noise ratio. The experimental results on GAMMA 10 show that the integrated scattering signal of the double-pass configuration is about two times larger than that of the single-pass configuration, which demonstrates the improvement in the data quality of the GAMMA 10 TS system and the feasibility of the proposed polarization-based multi-pass system. In the Raman scattering experiment, a six-pass scattering signal is clearly observed that the measured scattering signal is proportional to the gas pressure and the integrated scattering intensity corresponding to the six-pass mode is about 3.5 times larger than that of the single-pass[18]. Because the intensity of not only the Thomson scattering signals but also Raman scattering signals corresponding to pass number more than 4 pass is relatively small, which means these signals can't make an effective contribution to enhancing the signal-to-noise ratio, in 2021, Yoshikawa et al develop a laser amplification system on GAMMA 10, for improving the degraded laser power and return an amplified laser to the MPTS system. In this case, scattered light signals can be obtained from the laser amplification system by improving the laser beam profile adjuster in gas scattering experiments[19]. The laser is introduced to the amplification system after the sixth pass through the laser beam profile adjuster. From the Raman scattering results, using the laser amplification after the sixth pass laser can produce a signal with intensity as high as that of the fifth pass signal. The amplification rates of signal intensity were calculated by dividing the integrated intensity of the total multi-pass signals with and without the amplification system by the integrated intensity of the first-pass signal. The calculated amplification rates were approximately 7.3 and 5.7, respectively. Moreover, the total signal

intensities were 1.6 times greater with the amplification system than without it.

From the development of the MPTS system shown above, it can be seen that in recent years, MPTS systems based on polarization-controlled devices become more and more dominant. Compared with the MPTS systems realized by other methods, MPTS systems realized by polarization-controlled technique have the unique advantage that the optical path can be realized in a coaxial path. Moreover, the beam alignment of such kind of system is not very complicated, and so is the calibration process. These advantages may be the driving force behind the increasing popularity of this system.

1.4 Objectives of this work

The single-pass Thomson scattering system on Heliotron J is initially constructed for the investigation of the effect of the control of the plasma profile in helical devices on improving plasma confinement[20,21]. The electron internal transport barrier has been successfully observed in Heliotron J in a low-density ECH plasma by this single-pass Thomson scattering system[22]. For a better understanding of equilibrium, instability, and turbulence in Heliotron J plasma, temperature anisotropy measurement is desirable. By analyzing the spectral density distribution function of scattered light, T_e can be interpreted because the profile of the spectral density distribution function is dependent on the scattering angle and T_e. More specifically, the spectral density distribution function reflects the projection of one component in three-dimensional electron velocity distribution (EVD) on the scattering plane; Generally, EVD is assumed as a Maxwellian distribution. However, EVD is expected to be anisotropic in strong electron heating experiments like ECH. Therefore, measurement of the anisotropic T_e profiles helps achieve a

complete understanding of the kinetic behavior of plasmas in such experimental conditions.

Benefiting from the coaxial optical path, polarization-based MPTS systems can provide scattered spectra reflecting two orthogonal components of EVD at the same measured position, which makes it more suitable for the investigation of anisotropy measurement. Although polarization-based MPTS has merit in anisotropy measurement, some problems exist. In the case of the MPTS system on Heliotron J that is constructed based on polarization-controlled devices, the obtained scattered light signals caused by two adjacent incidences almost completely overlap with each other due to the short incident interval as compared with the time constant of Avalanche photodiode (APD) output signal, which follows an exponential formation. Therefore, performing a separate analysis on a scattered light signal corresponding to one incident direction is impossible. Moreover, the spot size of the laser beam would undergo a significant expansion during the propagation along the optical path of a MPTS system because the optical path is extended compared with conventional single-pass systems. As a result, the expanded spot size will inflict damage on the fragile optical components when the diameter of the laser beam exceeds the entry size of these components. Finally, if the scattering angles corresponding to two opposite incident directions in a MPTS system are not equal, i.e., both scattering angles are not 90º, the profiles of scattering spectra corresponding to the two different scattering angles will increasingly differ from each other as T_e rises, due to a different blue shift trend caused by the magnitude of the scattering angle, which may decrease measurement accuracy and further hinder the observation of the anisotropic phenomenon. Studies on the effect of different blue shift trends on T_e measurement in MPTS systems are scarce.

The thesis is structured as follows:

In Chapter 2, the basic information of the helical-axis heliotron device Heliotron J where our MPTS system is prepared to install is described.

In Chapter 3, the basic theory of Thomson scattering is given.

In Chapter 4, the single-pass YAG-TS system in Heliotron J is described.

In Chapter 5, the detailed MPTS system design is given including the polarization optical system, trigger system, image relay system, and spectroscopic system.

In Chapter 6, the system performance is confirmed by a Raman scattering experiment. A first result of the anisotropy measurement in an ECH plasma is provided.

In Chapter 7, a concludion of this thesis is given.

Chapter 2
The Heliotron J Device

2.1 Introduction

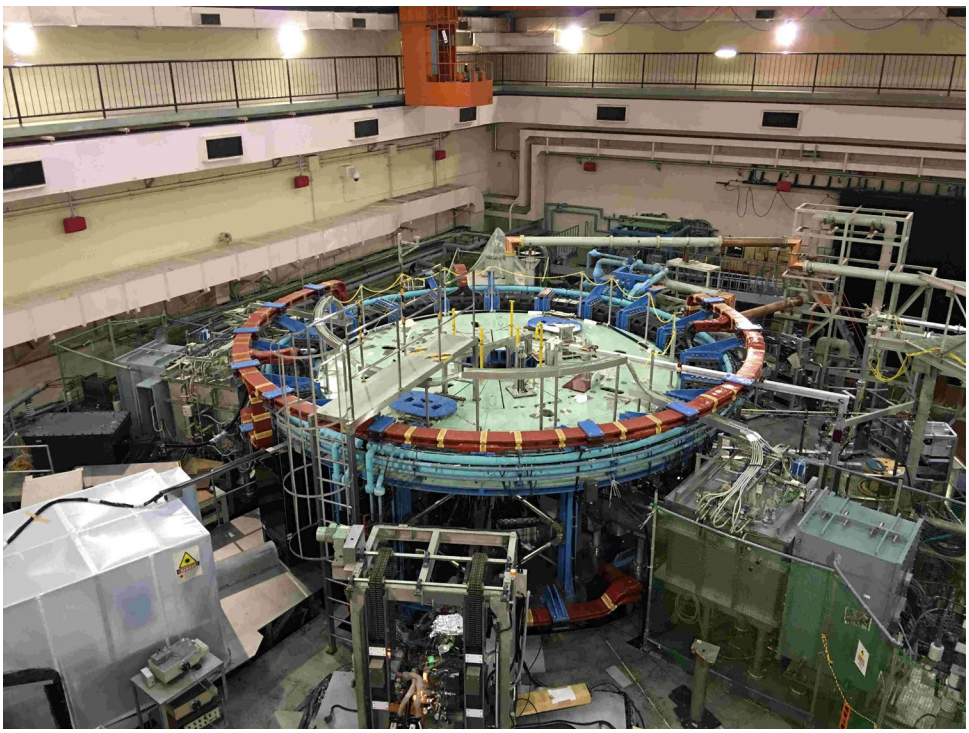

Figure 2.1 Heliotron J

Helical devices are a kind of magnetic confinement fusion device designed to produce a helical magnetic field configuration so that plasma discharges can be realized with better confinement and stability[23,24]. As a member of helical devices, Heliotron J at Kyoto University serves as a platform for testing and developing new technologies and materials for fusion reactors. Compared with its predecessor, Heliotron E[25], Heliotron J is larger with a major radius of 1.5 m, which affects the range of plasma densities and temperatures that can be achieved, as well as the level of magnetic field strength

that can be generated[26,27]. Moreover, a helical field is generated by an array of coils on Heliotron J, while Heliotron E uses a helical field generated by a single central coil. This difference in field generation can affect the stability and confinement of the plasma[28,29]. Figure 2.1 shows a schematic diagram of Heliotron J and main parameters of the device are listed in Table 2.1. The final goals of Heliotron J are as follows[28].

1 To optimize the helical-axis heliotron configuration.
2 To enhance MHD stability with good particle confinement.
3 A controllable particle and power-handling scheme.

In this chapter, the Heliotron J magnetic field is briefly described in section 3.2. In section 3.3, heating systems serving on Heliotron J are described. Lastly, diagnostics equipped on Heliotron J are listed in section 3.5.

Parameters	Values
Major Radius (R)	1.2 m
Plasma Minor Radius (a)	0.1-0.2 m
Vacuum Iota	~0.5 (flexible in 0.3 - 0.8)
Electron Temperature (T_e)	< 3 keV
Ion Temperature (T_i)	< 0.5 keV
Electron Density (n_e)	$< 1 \times 10^{20} \mathrm{m}^{-3}$

Table 2.1: Heliotron J plasma parameters

2.2 Magnetic Configurations

A variety of magnetic configurations can be realized on Heliotron by using its external coils. Schematic views of the vacuum chamber and the coils of Heliotron J are shown in Figure 2.2. Heliotron J can

constitute the local quasi-isodynamic configuration in the straight confinement section of the standard configuration. The magnetic field strength in the direction of the major radius is almost constant at the central cross-section of the straight section ($\phi = 45°$) while the magnetic field lines there are found to be nearly straight. As shown in figure 2.3, the collisionless orbits of the deeply-trapped particles in the inner side of the torus are on the magnetic flux surfaces, thus showing the local omnigenity.[28]

On the other hand, in order to test the predictions from the flow-based theories, e.g. testing the dependence of that quality on the neoclassical viscous damping in the collisional regime, as well as to optimize the turbulent transport of helical-axis heliotron[30,31], L–H transition is another key issue on Heliotron J. Figure 2.4 shows Magnetic surface structures of the edge rotational transform values $\iota(a)/2\pi$ = 0.493, 0.498, 0.56 and 0.62.

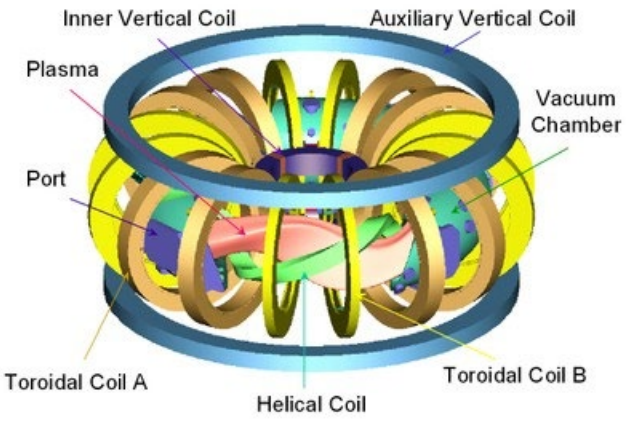

Figure 2.2 Schematic views of vacuum chamber and coils of Heliotron J.

2.3 Heating systems

Three heating systems are available in the current operation of Heliotron J, which are the electron cyclotron heating (ECH) system,

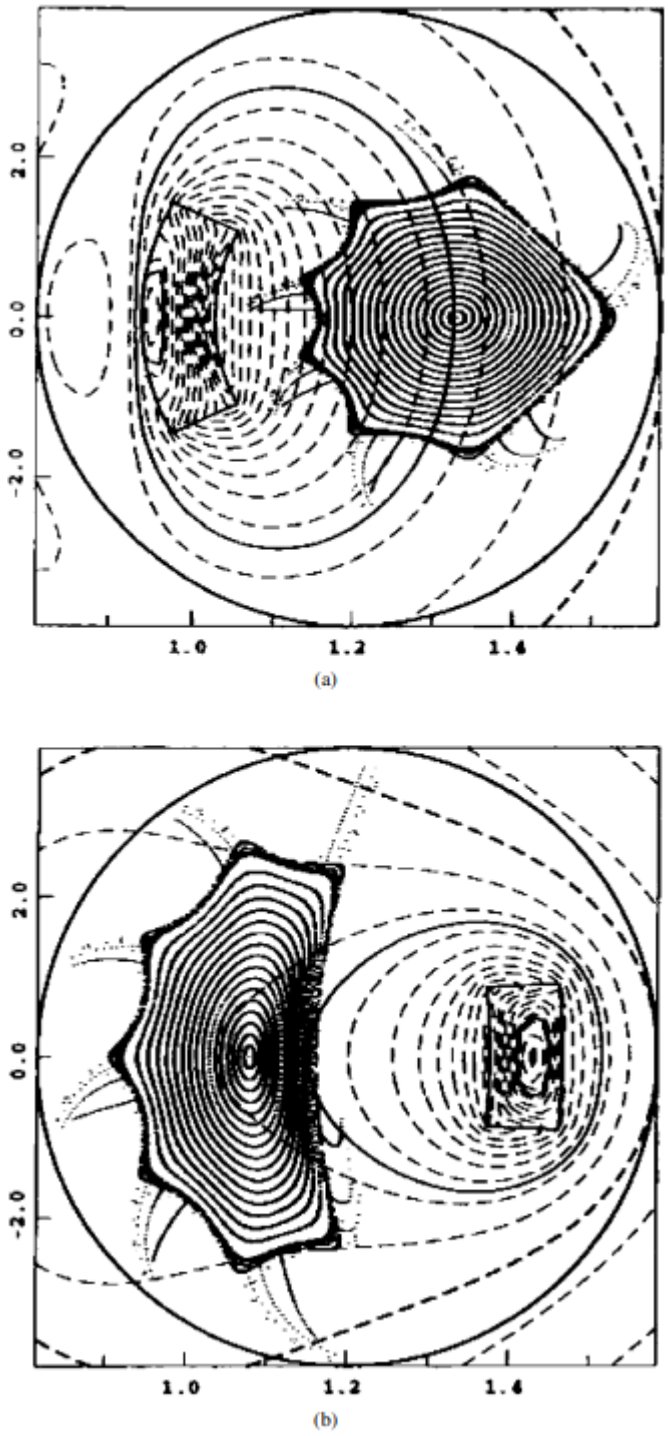

Figure 2.3 Poincare´ plots for the standard magnetic surfaces of Heliotron J: (a) corner section; (b) straight section[28].

neutral beam injection (NBI) system, and ion cyclotron range of frequencies (ICRF) system. The basic theory and information about them are given below. The positions corresponding to each heating

systems and diagnostics described in next section are demonstrated in Figure 2.5.

2.3.1 Electron cyclotron heating system

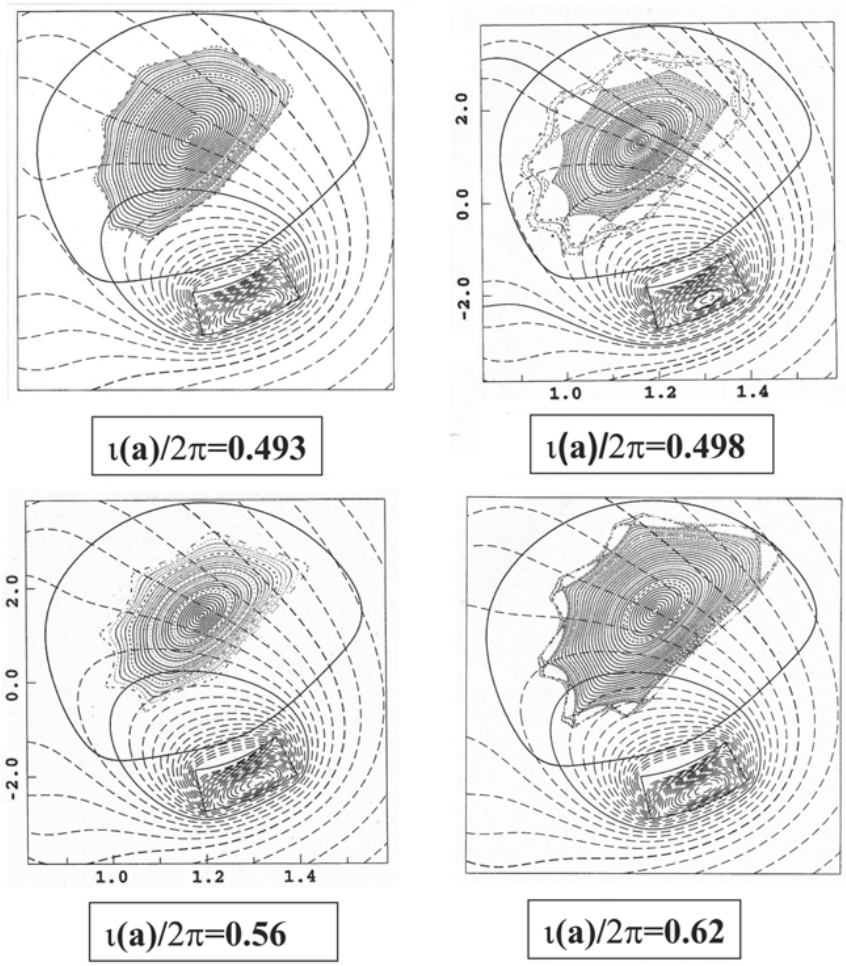

Figure 2.5. Magnetic surface structures of the edge rotational transform values $\iota(a)/2\pi$ = 0.493, 0.498, 0.56 and 0.62[30].

ECH systems work by launching electromagnetic waves at the plasma in the presence of a strong magnetic field, causing the electrons in the plasma to move in a circular path around the magnetic field lines. As the electrons move, they collide with other particles in the plasma, transferring their energy and increasing the temperature of the plasma. The ECH system uses microwaves with a frequency in the range of tens of GHz to penetrate the plasma and reach the desired region for

heating. These microwaves are generated by a high-power microwave source and then transmitted to the plasma through waveguides. The microwaves are then coupled to the plasma using a launcher, which directs the microwaves into the plasma in a controlled manner.

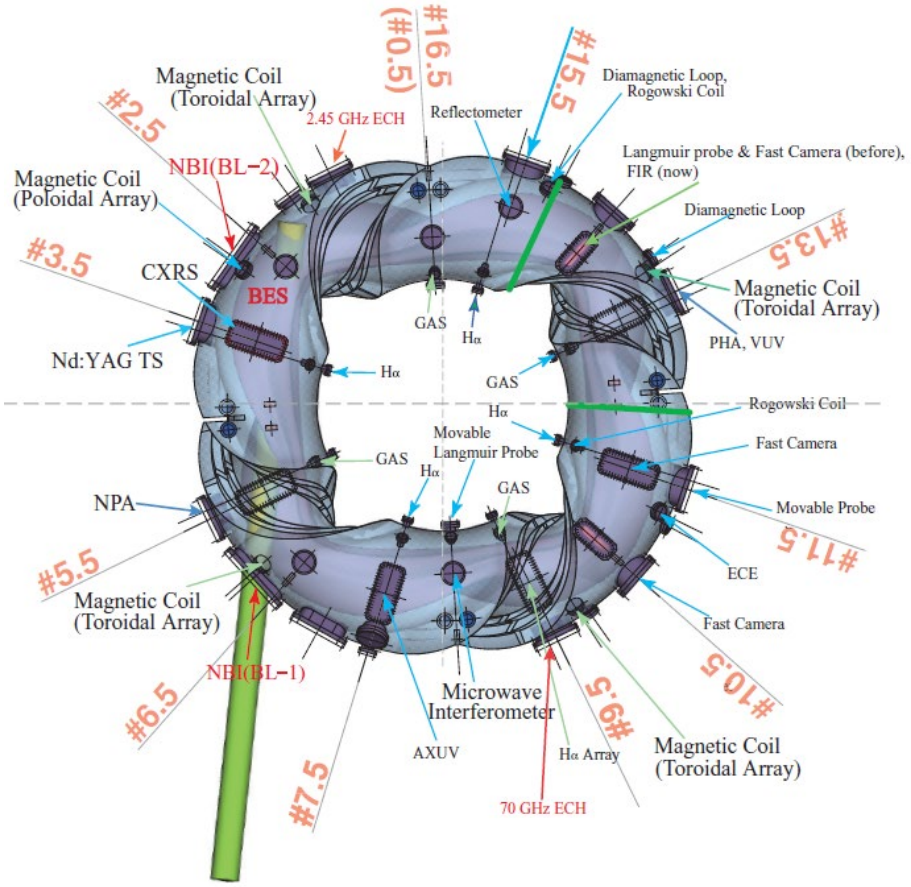

Figure 2.5. A top view of the vacuum vessel, plasma, heating systems and diagnostics of Heliotron J[33].

On Heliotron J, there's an ECH system consisting of a gyrotron, a matching optics unit, a transmission line, a Boron Nitride barrier window, and a launching system, as shown in Fig. 2.6. The gyrotron manufactured by GYCOM has an operational frequency of 70.0GHz, a maximum power of 600 kW at the output window, the pulse duration up to 500 ms and the Gaussian beam output mode[32].

2.3.2 Neutral beam injection system

NBI systems work by firing a beam of high-energy neutral particles, typically hydrogen or deuterium, into the plasma. The neutral particles penetrate deep into the plasma, where they undergo charge exchange reactions with the plasma ions, ionizing the neutral particles and transferring their energy to the plasma. The neutral beam injection system on Heliotron J consists of two tangential neutral beam lines. Each beamline has a maximum applied voltage of 30 keV and maximum injection power of 0.7MW, respectively[34].

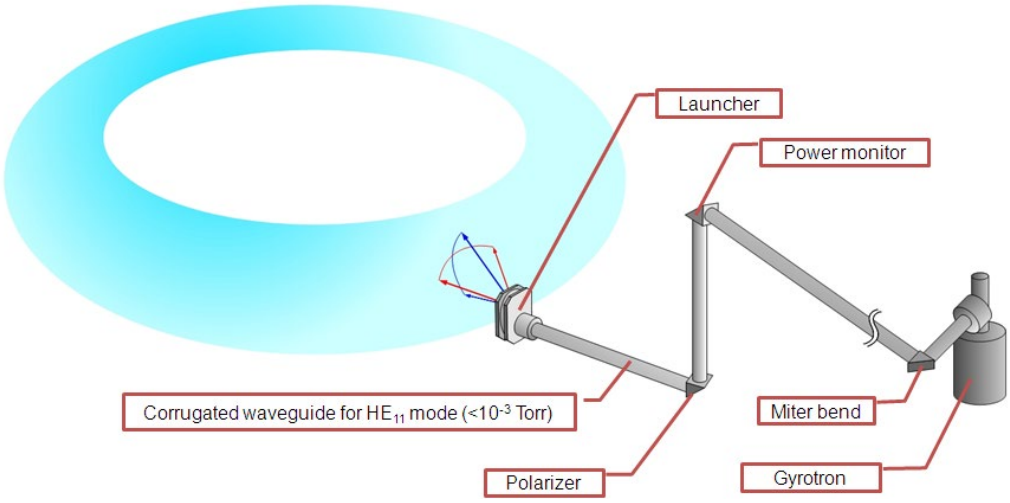

Figure 2.6. Schematic view of the 70GHz ECH system in Heliotron J.

2.3.3 Ion cyclotron range of frequencies system

ICRF is a type of radio-frequency (RF) heating working by transmitting RF waves into the plasma, which interact with ions that are in resonance with the frequency of the waves. The frequency range for ICRF heating is typically in the range of tens to hundreds of megahertz, which corresponds to the cyclotron frequency of ions in the plasma. The specific frequency used is determined by the type of ions present in the plasma and the strength of the magnetic field. The

frequency range of the system on Heliotron J is 17.8 MHz to 53.4 MHz with a maximum power output of 3 MW, and a pulse width of 0.2 s[35].

2.4 Diagnostics

Several diagnostics are equipped on Heliotron J and the positions of them are demonstrated in Figure 2.5. The information of some diagnostics are described below.

2.4.1 Microwave interferometer system

The line integrated density is measured by a ~320 GHz solid-state source microwave interferometer system. This interferometry system is of the Michelson type and is based on the heterodyne principle, with two independent solid-state sources that can deliver an output power of up to 50 mW. Its cutoff density is 1.27×10^{21} m^{-3}. A high time resolution measurement of $< 1\mu s$ can be derived by tuning the frequency of one source in the frequency range of 312-324 GHz on the new system, which can realize the fluctuation measurement. The submillimeter wave was transmitted to an optical bench through the waveguide and was injected into the plasma from the diagnostic port, passing through the mid-plane of the plasma[36,37].

2.4.2 Multi-channel electron cyclotron emission

A multi-channel electron cyclotron emission (ECE) radiometer system is being developed in Heliotron J to measure T_e profile and evaluate T_e fluctuation. The conventional ECE part of this system includes 16 channels and can measure electron temperature profile from 58GHz to 74GHz which covers from the core to the edge region, and the correlation ECE part is composed of CECE-RF and CECE-IF sides. The signals from these two sides share a same source of electron

cyclotron emission and thus are possible to estimate T_e fluctuation through correlation analysis[38].

2.4.3 multi-pass Thomson scattering system

T_e and n_e can be measured by a Thomson scattering system with multi-pass mode[20,39]. The profiles of them including 25 measurement positions can be measured by the scattered light produced by the interaction of the plasma and the incident yttrium aluminum garnet (Nd:YAG) Laser beam (500 mJ) guided from #3.5 port. In low *ne* conditions, this system can be changed into a multi-pass mode that can significantly enhance the signal-to-noise ratio, which overcomes the predicament of weak scattered light intensity under low-density conditions. The detail of this system and the development of this system will be specified in chapter 5.

2.4.4 Impurity measurements

Photon emissions from the plasma can be detected using various photon detectors, including the absolute extreme ultraviolet (AXUV) photodiode, which is capable of detecting photons over a wide range of energy. The line emissions, such as the Hα line, can be measured using a visible spectrometer.

Chapter 3
Thomson scattering theory

3.1 Introduction

In plasma physics research, Thomson scattering (TS) is widely used in nuclear fusion devices as a powerful and non-perturbing diagnostic technique. It can provide detailed information on the electron (or ion) density, electron (or ion) velocity distribution, and hence electron temperature (T_e). In addition, a non-perturbing feature that only light enters the plasma provides the non-invasive essential to avoid disturbing the plasma[40]. The theory of Thomson scattering can be briefly summarized as an acceleration of a free electron by the incident field of a light wave and the subsequent re-radiation by the electron of electromagnetic radiation into other directions. The incident light is normally realized by a high-energy laser beam, which imparts an oscillation to the plasma electrons at the frequency of the probing beam. The interaction between electrons and the incident light causes the electrons to undergo acceleration as the subsequence of oscillation and therefore leads to the emission of electromagnetic radiation. By analyzing the scattered light as the electromagnetic radiation from the electrons interacting with the probing light, relative information on the temperature of electrons and densities can be revealed.

In this chapter, TS theory is described, starting with how to define Thomson scattering is discussed in section 3.2. The acceleration of a particle caused by an electromagnetic wave with consideration of special relativity is discussed in section 3.3. In section 3.4, the radiation of an accelerated particle is in detail discussed. The standard

geometry of Thomson scattering is discussed in section 3.5. With all the information discussed above, the information given by a single electron or an assemble of electrons in a scattering volume with a Maxwellian electron velocity distribution is provided in sections 3.5 and 3.6 in sequence.

3.2 Principle of Thomson Scattering

The condition that can let Thomson scattering be satisfied is detailed in this section, which can also be used to explain the non-perturbing feature of this diagnostic. When an electric and magnetic field of an electromagnetic wave interacts with a charged particle, the particle accelerates and emits electromagnetic radiation in a dipole pattern. If the particle is moving in the field of the wave, the scattered frequency of the electromagnetic radiation will be Doppler shifted, which is caused by two effects. The first effect is that the moving particle will experience the incident wave at a different frequency than the input wave. The second effect is that the scattered radiation from a particle measured by an observer will also be Doppler-shifted due to the particle's motion. From the perspective of the principles of momentum, the momentum of the scattered wave may be changed after the scattering and so the momentum of the particle may also be changed to conserve total momentum[41]. The momentum and the energy imparted to the particle from the electromagnetic wave can be used to judge the changes in the particle. We assume the input wave is in the form of photons, the particle is initially at rest and the scattering takes place in a plane. The scattering is schematically shown in Fig. 3.1. Here Ψ and φ are the angles at that the particle recoils and photon scatters, respectively.

The energies of the photon shown in Fig. 3.1 before and after the collision are assumed as E_p and E_p', respectively. Here we assume the particle is an electron at rest. p_e is the momentum of the electron

following the collision. The energy of the electron in this case can be expressed as:

$$E_e = \sqrt{(p_e c)^2 + (m_0 c^2)^2} \tag{3.1}$$

where m_0 is the rest mass of the electron and c is the velocity of light. If the scattering process between the photon and the electron can be treated as an elastic collision holds true in this context, based on the conservation of momentum

$$\frac{E_p}{c} = \frac{E_p'}{c}\cos\varphi + p_e \cos\Psi \tag{3.1}$$

$$0 = \frac{E_p'}{c}\sin\varphi - p_e \sin\Psi \tag{3.2}$$

and the conservation of energy

$$E_p + m_0 c^2 = E_p' + \sqrt{(p_e c)^2 + (m_0 c^2)^2}. \tag{3.3}$$

The energy of the scattered photon following the collision can be deduced as

$$E_p' = \frac{E_p m_0 c^2}{m_0 c^2 + E_p(1-\cos\varphi)}. \tag{3.4}$$

Consequently, the energy obtained by the electron as the energy lost by the photon is

$$E_p - E_p' = \left(\frac{E_p^2}{m_0 c^2}\right)\frac{1-\cos(\varphi)}{1+\frac{E_p(1-\cos(\varphi))}{m_0 c^2}}. \tag{3.5}$$

When the E_p is relatively negligible to the rest energy of the electron, the electron's momentum does not significantly change as a result of the collision. When the above condition is met as the photon energy is negligible to the electron's energy, which can be expressed as $E_p \ll m_0 c^2$, it's termed 'Thomson scattering'. It's also represented as the low-energy limit of the Compton effect for scattering. When this condition is not satisfied, and the photon energies can no longer be ignored, it is called Compton scattering. In typical Thomson scattering systems, lasers are used with photon energies up to six orders of magnitude less than the rest energy of the plasma electron. Therefore, the incident light wave does not significantly alter the electron path.

At the other extreme, Compton scattering applies when the photon energy is comparable to the rest energy of the electron.

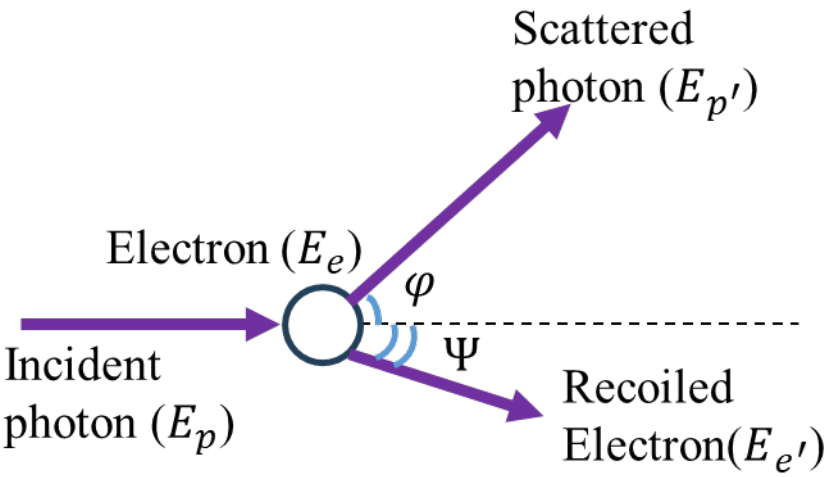

Fig 3.1: Compton scattering.

3.3 Acceleration of an electron in an electromagnetic field

Accelerated charged particles emit electromagnetic radiation whose radiated electric and magnetic fields can be determined from the Lienard–Wiechert potentials. In order to determine the radiation from an accelerated particle as a result of a laser beam traversing it, it's necessary to know the acceleration acquired by the particle[42]. The equation of motion of an electron within a time-varying electric and magnetic field is firstly considered to evaluate the electron acceleration caused by the electric and magnetic fields of the incident laser beam. In this case, using Newton's Second Law of Motion, the equation of the electron's motion can be written as

$$\frac{dm}{dt} = -e(\vec{E}_i + \vec{v} \times \vec{B}_i) \tag{3.6}$$

where $\vec{E}_i$ and $\vec{B}_i$ are the electric and magnetic fields of the incident light wave, respectively. e is the magnitude of the charge on the electron[43]. m is the mass of the electron with consideration of the

increase in the electron's mass with velocity ($\vec{v}$) in the special theory of relativity, namely,

$$m = \frac{m_0}{\sqrt{1-\frac{v^2}{c^2}}} \tag{3. 7}$$

where m_0 is the rest mass of the electron and c is light speed.

Substituting Equation (3. 8) into Equation (3.7) and let $\vec{\beta} = \vec{v}/c$, we can have

$$m_0 \frac{\mathrm{d}}{\mathrm{d}t}\left[\vec{\beta}(1-\beta^2)^{-\frac{1}{2}}\right] = -e\left(\frac{\vec{E}_i}{c} + \vec{\beta} \times \vec{B}_i\right). \tag{3. 8}$$

Carrying out the differentiating, we have

$$m_0\gamma\vec{\beta} + m_0\gamma^3\vec{\beta}(\beta\dot{\beta}) = -e\left(\frac{\vec{E}_i}{c} + \vec{\beta} \times \vec{B}_i\right) \tag{3. 9}$$

where the dot on $\vec{\beta}$ indicates the time derivative and $\gamma = \frac{1}{\sqrt{1-\frac{v^2}{c^2}}}$.

Calculating the electron acceleration $\dot{\vec{\beta}}$ of Equation (3. 10), the following is obtained,

$$\dot{\vec{\beta}} = -\frac{e}{m_0\gamma}\left\{\frac{\vec{E}_i}{c} - \left(\frac{\vec{\beta}\cdot\vec{E}_i}{c}\right)\vec{\beta} + \vec{\beta} \times \vec{B}_i\right\}. \tag{3. 10}$$

As shown in figure 3.,2 if the time-varying electric and magnetic field of the incident light wave obeys a plane-wave electromagnetic propagation, the B-fields can be expressed by E-field due to the relationship[44] between H-field and E-field, according to

$$\vec{H}_i = \frac{\vec{k}_i \times \vec{E}_i}{\mu_0\omega_i} \tag{3. 11}$$

where $\vec{k}_i$ is the propagation vector in the direction $\hat{\imath}$, $\mu_0 = 4\pi \times 10^{-7}\mathrm{Hm}^{-1}$ and ω_i is the radian frequency of the incident light wave. The wave vector showing the propagation of wave is given by $\vec{k}_i = \frac{\omega_i}{c}\hat{\imath}$. According to $\vec{B}_i = \mu_0\vec{H}_i$, we can have the following result,

$$\vec{B}_i = \frac{1}{c}\hat{\imath} \times \vec{E}_i. \tag{3. 12}$$

Substituting (3. 13) into equation (3. 11) and considering vector identity $\vec{A} \times (\vec{B} \times \vec{C}) = (\vec{A} \cdot \vec{C})\vec{B} - (\vec{A} \cdot \vec{B})\vec{C}$, we have

$$\dot{\vec{\beta}} = -\frac{e}{m_0 c\gamma}\{\vec{E}_i - (\vec{\beta}\cdot\vec{E}_i)\vec{\beta} + \hat{\imath}(\vec{\beta}\cdot\vec{E}_i) - \vec{E}_i(\vec{\beta}\cdot\hat{\imath})\}. \quad (3.\ 13)$$

Equation demonstrates that all terms on the right-hand side are related to $\vec{E}_i$, which means the acceleration is absolutely along the E-field of the incident light wave. Furthermore, when the speed of an electron is much smaller than the velocity of light, equation (3. 14) can be reduced to the formation suitable to the classical Newtonian spacetime view

$$\dot{\vec{\beta}} = -\frac{e}{m_0 c\gamma}\vec{E}_i. \quad (3.\ 14)$$

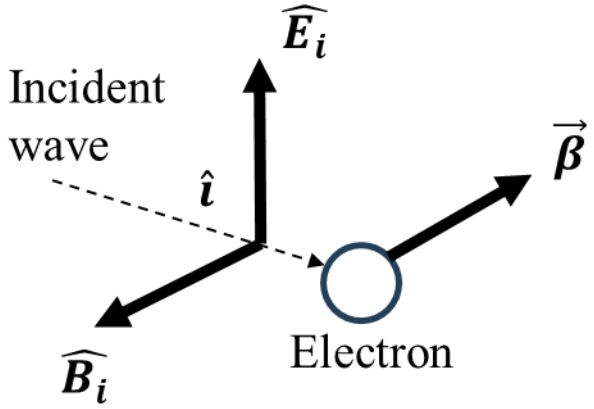

Figure 3.2: Schematic diagram showing the interaction between the incident light wave and the moving electron.

3.4 Radiation by accelerated charges

To detect electromagnetic radiation from an accelerated particle, it's desirable to determine the properties of the electromagnetic radiation, such as the formation of the radiated electromagnetic wave and the radiated energy. Here we first deduce the formation and energy of the radiated electromagnetic wave from an accelerated particle and, thereafter, we deduce them from a scattering volume containing N particles.

In the beginning, we start from the deduction of radiation power from a single particle under acceleration. It is assumed that the position

where the scattered radiation is detected is located at a remote position with respect to the position of the particle.

The radiated power of an accelerated particle is related to its Poynting vector. Instantaneous Poynting vector for the scattered radiation from an accelerated particle can be written as

$$\vec{S}_s(\vec{r},t) = \vec{E}_s(\vec{r},t) \times \vec{H}_s(\vec{r},t) \qquad (3.\ 15)$$

where $\vec{E}_s(\vec{r},t)$ and $\vec{H}_s(\vec{r},t)$ are the E-field and H-field of the scattered radiation at the observation position at time *t*.

The electric $\vec{E}_s(\vec{r},t)$ and magnetic $\vec{H}_s(\vec{r},t)$ fields are derived from the scalar and vector potentials, $\phi(\vec{r},t)$ and $\vec{A}(\vec{r},t)$ according to

$$\vec{E}(\vec{r},t) = -\vec{\nabla}\phi(\vec{r},t) - \frac{\partial \vec{A}(\vec{r},t)}{\partial t} \qquad (3.\ 16)$$

$$\vec{B}(\vec{r},t) = \vec{\nabla} \times \vec{A}(\vec{r},t) \qquad (3.\ 17)$$

$$\vec{B}(\vec{r},t) = \mu_0 \vec{H}(\vec{r},t) \qquad (3.\ 18)$$

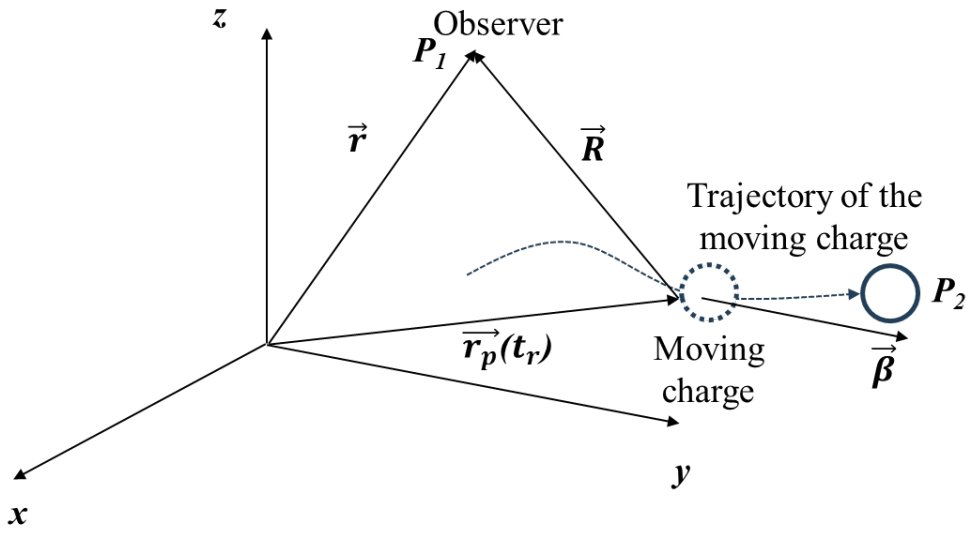

Figure 3.3: The path of the moving charge distribution.

Therefore, the goal of solving the solution of equation (3. 16) becomes getting the solution of the scalar and vector potentials. However, to a point charge with the volume approaching zero and moving along the trajectory $\vec{r}_p$ with velocity $\vec{v}$ as shown in Fig. 3.3,

the scalar potential $\phi(\vec{r},t)$ and vector potential $\vec{A}(\vec{r},t)$ recorded at time t at the observation point depends on what has occurred at an earlier time t_r at the position of the electron $\vec{r}_p(t_r)$. The reason is that the scalar potential $\phi(\vec{r},t)$ and vector potential $\vec{A}(\vec{r},t)$ satisfy the inhomogeneous wave equations within the Lorentz gauge, and therefore, the speed of their transmission is the velocity of light[45]. In this case, it takes a period for the information to transit from the source to the observer. The detail to prove that the scalar potential $\phi(\vec{r},t)$ and vector potential $\vec{A}(\vec{r},t)$ satisfy the inhomogeneous wave equations is given below.

$$\frac{\rho}{\epsilon_0} = \vec{\nabla}\cdot\vec{E} = \vec{\nabla}\cdot\left(-\vec{\nabla}\phi - \frac{\partial\vec{A}}{\partial t}\right) = -\vec{\nabla}^2\phi - \frac{\partial}{\partial t}\vec{\nabla}\cdot\vec{A}$$
$$\xrightarrow{\text{Lorentz gauge}} -\vec{\nabla}^2\phi - \frac{\partial}{\partial t}\left(-\frac{1}{c^2}\frac{\partial\phi}{\partial t}\right),$$

where ρ is the distribution of the charge density and ϵ_0 is the permittivity of free space. Using the Lorentz gauge, we can write

$$\vec{\nabla}^2\phi - \frac{1}{c^2}\frac{\partial^2\phi}{\partial t^2} = -\frac{\rho}{\epsilon_0},$$

which means the scalar potential ϕ satisfies the inhomogeneous wave equation. On the other hand, with $\vec{\nabla}\times\vec{H} = \vec{J} + \frac{\partial\vec{D}}{\partial t}$ and the constitutive equation $\vec{H} = \frac{\vec{B}}{\mu}$, we have

$$\vec{\nabla}\times\frac{\vec{B}}{\mu_0} - \frac{\partial}{\partial t}\left(\epsilon_0\vec{E}\right) = \vec{J} \rightarrow \vec{\nabla}\times\frac{\vec{B}}{\mu_0\epsilon_0} - \frac{\partial\vec{E}}{\partial t} = c^2\vec{\nabla}\times\vec{B} - \frac{\partial\vec{E}}{\partial t} = \frac{\vec{J}}{\epsilon_0},$$

where μ and μ_0 are magnetic constant and vacuum magnetic constant, respectively. $\vec{J}$ is the current density. $\vec{D}$ is electric displacement. $\vec{B}$ and $\vec{H}$ are the magnetic induction and magnetic field strength, respectively. Substituting ϕ and $\vec{A}$ into the above equation, we have

$$c^2\vec{\nabla}\times\vec{\nabla}\times\vec{A} - \frac{\partial}{\partial t}\left(-\vec{\nabla}\phi - \frac{\partial\vec{A}}{\partial t}\right) \xrightarrow{\vec{\nabla}\times(\vec{\nabla}\times\vec{A})=\vec{\nabla}(\vec{\nabla}\cdot\vec{A})-\vec{\nabla}^2\vec{A}} c^2\vec{\nabla}(\vec{\nabla}\cdot\vec{A}) -$$
$$c^2\vec{\nabla}^2\vec{A} + \frac{\partial}{\partial t}\vec{\nabla}\phi + \frac{\partial^2\vec{A}}{\partial t^2} = \frac{\vec{J}}{\epsilon_0}.$$

Using the Lorentz equation $\vec{\nabla}\cdot\vec{A}+\frac{1}{c^2}\frac{\partial\phi}{\partial t}=0$, the above equation can be written as

$$c^2\vec{\nabla}\left(-\frac{1}{c^2}\frac{\partial\phi}{\partial t}\right)-c^2\vec{\nabla}^2\vec{A}+\frac{\partial}{\partial t}\vec{\nabla}\phi+\frac{\partial^2\vec{A}}{\partial t^2}=-c^2\vec{\nabla}^2\vec{A}+\frac{\partial^2\vec{A}}{\partial t^2}=\frac{\vec{J}}{\epsilon_0}$$

$$\vec{\nabla}^2\vec{A}-\frac{1}{c^2}\frac{\partial^2\vec{A}}{\partial t^2}=-\frac{\vec{J}}{c^2\epsilon_0}=-\mu_0\vec{J},$$

which means the vector potential $\vec{A}$ also satisfies the inhomogeneous wave equation. Therefore, it takes a finite time of $\left|\vec{r}-\vec{r}_p(t_r)\right|/c$ for the electromagnetic signal to arrive at the observer. t_r is equal to the quantity $t-\frac{|\vec{r}-\overrightarrow{r_p}(t_r)|}{c}$. Under this circumstance, the scalar and vector potentials at the observation point are

$$\phi(\vec{r},t)=\iiint\frac{\rho(\overrightarrow{r\prime},t_r)}{4\pi\varepsilon_0|\vec{r}-\overrightarrow{r\prime}|}d^3r' \qquad (3.\ 19)$$

and

$$\vec{A}(\vec{r},t)=\iiint\frac{\mu_0\vec{J}(\overrightarrow{r\prime},t_r)}{4\pi|\vec{r}-\overrightarrow{r\prime}|}d^3r' \qquad (3.\ 20)$$

respectively, where ρ is the distribution of the charge density and $\vec{J}=\rho v$ is the current density of the charge density distribution. v is the velocity of the charge density distribution. t_r is called the retarded time. *r'* is the integral variant, which is with respect to the position of the source charge.

At time *t* when the signal arrives at the observation point P_1 to record the potentials, the charge has already moved to a new position P_2 described as $\overrightarrow{r_p}(t)$. Because the time for a light signal propagating from one position to another is not infinite, different spatial parts of the charge distribution must emit their signals at different retarded times in order that these signals can arrive at the observation point at the same time t. This effect is also applied to a point charge. To a point charge with charge *e*, here are a lot of methods to deal with the right-hand side of equations (3. 20) and (3. 21) into the formation at the retarded time. Dirac delta function is adopted in the method mentioned in [46] to make a variable change. Taylor expansion is used in the

method mentioned in reference[47]. Geometry is used in the Methods mentioned in the reference[48]. Here we adopt the Dirac delta function to rewrite equations (3. 20) and (3. 21).

Based on the sifting property of the Dirac delta function, as shown in equation (3. 22),

$$\int_{-\infty}^{\infty} f(t)\delta(t-T)\mathrm{d}t = f(T). \qquad (3.\ 21)$$

By writing T as $t - \frac{|\vec{r}-\overrightarrow{r_p}(t_r)|}{c}$, the charge density $\rho(\vec{r},t)$ can be written as

$$\rho\left(\overrightarrow{r'},t_r\right) = q\delta(\overrightarrow{r'} - \overrightarrow{r_p}(t_r))^3\delta(t_r - t + \frac{|\vec{r}-\overrightarrow{r_p}(t_r)|}{c}). \qquad (3.\ 22)$$

Here term $\overrightarrow{r_p}(t_r)$ is the term T mentioned in equation (3. 22) to sift the variables $\overrightarrow{r'}$, respectively.

Substituting equation (3.23) into equation (3. 20), we have

$$\phi(\vec{r},t) = \int \oiint\!\!\!\oint \frac{q\delta(\overrightarrow{r'}-\overrightarrow{r_p}(t_r))^3\delta(t_r-t+\frac{|\vec{r}-\overrightarrow{r_p}(t_r)|}{c})}{4\pi\varepsilon_0|\vec{r}-\overrightarrow{r_p}(t_r)|} d^3r'dt_r. \qquad (3.\ 23)$$

Firstly, q and the denominator are taken out of the integrand of the volume integral because $\left|\vec{r} - \overrightarrow{r_p}(t_r)\right| = \{[x - r_{px}(t_r)]^2 + [y - r_{py}(t_r)]^2 + [z - r_{pz}(t_r)]^2\}^{1/2}$ can be treated as a function of t_r, which is independent to r'. The remained volume integral is $\oiint\!\!\!\oint \delta(\overrightarrow{r'} - \overrightarrow{r_p}(t_r))^3 d^3r'$ equal to 1 and equation (3. 24) can be written as

$$\phi(\vec{r},t) = q\int \frac{\delta(t_r-t+\frac{|\vec{r}-\overrightarrow{r_p}(t_r)|}{c})}{4\pi\varepsilon_0|\vec{r}-\overrightarrow{r_p}(t_r)|} dt_r. \qquad (3.\ 24)$$

It should be emphasized that the variable change is necessary here because the vector $\overrightarrow{r_p}$ is a function of the retarded time variable. Therefore, the integrand that appears in equation (3. 25) cannot yet be evaluated. A new variable t'' to be equal to the argument of the delta function is defined here:

$$t'' \equiv t_r - t + \frac{|\vec{r}-\overrightarrow{r_p}(t_r)|}{c} \qquad (3.\ 25)$$

Equation (3. 26) can be further differentiated and because t is the fixed time at the observation position as $dt = 0$, we have

$$dt'' = \left\{1 + \frac{1}{c}\frac{d}{dt_r}\left|\vec{r} - \overrightarrow{r_p}(t_r)\right|\right\} dt_r \quad (3.\ 26)$$

The quantity $\left|\vec{r} - \overrightarrow{r_p}(t_r)\right|$ is just

$$\left|\vec{r} - \overrightarrow{r_p}(t_r)\right| = \sqrt{\sum_i \left(x_i - x_{e,i}(t_r)\right)^2} \quad (3.\ 27)$$

Where x_i and $x_{e,i} = x_{e,i}(t_r)$ are coordinate components of the position of observation at the time t_r and source at time *t*, respectively. The subscript *i* corresponds to three directions orthogonal with each other, which are *x, y,* and *z* in the Cartesian coordinate system. x_i are fixed because they represent the coordinate components of the fixed observation position. Here although $\left|\vec{r} - \overrightarrow{r_p}(t_r)\right|$ is a function with an implicit dependence of t_r through the $x_{e,i}(t_r)$, these three coordinate components are explicit functions of t_r. Therefore, the derivative of $\left|\vec{r} - \overrightarrow{r_p}(t_r)\right|/c$ concerning t_r is

$$\frac{1}{c}\frac{d}{dt_r}\left|\vec{r} - \overrightarrow{r_p}(t_r)\right| = \frac{1}{c}\sum_i \left(\frac{\partial}{\partial x_{e,i}}\left|\vec{r} - \overrightarrow{r_p}(t_r)\right|\right)\frac{dx_{e,i}}{dt_r} \quad (3.\ 28)$$

or

$$\frac{1}{c}\frac{d}{dt_r}\left|\vec{r} - \overrightarrow{r_p}(t_r)\right| = \frac{1}{c}\left(\mathrm{grad}_{r_p}\left|\vec{r} - \overrightarrow{r_p}(t_r)\right|\right) \cdot \frac{d\overrightarrow{r_p}(t_r)}{dt_r} \quad (3.\ 29)$$

where the subscript r_p on the gradient operator signifies that the derivatives are to be taken with respect to the coordinates of the charge. Hence, the gradient operation may be expressed as

$$\mathrm{grad}_{r_e}\left|\vec{r} - \overrightarrow{r_p}(t_r)\right| = -\frac{\vec{r} - \overrightarrow{r_p}(t_r)}{\left|\vec{r} - \overrightarrow{r_p}(t_r)\right|} = -\frac{\vec{R}}{R} \quad (3.\ 30)$$

The vector difference between the position vector of the observation position and the particle position is defined as $\vec{R}$ and its magnitude is *R*, respectively. Because the derivative of $\overrightarrow{r_p}(t_r)$ with respect to t_r is just the particle's velocity $\overrightarrow{u_p}(t_r)$. If we define $\vec{\beta}(t_r) \equiv \frac{1}{c}\frac{d\overrightarrow{r_p}(t_r)}{dt_r} \equiv \overrightarrow{u_p}(t_r)/c$, equation (3. 30) becomes

$$\frac{1}{c}\frac{d}{dt_r}\left|\vec{r} - \overrightarrow{r_p}(t_r)\right| = -\frac{\vec{\beta}(t_r) \cdot \vec{R}(t_r)}{R(t_r)}. \quad (3.\ 31)$$

Therefore, the right side of equation (3. 27) can be written as

$$dt'' = dt_r\left(1 - \frac{\vec{\beta}(t_r)\cdot\vec{R}(t_r)}{R(t_r)}\right). \tag{3. 32}$$

On the other hand,

$$dt_r = \frac{R(t_r)}{R(t_r) - \vec{\beta}(t_r)\cdot\vec{R}(t_r)}\,dt''. \tag{3. 33}$$

Based on the relationship between t_r and t'' defined in equation (3.26) as the change of variable, equation (3.25) for the scalar potential $\phi(\vec{r}, t)$ becomes

$$\begin{aligned}\phi(\vec{r}, t) &= q\int \frac{\delta\left(t_r - t + \frac{\left|\vec{r} - \overrightarrow{r_p}(t_r)\right|}{c}\right)}{4\pi\varepsilon_0\left|\vec{r} - \overrightarrow{r_p}(t_r)\right|}\,dt_r \\ &= \frac{q}{4\pi\varepsilon_0}\int_{-\infty}^{+\infty}\frac{\delta(t'')}{R(t_r)}\left(\frac{R(t_r)}{R(t_r) - \vec{\beta}(t_r)\cdot\vec{R}(t_r)}\right)dt''.\end{aligned} \tag{3. 34}$$

Due to the sifting property of the delta function, the truth of t'' equal to 0, and the coincidence of the variable of the integrand, equation (3.35) becomes

$$\phi(\vec{r}, t) = \frac{q}{4\pi\varepsilon_0[R(t_r) - \vec{\beta}(t_r)\cdot\vec{R}(t_r)]}\Big|_{t''=0}. \tag{3. 35}$$

Obviously, $t'' = 0$ implies $t_r = t - R(t_r)/c$, the retarded time. Thus

$$\phi(\vec{r}, t) = \frac{q}{4\pi\varepsilon_0}\left[\frac{1}{R - \vec{R}\cdot\vec{\beta}}\right]_{\text{ret}} \tag{3. 36}$$

where the subscript ret indicates that all quantities within the square bracket are evaluated at the retarded time t_r. The corresponding equation for the vector potential can be obtained in the same way, which is given by

$$\vec{A}(\vec{r}, t) = \frac{\mu_0 q}{4\pi}\left[\frac{\vec{v}}{R - \vec{R}\cdot\vec{\beta}}\right]_{\text{ret}}. \tag{3. 37}$$

Equations (3.37) and (3.38) are the Lienard-Wiechert potentials for a moving point charge. These two equations still hold true under the view of special relativity[49]. In addition, equations (3.37) and (3.38) can also be proved that they are indeed the solutions to the inhomogeneous wave equations for the potentials[46].

With the potentials produced by the source at the retarded time, the electric $\vec{E}_s(\vec{r}, t)$ and magnetic $\vec{H}_s(\vec{r}, t)$ fields mentioned in equations

(3.17) and (3.19) can be deduced. Before doing that, it should be noticed that the gradient operator $\vec{\nabla}$ before scalar potential and the partial derivatives of the vector potential are taken at constant time t instead of constant t_r in equations (3.17) and (3.19). Nevertheless, these potentials are produced by the source at an earlier time t_r, which means these partial derivatives should be converted from the time *t* to the time t_r, e.g. from $\left(\frac{\partial}{\partial t}\right)_{x,y,z}$, $\left(\frac{\partial}{\partial x}\right)_{y,z,t}$, $\left(\frac{\partial}{\partial y}\right)_{x,z,t}$, and $\left(\frac{\partial}{\partial z}\right)_{y,z,t}$ to quantities in terms of $\left(\frac{\partial}{\partial t_r}\right)_{x,y,z}$, $\left(\frac{\partial}{\partial x}\right)_{y,z,t_r}$, $\left(\frac{\partial}{\partial y}\right)_{x,z,t_r}$, and $\left(\frac{\partial}{\partial z}\right)_{y,z,t_r}$.[48]

The conversions of partial derivatives at time *t* to retarded time t_r are made before determining the electric and magnetic fields. Two types of conversion need to be done here, which are the time derivatives and the gradient operators. To figure out the conversion, variable *R* may be the key here because it's related to not only the coordinate components of vector positions but also the time variables *t* and t_r. In the other words, *R* can be written as a function of *x*, *y*, *z* and t_r due to $R = \left|\vec{r} - \vec{r}_p(t_r)\right| = \left[\left(x - x_p(t_r)\right)^2 + \left(y - y_p(t_r)\right)^2 + \left(z - z_p(t_r)\right)^2\right]^{\frac{1}{2}}$ expanded from equation (3.28). Meanwhile, from $t - t_r = \frac{R}{c} \equiv \frac{R(x,y,z,t_r)}{c}$ we can say t_r is a function of *t* when the position of observation is fixed, as $t_r \equiv t_r(t)$. This conclusion can be proven by a reductio ad absurdum as follow. If two sources located at $\vec{r}_{p1}$ and $\vec{r}_{p2}$ can produce the potential at time *t* simultaneously, we can have $c(t - t_{r1})\widehat{R_1} = \overrightarrow{R_1}$ and $c(t - t_{r2})\widehat{R_2} = \overrightarrow{R_2}$, respectively. $\overrightarrow{R_1}$ and $\overrightarrow{R_2}$ are vectors pointing from sources 1 and 2 to the position of observation, respectively. $\widehat{R_1}$ and $\widehat{R_2}$ are the corresponding unit vectors. By combining them, we can have $c(t_{r2} - t_{r1})\widehat{R_1 - R_2} = \overrightarrow{R_1} - \overrightarrow{R_2}$, which means the information transmitted along the direction of $\widehat{R_1 - R_2}$ have a velocity of *c*. Nevertheless, the information transmitted along $\widehat{R_1}$ and $\widehat{R_2}$ have

already had the velocity of c. Because nothing can acquire a speed over light in the view of special relativity, only one source can transmit information to the position of observation at a specific time, e.g. the function $t - t_r = \frac{R(x,y,z,t_r)}{c}$ is injective when x, y, and z are fixed. Hence, t_r can be written as a function of t as $t_r \equiv t_r(t)$, and vice versa.

Based on the relationship given by R, the conversion of the time derivative and the gradient operators from t to t_r are deduced in sequence. Regarding the time derivative, the relationship between the partial derivatives of time t and retarded time t_r can be determined if the other two quantities, $\left(\frac{\partial R}{\partial t}\right)_{x,y,z}$ and $\left(\frac{\partial R}{\partial t_r}\right)_{x,y,z}$ are given in equation (3.39).

$$\left(\frac{\partial R}{\partial t}\right)_{x,y,z} = \left(\frac{\partial R}{\partial t_r}\frac{\partial t_r}{\partial t}\right)_{x,y,z}. \tag{3.38}$$

To the left-hand side of the equation, since $R = c(t - t_r)$, differentiating it towards time t can give out

$$\left(\frac{\partial R}{\partial t}\right)_{x,y,z} = c\left[1 - \left(\frac{\partial t_r}{\partial t}\right)_{x,y,z}\right]. \tag{3.39}$$

On the other hand,

$$\begin{aligned}\left(\frac{\partial R}{\partial t_r}\right)_{x,y,z} = \ & \frac{1}{2}\left[(x - x_p)^2 + (y - y_p)^2\right. \\ & \left.+(z - z_p)^2\right]^{-\frac{1}{2}}\left[-2(x - x_p)\frac{\partial x_p}{\partial t_r}\right. \\ & \left.-2(y - y_p)\frac{\partial y_p}{\partial t_r} - 2(z - z_p)\frac{\partial z_p}{\partial t_r}\right]\end{aligned} \tag{3.40}$$

which means it can be written as,

$$\left(\frac{\partial R}{\partial t_r}\right)_{x,y,z} = -\frac{\vec{R}\cdot\vec{v}}{R}, \tag{3.41}$$

where $\vec{v} = \partial\vec{r}_p(t_r)/\,\partial t_r$ is the velocity of the charged particle. Substituting equations (3.40) and (3.42) into equation (3.39), we have

$$\left(\frac{\partial t_r}{\partial t}\right)_{x,y,z} = \frac{R}{R - \vec{R}\cdot\vec{\beta}}. \tag{3.42}$$

Defining

$$\kappa \equiv R - \vec{R}\cdot\vec{\beta}, \tag{3.43}$$

we have

$$\left(\frac{\partial}{\partial t}\right)_{x,y,z} = \frac{R}{\kappa}\left(\frac{\partial}{\partial t_r}\right)_{x,y,z}, \tag{3. 44}$$

which is the conversion of the time derivative from *t* to t_r.

To convert the gradient operators partially differentiating at *t* to the one partially differentiating at t_r, we can still use *R* which has a relationship with every variable corresponding to the observation position and the source. By calculating the gradient of *R*, we have

$$\vec{\nabla}R\big|_t = \vec{\nabla}c(t - t_r)\big|_t = -c\vec{\nabla}t_r\big|_t, \tag{3. 45}$$

By substituting $dR(x, y, z, t_r)$, $dt_r(x, y, z, t)$ and the expansion of $\vec{\nabla}R\big|_t$ into equation (3.47), we have

$$\vec{\nabla}R\big|_t = \vec{\nabla}R\big|_{t_r} - \frac{\vec{R}}{\kappa c}\left(\frac{\partial R}{\partial t_r}\right)_{x,y,z}. \tag{3. 46}$$

Extract the gradient operator from both sides of equation (3.47) and the conversion of the gradient operator from *t* to t_r is obtained as the following form.

$$\vec{\nabla}_t = \vec{\nabla}_{t_r} - \frac{\vec{R}}{\kappa c}\frac{\partial}{\partial t_r}. \tag{3. 47}$$

Substituting equations (3.45) and (3.48) into the expression of Lienard-Wiechert potentials, namely, equations (3.37) and (3.38), we have

$$\begin{aligned}\vec{E}(\vec{r}, t) = \; & \frac{q}{4\pi\varepsilon_0}\left[\frac{1}{(1-\vec{\beta}\cdot\hat{s})^3}(\vec{R} - R\vec{\beta})(1-\beta^2)\right]_{\text{ret}} \\ & + \frac{q}{4\pi\varepsilon_0}\left[\frac{1}{(1-\vec{\beta}\cdot\hat{s})^3 c^2}\vec{R}\times(\vec{R} - R\dot{\vec{\beta}})\times\vec{v}\right]_{\text{ret}}\end{aligned}, \tag{3. 48}$$

$$\vec{B}(\vec{r}, t) = -\{\vec{R}\times\frac{q}{4\pi\varepsilon_0 c^2\kappa^3}\times\left[(1-\beta^2)\vec{v} + \kappa\dot{\vec{\beta}} + \left(\vec{R}\cdot\dot{\vec{\beta}}\right)\vec{\beta}\right]\}_{ret}, \tag{3. 49}$$

where all quantities within square brackets and curly braces are evaluated at the retarded time t_r, hence, the subscript *ret*. Specifically, to the scattered electric field from the retarded potential, The first term is inversely proportional to the square of the distance *R*, while the second term is inversely proportional to the first power of *R*. Consider

a huge sphere of radius r'', the surface area of the sphere is proportional to r''^2. So any terms in the Poynting vector $\vec{S} = \frac{1}{\mu_0}(\vec{E} \times \vec{B}) = \frac{1}{\mu_0 c}[\vec{E} \times (\hat{\imath} \times \vec{E})] = \frac{1}{\mu_0 c}\left[E^2\hat{\imath} - (\hat{\imath} \cdot \vec{E})\vec{E}\right]$ that goes like $1/r''^2$ will yield a finite answer, but terms like $1/r''^3$ or $1/r''^4$ will contribute nothing to the limit $r'' \to \infty$. The first term in equation (3.49) carries energy as the charge moves this energy is dragged along, but it's not radiation. Only the latter term in equation (3.49) represents true radiation, which depends on the acceleration of the charge and, hence, constitutes the radiation field which is given by

$$\vec{E}_s(\vec{r}, t) = \frac{q}{4\pi\varepsilon_0}\left[\frac{1}{\tilde{\kappa}^3 Rc}\hat{s} \times (\hat{s} - \vec{\beta}) \times \dot{\vec{\beta}}\right]_{\text{ret}}. \qquad (3.50)$$

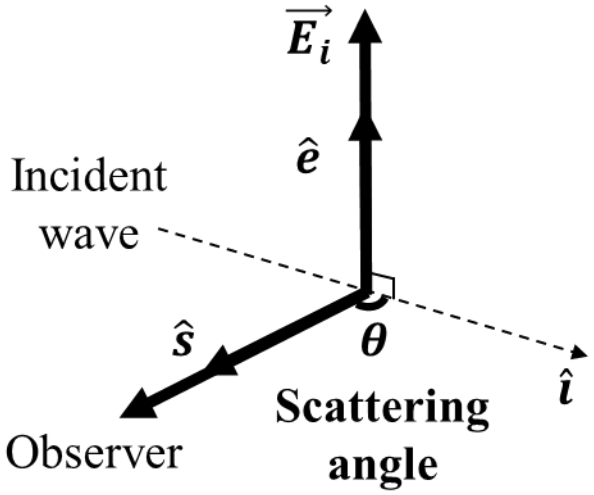

Figure 3.4: The incident electric field $\vec{E}_i$ is perpendicular to the scattering plane, that is, the plane defined by $\hat{\imath}$ and $\hat{s}$.

Besides, it can be found that a relationship exists between equations (3.49) and (3.50), namely,

$$\vec{B}(\vec{r}, t) = \frac{1}{c}\frac{\vec{R}}{R} \times \vec{E}(\vec{r}, t). \qquad (3.51)$$

After obtaining the retarded fields given by equations (3.49) and (3.50), the instantaneous Poynting vector describing the energy radiated by the particle at a moment *t* can be deduced by following equation (3.16)

$$\vec{S}_s(\vec{r},t) = \vec{E}_s(\vec{r},t) \times \vec{H}_s(\vec{r},t) = \frac{1}{\mu_0 c} E_s(\vec{r},t)^2 \hat{s}. \quad (3.52)$$

The magnitude of the instantaneous Poynting vector describing the rate of energy transfer per unit area per unit time is

$$S_s(t) = \frac{1}{\mu_0 c} E_s^2(\vec{r},t) = c\varepsilon_0 E_s^2(\vec{r},t). \quad (3.53)$$

Furthermore, to an observer of the position $\vec{r}$, the energy flowing through an area $\mathrm{d}A = R^2 \mathrm{d}\Omega$ in the direction $\hat{s}$ and received by this observer during a time interval $\mathrm{d}t$ is

$$\begin{aligned} d^2E &= \left(\vec{E}_s(\vec{r},t) \times \vec{H}_s(\vec{r},t)\right) \cdot \hat{s} R(t_r)^2 \, d\Omega dt \\ &= \frac{q^2}{16\pi^2 \varepsilon_0 c} \left[\frac{\{\hat{s} \times (\hat{s} - \vec{\beta}) \times \dot{\vec{\beta}}\}^2}{(1 - \vec{\beta} \cdot \hat{s})^6}\right]_{ret} d\Omega dt. \end{aligned} \quad (3.54)$$

where $\vec{\beta} = \vec{v}/c$. $\mathrm{d}\Omega$ is the solid angle. The direction $\hat{s}$ is as same as $\vec{R}(t_r)$. It can be seen that in equation (3.55) the term *dt* describing the time interval is still evaluated by the observer. If this time interval *dt* can be converted to dt_r, the right-hand side of equation (3.55) can be unified. Here we repress the equation (3.55) as

$$d^2E = \frac{q^2}{16\pi^2 \varepsilon_0 c} \left[\frac{\{\hat{s} \times (\hat{s} - \vec{\beta}) \times \dot{\vec{\beta}}\}^2}{(1 - \vec{\beta} \cdot \hat{s})^6}\right]_{ret} d\Omega \frac{dt}{dt_r} dt_r \quad (3.56)$$

Substituting the reciprocal of equation (3.43) into equation (3.56), the energy radiated per unit solid angle in a time interval dt_r can be written as the following equation

$$d^2E = \frac{q^2}{16\pi^2 \varepsilon_0 c} \left[\frac{\{\hat{s} \times (\hat{s} - \vec{\beta}) \times \dot{\vec{\beta}}\}^2}{(1 - \vec{\beta} \cdot \hat{s})^6}\right] d\Omega \times (1 - \vec{\beta} \cdot \hat{s}) dt_r \quad (3.57)$$

Compared with equation (3.55), here all quantities at the right-hand side are evaluated at the charge's own time t_r. Hence, the power P radiated by the charged particle in terms of the particle's own time t_r is given by

$$P = \frac{q^2}{16\pi^2 \varepsilon_0 c} \int \frac{|\hat{s} \times (\hat{s} - \vec{\beta}) \times \dot{\vec{\beta}}|^2}{(1 - \vec{\beta} \cdot \hat{s})^5} d\Omega. \quad (3.58)$$

The power radiated per unit solid angle is given by

$$\frac{dP}{d\Omega} = \frac{q^2}{16\pi^2 c \varepsilon_0} \frac{1}{(1 - \beta \cos\theta_1)^5} |\hat{s} \times (\hat{s} - \vec{\beta}) \times \dot{\vec{\beta}}|^2. \quad (3.59)$$

Here θ_1 is the angle between $\vec{\beta}$ and $\hat{s}$.

3.5 Typical scattering geometry

A usual scattering geometry normally satisfies the perpendicular between the scattering plane defined by $\hat{\imath}$ and $\hat{s}$ and the incident field vector $\vec{E}_i$, which is described by $\hat{s} \cdot \hat{e} = 0$, as shown in Fig. 3.4. From the scattered field

$$\vec{E}_s(\vec{r}, t) = \frac{q}{4\pi\varepsilon_0}\left[\frac{1}{\tilde{\kappa}^3 Rc}\hat{s} \times (\hat{s} - \vec{\beta}) \times \dot{\vec{\beta}}\right]_{\text{ret}},$$

as shown in equation (3.51) and the acceleration of a charged particle in an electromagnetic field

$$\dot{\vec{\beta}} = -\frac{e}{m_0 c\gamma}\{\vec{E}_i - (\vec{\beta} \cdot \vec{E}_i)\vec{\beta} + \hat{\imath}(\vec{\beta} \cdot \vec{E}_i) - \vec{E}_i(\vec{\beta} \cdot \hat{\imath})\},$$

as shown in equation (3.14), the expression of the scattered field can be expanded. It should be noted that four terms consist of the acceleration. The first is defined as the classical term, the second is defined as the relativistic term and the latter two terms are due to the B-field of the incident light wave. Here we investigate the formation of these four terms in sequence before further deducing scattered signals arising from several electrons within the scattering volume.

The classical term is proportional to the following one by using the so-called "back cab" role.

$$\hat{s} \times \left[(\hat{s} - \vec{\beta}) \times \vec{E}_i\right] = \hat{s} \times (\hat{s} \times \vec{E}_i) - \hat{s} \times (\vec{\beta} \times \vec{E}_i)$$

$$\xrightarrow{\vec{A}\times(\vec{B}\times\vec{C})=\vec{B}(\vec{A}\cdot\vec{C})-\vec{C}(\vec{A}\cdot\vec{B})} \hat{s}(\hat{s} \cdot \vec{E}_i) - \vec{E}_i(\hat{s} \cdot \hat{s}) - \vec{\beta}(\hat{s} \cdot \vec{E}_i) + \vec{E}_i(\hat{s} \cdot \vec{\beta})$$

If $\hat{e}$ is defined as a unit vector in the direction of the electric field vector, then $\vec{E}_i = E_i\hat{e}$ and the latter expression becomes

$$= E_i\hat{s}(\hat{s} \cdot \hat{e}) - E_i\hat{e} - E_i\vec{\beta}(\hat{s} \cdot \hat{e}) + E_i\hat{e}\beta_s$$

where $\beta_s \equiv (\hat{s} \cdot \vec{\beta})$ is the component of $\vec{\beta}$ along the scattering direction $\hat{s}$. For the usual scattering geometry where the $\hat{e}$ vector is perpendicular to the scattering plane, that is $\hat{s} \cdot \hat{e} = 0$, the latter expression is

$$= -E_i\hat{e}(1-\beta_s). \tag{3.60}$$

As a result, the scattered field vector is along the same direction as the incident field vector.

The relativistic term is dealt with the same way as

$$\hat{s}\times\left[\left(\hat{s}-\vec{\beta}\right)\times -\beta_e E_i\vec{\beta}\right] = -\beta_e E_i\left[\hat{s}\times\hat{s}\times\vec{\beta}-\hat{s}\times\vec{\beta}\times\vec{\beta}\right]$$
$$\xrightarrow{\vec{A}\times(\vec{B}\times\vec{C})=\vec{B}(\vec{A}\cdot\vec{C})-\vec{C}(\vec{A}\cdot\vec{B})} -\beta_e E_i\left[\beta_s\hat{s}-\vec{\beta}\right] \tag{3.61}$$

It can be seen these terms contribute to a component in the $\hat{s}$ direction and a component in the direction of the electron's velocity $\vec{\beta}$ to the scattered electric field.

Lastly, we expand the expression of B-field terms as the following equation with consideration of the usual scattering geometry that is $\hat{s}\cdot\hat{e}=0$.

$$\hat{s}\times\left[\left(\hat{s}-\vec{\beta}\right)\times\left\{\hat{\imath}\left(\vec{\beta}\cdot\vec{E}_i\right)-\vec{E}_i\left(\vec{\beta}\cdot\hat{\imath}\right)\right\}\right] = E_i\beta_e(\beta_s-1)\hat{\imath}+$$
$$E_i\beta_i(1-\beta_s)\hat{e}-\beta_e E_i\vec{\beta}\cos\,\theta+\beta_e E_i\hat{s}\cos\,\theta \tag{3.62}$$

Here θ is defined as the scattering angle between the vector $\hat{\imath}$ and $\hat{s}$. Equation (3.62) indicates the B-field terms contribute the components corresponding to four directions, e.g., $\hat{\imath}$, $\hat{e}$, $\hat{s}$ and $\vec{\beta}$.

From the expressions of the three terms mentioned above, it can be known the scattered electric field vector has components along the directions; $\hat{\imath},\hat{e},\hat{s}$ and $\vec{\beta}$. Collect the terms on the right-hand of equations (3.60), (3.61) and (3.62) and reexpress $\vec{E}_s(\vec{r},t)$ given in equation (3.51), the general formula of $\vec{E}_s(\vec{r},t)$ scattered by an electron is given as

$$\vec{E}_s(\vec{r},t) = \frac{e^2}{4\pi\epsilon_0 m_0 c^2}\left[\frac{E_i(1-\beta^2)^{\frac{1}{2}}}{R(1-\beta_s)^3}\{-(1-\beta_i)(1-\beta_s)\hat{e}\right.$$
$$-\beta_e(1-\beta_s)\hat{\imath}\}$$
$$+(\{1-\beta_i\}\hat{s}\cdot\hat{e}+\{\hat{s}\cdot\hat{\imath}-\beta_s\}\beta_e)\hat{s}$$
$$\left.-(\{1-\beta_i\}\hat{s}\cdot\hat{e}-\{1-\hat{s}\cdot\hat{\imath}\}\beta_e)\vec{\beta}\right]_{ret} \tag{3.63}$$

In the majority of experimental set-ups, a polarizer with transmission direction parallel to the component in the direction of $\hat{e}$ is normally

utilized. Under this circumstance, only that component of the scattered wave $\vec{E}_s(\vec{r},t)$ parallel to ê is selected. With the existence of such kind of polarizer, equation (3.63) is simplified to

$$\vec{E}_s(R,t) = \frac{e^2}{4\pi\varepsilon_0 m_0 c^2}\hat{e}\left[\frac{E_i}{\gamma(1-\beta_s)^3 R}\{(1-\beta_i) \times (1-\beta_s) - \beta_e^2(1-\hat{s}\cdot\hat{\imath})\}\right]_{ret} \quad (3.64)$$

In the above two equations, the term $\frac{e^2}{4\pi\varepsilon_0 m_0 c^2}$ is defined as the classical electron radius r_e with a value equal to 2.82×10^{-15} m.

3.6 The Nature of the scattered signal at the detector

3.6.1 Scattering due to a single electron

Based on the formula of the simplified scattered electric field given in equation (3.64), the Poynting vector given in equation (3.54) can be deduced. Furthermore, we can measure the energy scattered in an area of a specified period by a detector. Before deducing the energy received by detectors, we need to confirm the formation of E_i mentioned in equation (3.64). To a laser traversing electrons, the wavefront of it can be assumed as a plane monochromatic wave. As a result, E_i mentioned in equation (3.64) can be given as

$$E_i = E_{i0}\cos\left[\vec{k}_i\cdot\vec{r}_p(t_r) - \omega_i t_r\right] \quad (3.65)$$

where $\vec{k}_i$ and ω_i are the incident wave number and radian frequency, respectively. As mentioned in section 3.2, the photon energy is negligible to the electron's energy in Thomson scattering, thus, the electron's trajectory won't be disturbed by the incident wave and it can be expressed as

$$\vec{r}_p(t_r) = \vec{v}t_r + \vec{r}_{p0} \quad (3.66)$$

where $\vec{v}$ is the velocity of the electron and $\vec{r}_{p0}$ is the initial position of the electron. It should be noted that $\vec{v}$ is no more the function of t_r because it's the velocity of the electron without the influence of the incident electromagnetic wave. Furthermore, in a far-field approximation, $r \gg r_p(t_r)$, $r \cong R$ and $\frac{\vec{R}}{R} = \hat{R} \equiv \hat{s} \cong \hat{r}$ are satisfied. Because $r \cong R$ is satisfied, in this case, R and $\hat{R}$ are no more the function of t_r. Also $\hat{R} \equiv \hat{s}$ is defined as the unit vector pointing from the charge to the observer. Hence,

$$t_r = t - \frac{\left|\vec{r} - \vec{r}_p(t_r)\right|}{c} = t - \frac{1}{c}\sqrt{\left(\vec{r} - \vec{r}_p(t_r)\right)^2}$$

$$= t - \frac{1}{c}\sqrt{r^2 - 2\vec{r}\cdot\vec{r}_p(t_r) + r_p^2} \cong t - \frac{1}{c}\sqrt{R^2 - 2R\hat{s}\cdot\vec{r}_p}$$

Based on the binominal expansion to first order,

$$t_r = t - \frac{1}{c}\sqrt{R^2 - 2R\hat{s}\cdot\vec{r}_p} = t - \frac{1}{c}\left[R - \hat{s}\cdot\vec{r}_p(t_r)\right] \qquad (3.67)$$

Substituting equation (3.66) into (3.67), we have

$$t_r = t - \frac{R}{c} + \hat{s}\vec{\beta}t_r + \frac{\hat{s}\cdot\vec{r}_{p0}}{c},$$

where $\vec{\beta} = \vec{v}/c$. Thus, t_r can be expressed as

$$t_r = \frac{t - \frac{R}{c} + \frac{\hat{s}\cdot\vec{r}_{p0}}{c}}{1 - \hat{s}\cdot\vec{\beta}} \qquad (3.68)$$

Substituting equation (3.66) and (3.68) into equation (3.65), we have

$$E_i = E_{i0}cos\left[\vec{k}_i\cdot\left(\vec{v}t_r + \vec{r}_{p0}\right) - \omega_i\frac{t - \frac{R}{c} + \frac{\hat{s}\cdot\vec{r}_{p0}}{c}}{1 - \hat{s}\cdot\vec{\beta}}\right]$$

$$= E_{i0}\cos\left[k_iR\left(\frac{1 - \hat{\imath}\cdot\vec{\beta}}{1 - \hat{s}\cdot\vec{\beta}}\right) - \omega_i\left(\frac{1 - \hat{\imath}\cdot\vec{\beta}}{1 - \hat{s}\cdot\vec{\beta}}\right)t\right.$$

$$\left. - k_i\hat{s}\cdot\vec{r}_{p0}\left(\frac{1 - \hat{\imath}\cdot\vec{\beta}}{1 - \hat{s}\cdot\vec{\beta}}\right) + \vec{k}_i\cdot\vec{r}_{p0}\right] \qquad (3.69)$$

where $\vec{k}_i = k_i\hat{\imath} = \frac{\omega_i}{c}\hat{\imath}$, and $\hat{\imath}$ is a unit vector in the direction of the incident wave. Substitute equation (3.69) into the scattered electric field given in equation (3.64) we have

$$E_s(R,t) = r_e\left[\frac{E_{i0}}{\gamma(1-\beta_s)^3 R}\{(1-\beta_i)(1-\beta_s) - \beta_e^2(1-\hat{s}\cdot\hat{\imath})\}\right] \times \cos\left[k_s R - \omega_s t - \vec{k}\cdot\vec{r}_{p0}\right] \quad (3.70)$$

Here based on the relationship between radian wave vector and radian frequency we have $\vec{k}_s = (\omega_s/c)\hat{s}$. Moreover, $\vec{k} = \vec{k}_s - \vec{k}_i$.

Comparing the arguments in the cosine of equations (3.70) with that in equation (3.69), the following relationships can be obtained.

$$k_s = k_i\left(\frac{1-\hat{\imath}\cdot\vec{\beta}}{1-\hat{s}\cdot\vec{\beta}}\right) = k_i\left(\frac{1-\beta_i}{1-\beta_s}\right)$$

and

$$\omega_d = \omega_s = \omega_i\left(\frac{1-\hat{\imath}\cdot\vec{\beta}}{1-\hat{s}\cdot\vec{\beta}}\right) = \omega_i\left(\frac{1-\beta_i}{1-\beta_s}\right).$$

These two terms are the Doppler-shifted radian wave number and the Doppler-shifted radian frequency ω_d, respectively. Here, the radian frequency is Doppler-shifted for two reasons. One is that an electron as the observer has motion in the transmission direction of the incident light wave. Another is that radiating electrons have motion toward or away from the observer.

It can be seen from equation (3.70) that the time variable *t* inside arguments in the cosine appears again. The purpose of this is to calculate the scattered power from the view of the time *t* at the observer at first[48], and then make a conversion to the view of the retarded time at the observer. Another way of calculating the scattered power is from the view of the retarded time at the observer directly, which has been detailed in these references[45,50].

Rewrite the scattered field given by equation (3.70) in the following complex form,

$$E_s(R,t) = r_e\left[\frac{E_{i0}}{\gamma(1-\beta_s)^3 R}\{(1-\beta_i)(1-\beta_s) - \beta_e^2(1-\hat{s}\cdot\hat{\imath})\}\right]$$

$$\times e^{j(k_s R-\omega_s t)} \tag{3.71}$$

The term $\vec{k}\cdot\vec{r}_{p0}$ has been dropped because $k_s R \gg \vec{k}\cdot\vec{r}_{p0}$ based on the far-field approximation that $R \gg r_{p0}$ where r_{p0} is the initial position of the electron.

With the expression of the scattered electric field given in the latter equation, we can deduce the average scattered power due to a single electron. The time-averaged Poynting vector of a single electron can be written as

$$\begin{aligned}\left\langle \vec{S}(R,t)\right\rangle &= \frac{1}{T_s}\int_0^{T_s} Re\left(\overrightarrow{E_s}(R,t)\right)\times Re\left(\overrightarrow{H_s}(R,t)\right)dt\\ &= \frac{1}{4T_s}\int_0^{T_s}\left[\overrightarrow{E_s}(R)e^{-j\omega_s t}+\overrightarrow{E_s}^{*}(R)e^{j\omega_s t}\right]\\ &\qquad\times\left[\overrightarrow{H_s}(R)e^{-j\omega_s t}+\overrightarrow{H_s}^{*}(R)e^{j\omega_s t}\right]dt\\ &= \frac{1}{4}Re\left(\overrightarrow{E_s}(R)\times\overrightarrow{H_s}^{*}(R)+\overrightarrow{E_s}^{*}(R)\times\overrightarrow{H_s}(R)\right)\\ &= \frac{1}{2}R\,e\left(\overrightarrow{E_s}(R,t)\times\overrightarrow{H_s}^{*}(R,t)\right)\end{aligned} \tag{3.72}$$

In the latter equation, only $e^{-j\omega t}$ and $e^{j\omega t}$ are related to the integral variable due to the far-field approximation. Other parts of the $\overrightarrow{E_s}(R,t)$ and $\overrightarrow{H_s}(R,t)$ can be written as another complex vector. Compared with equation (3.54), the term 1/2 is caused by the time average.

Therefore, the energy scattered through a solid angle $\mathrm{d}\Omega_s$ at the observer in a time interval $\mathrm{d}t$ is given by

$$\mathrm{d}^2E = \left|\left\langle\vec{S}(R,t)\right\rangle\right|R^2\mathrm{d}\Omega_s\mathrm{d}t = \frac{c\varepsilon_0}{2}\left|\overrightarrow{E_s}(R,t)\right|^2R^2\mathrm{d}\Omega_s\mathrm{d}t \tag{3.73}$$

Further, the averaged scattered power at the observer $\bar{P}_0$ by a single electron per unit solid angle is

$$\begin{aligned}\frac{\mathrm{d}\bar{P}_0}{\mathrm{d}\Omega_s} &= \frac{c\varepsilon_0R^2}{2}\lim_{T\to\infty}\left\{\frac{1}{T}\int_{-T/2}^{T/2}|E_s(R,t)|^2\mathrm{d}t\right\}\\ &= \frac{c\varepsilon_0R^2}{2}\lim_{T\to\infty}\frac{1}{T2\pi}\int_{-\infty}^{+\infty}|E_S(\omega_s)|^2\mathrm{d}\omega_S\end{aligned} \tag{3.74}$$

where $T \to \infty$ implies that T is the integration time of the measurement or the response time of the detector and $T \gg 2\pi/\omega_s$. $E_s(\omega_s)$ is the Fourier transform of $E_s(R,t)$. Based on the Fourier transform of $E_S(R,t)$ as

$$E_S(\omega_s) = \int_{-\infty}^{+\infty} E_s(R,t) e^{j\omega_s t}\,\mathrm{d}t \tag{3.75}$$

and the role of the Dirac delta function $\delta(\omega_s - \omega_\mathrm{d})$ given by the integral as

$$\delta(\omega_s - \omega_\mathrm{d}) = \frac{1}{2\pi}\int_{-\infty}^{+\infty} e^{j(\omega_s-\omega_\mathrm{d})t}\,\mathrm{d}t \tag{3.76}$$

we can rewrite the formula of the scattered field as

$$E_S(\omega_s) = 2\pi r_e[\frac{E_{i0}e^{jk_sR}}{\gamma(1-\beta_s)^3R}\{(1-\beta_i)(1-\beta_s)-\beta_e^2(1-\hat{s}\cdot\hat{\imath})\}$$
$$\delta(\omega_s-\omega_\mathrm{d})] \tag{3.77}$$

Substitute equation (3.77) into equation (3.74), and we have

$$\frac{\mathrm{d}^2\bar{P}_0}{\mathrm{d}\Omega_s\mathrm{d}\omega_s} = c\varepsilon_0 r_e^2\pi$$
$$\left[\frac{E_{i0}^2}{\gamma^2(1-\beta_s)^6}\{(1-\beta_i)(1-\beta_s)-\beta_e^2(1-\hat{s}\cdot\hat{\imath})\}^2\right]$$
$$\lim_{T\to\infty}\frac{1}{T}\delta^2(\omega_s-\omega_\mathrm{d}) \tag{3.78}$$

With the property of the delta function as [a primer 28 29]

$$\lim_{T\to\infty}\frac{1}{T}\delta^2(\omega_s-\omega_\mathrm{d}) = \frac{1}{2\pi}\delta(\omega_s-\omega_\mathrm{d}) \tag{3.79}$$

we can rewrite equation (3.78) as

$$\frac{\mathrm{d}^2\bar{P}_0}{\mathrm{d}\Omega_s\mathrm{d}\omega_s} = \frac{r_e^2 c\varepsilon_0 E_{i0}^2}{2}$$
$$\left[\frac{(1-\beta^2)}{(1-\beta_s)^6}\{(1-\beta_i)(1-\beta_s)-\beta_e^2(1-\hat{s}\cdot\hat{\imath})\}^2\right]\delta(\omega_s-\omega_\mathrm{d}) \tag{3.80}$$

Finally, because equation (3.80) is measured at the observer while what we need is the scattered power at the particle itself, we rewrite equation (3.80) as

$$\frac{d^3\bar{E}_0}{dtd\Omega_s d\omega_s} = \frac{d^3\bar{E}_0}{\frac{dt}{dt_r}dt_r d\Omega_s d\omega_s} = \frac{r_e^2 c\varepsilon_0 E_{i0}^2}{2}$$

$$\left[\frac{(1-\beta^2)}{(1-\beta_s)^6}\{(1-\beta_i)(1-\beta_s)-\beta_e^2(1-\hat{s}\cdot\hat{\imath})\}^2\right]\delta(\omega_s-\omega_d) \quad (3.81)$$

Because the relationship between t and t_r is given in equation (3.43), we have the following equation which is the scattered power per solid angle per radian frequency at the electron.

$$\frac{\mathrm{d}^2\bar{P}_e}{\mathrm{d}\Omega_s \mathrm{d}\omega_s} = \frac{r_e^2 c\varepsilon_0 E_{i0}^2}{2}\left[\frac{(1-\beta^2)}{(1-\beta_s)^6}\{(1-\beta_i)(1-\beta_s)-\beta_e^2(1-\hat{s}\cdot\hat{\imath})\}^2\right] \tilde{\kappa}\delta(\omega_s-\omega_{\mathrm{d}}) \quad (3.82)$$

Where $\tilde{\kappa} = 1-\beta_s$, subscript e of P means this power is measured at the electron itself.

3.6.2 Scattering from an assembly of electrons

In the last section, we have calculated the scattering from a single electron. In plasma, the scattering will be consisting of many electrons. To calculate the total scattering, it is necessary to add up the electric field contributions from each of the electrons. However, the problem whether the phase of scattering electrons are purely randomly distributed is unknown. Plasma is a medium that supports various collective effects, resulting in correlated electron positions and movements. Therefore, in certain scenarios, the summation requires coherent addition, which will not be a simple sum of all electric field corresponding to all scattering electrons. Based on equation (3.70) showing the scattered electric field, all electrons having the constant phase factor $\vec{k}\cdot\vec{r}_{p0}$ will scatter in phase. The equation $\vec{k}\cdot\vec{r}_{p0} = Constant$ gives a plane whose normal vector is $\vec{k}$, which means all electrons in this plane will scatter in phase. Electrons located in any adjacent parallel planes $\vec{k}\cdot(\vec{r}_{p0}+\Delta\vec{r}) = Constant + 2\pi$ will also scatter in phase with the plane above, hence, the radian wavenumber

$\frac{2\pi}{\lambda}$ is also defined as scale length. Therefore, the magnitude of the average Poynting vector corresponding to an assembly of electrons in plasma isn't the simple sum of all separated contributions given by each electron but also with consideration of the possible collective effect between electrons. The average scattered power per solid angle from an assembly of electrons is given as

$$\frac{d\bar{P}_e}{\mathrm{d}\Omega_s} = \frac{1}{2}R^2 c\epsilon_0 \sum_j \vec{E}_j \cdot \sum_i \vec{E}_i$$
$$= \frac{1}{2}R^2 c\epsilon_0 \sum_j \vec{E}_j^2 + \frac{1}{2}R^2 c\epsilon_0 \cdot \sum_{i\neq j} \vec{E}_i \cdot \vec{E}_j \qquad (3.83)$$

The sum of the scattered powers from every individual electron comprises the first term, while the second term is attributable to the correlation of electron positions. If the electrons are distributed randomly in space, the ensemble average of the second term is zero. In this case, the total scattered power from a volume of electrons can be obtained by the sum of the magnitude of the Poynting vector over all electrons. To the electrons in plasma, the collective effect needs to be considered if some situations satisfy. Therefore, it's necessary to determine whether the collective effect contributes to the second term of the average scattered power. A condition to determine whether the scattering takes the form of incoherent or coherent is summarised here[51].

The smallest correlation length in plasma is the Debye length. It's used to determine whether scattering is coherent or incoherent. It refers to the effect that a charge in plasma is shielded by other charges over a characteristic length. Influence made by a potential-perturbing charge on other charges can only happen within Debye length, as called Debye shielding. The charges in plasma tend to redistribute themselves to shield the plasma from the electric field generated by perturbing charges. As a result, the effects of a potential perturbing charge in plasma are generally much shorter than that exists in vacuum[40]. The characteristic Debye length can be derived from

Poisson's equation by assuming both electrons and ions are in thermal equilibrium, which is given as

$$\lambda_D = \left(\frac{\epsilon_0 T_e}{e^2 n_e}\right)^{\frac{1}{2}} \tag{3.84}$$

where T_e is the electron temperature. n_e is the electron density and e is the electron charge.

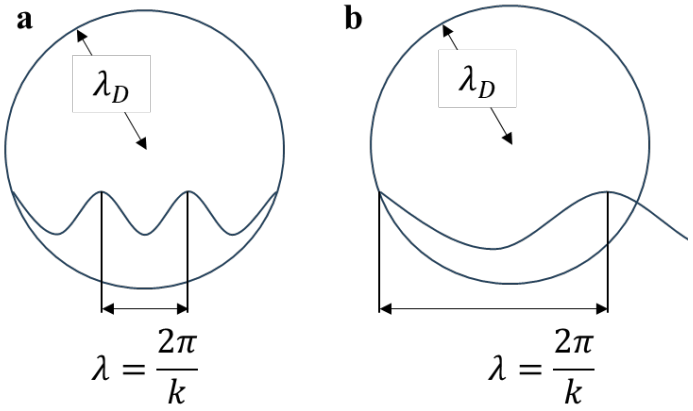

Figure 3.5: (a) Incoherent scattering. (b) Collective scattering.

Compare the ratio between Debye length and the scattering length k, scattering type can be determined[52]. If $\lambda_D \gg 2\pi/k$, significant phase changes between each electron that result in a lack of correlation, As a consequence, electrons are randomly distributed and the second term for the scattered power in equation (3.83) becomes zero on average. This phenomenon is defined as incoherent scattering. On the other hand, if $\lambda_D < 2\pi/k$, In this case, the resolution is small and only the motion of the electron cloud can be detected, resulting in coherent scattering. The positions of the electrons within the cloud are interrelated as they follow the motion of the ion, making their scattering correlated. This necessitates the inclusion of the second term in the calculation of the average scattered power. This phenomenon is defined as coherent scattering.

A method is provided to approximately quantify the scale length[48]. The scale length can be expanded as

$$k = \left|\vec{k}\right| = \left|\vec{k}_s - \vec{k}_i\right| = \sqrt{k_s^2 + k_i^2 - 2k_s k_i \cos\theta} \tag{3.85}$$

where θ is the scattering angle between $\vec{k}_s$ and $\vec{k}_i$. As $k_s = \omega_s/c, k_i = \omega_i/c$ and $\omega_s \approx \omega_i$, the following expression can be obtained

$$k = \frac{4\pi}{\lambda_i}\sin\frac{\theta}{2} \tag{3.86}$$

where λ_i is the wavelength of the incident electromagnetic wave that perturbs the electron for an oscillation. With equation (3.86), the scattering type can be readily identified based on the wavelength of the incident wave and scattering angle.

3.6.3 Incoherent scattering from an assembly of electrons

If the phases of all contributions are completely uncorrelated, from the formula of the scattered electric field produced by one accelerated electron, we can further deduce the scattered power produced by an assembly of electrons from an incoherent scattering. Based on equation (3.82), the power scattered per unit solid angle per unit angular frequency interval from an assembly of electrons with density n_e and velocity distribution $f(\vec{\beta})$ is given by

$$\frac{\mathrm{d}^2\bar{P}_e}{\mathrm{d}\Omega_s \mathrm{d}\omega_s} = r_e^2 \int_{\mathrm{vol}} \langle S_i \rangle n_e \, \mathrm{d}^3\vec{r} \int_{\mathrm{vel}} \left[\frac{(1-\beta^2)}{(1-\beta_s)^6}\{(1-\beta_i)(1-\beta_s) - \beta_e^2(1-\hat{s}\cdot\hat{\imath})\}^2\right] \tilde{\kappa}\delta(\omega_s - \omega_{\mathrm{d}})\mathrm{d}^3\vec{\beta} \tag{3.87}$$

where $\langle S_i \rangle = c\varepsilon_0 E_{i0}^2/2$ is the time-averaged Poynting vector for the incident field. What's more, because of the relation in the argument of the Delta function that

$$\delta(\omega_s - \omega_{\mathrm{d}}) = \delta\left(\omega_s - \omega_i \frac{1-\beta_i}{1-\beta_s}\right) = \delta\left(\frac{\omega_s(1-\beta_s) - \omega_i(1-\beta_i)}{1-\beta_s}\right)$$

$$= \delta\left(\frac{(\omega_s - \omega_i) - \vec{k}\cdot\vec{v}}{1-\beta_s}\right) \tag{3.88}$$

the rule of the Delta function $\delta(ax) = \frac{1}{|a|}\delta(x)$ and $\delta(x) = \delta(-x)$, we have the following relationship,

$$\tilde{\kappa}\delta\left(\vec{k}\cdot\vec{v} - \omega\right) = \delta(\omega_s - \omega_{\mathrm{d}}) \tag{3.89}$$

Here we define ω as $\omega_s - \omega_i = \vec{k}\cdot\vec{v}$. As a result, the expression of the scattered power per solid angle per radian frequency can now be written in the following form,

$$\begin{aligned}\frac{\mathrm{d}^2\bar{P}}{\mathrm{d}\Omega_s \mathrm{d}\omega_s} = \;& r_e^2 \int_{\mathrm{vol}} \langle S_i\rangle n_e \mathrm{d}^3\vec{r} \int_{\mathrm{vel}} \frac{(1-\beta^2)}{(1-\beta_s)^4} \\ & \times \{(1-\beta_i)(1-\beta_s) - \beta_e^2(1-\hat{s}\cdot\hat{\imath})\}^2 \\ & \times f\left(\vec{\beta}\right)\delta\left(\vec{k}\cdot\vec{v} - \omega\right)\mathrm{d}^3\vec{\beta} \\ = \;& r_e^2 \int_{\mathrm{vol}} \langle S_i\rangle n_e \mathrm{d}^3\vec{r} \int_{\mathrm{vel}} \left(\frac{\omega_s}{\omega_i}\right)^2 \\ & \times \left\{1 - \frac{\beta_e^2(1-\hat{s}\cdot\hat{\imath})}{(1-\beta_i)(1-\beta_s)}\right\}^2 \\ & \times (1-\beta^2) f\left(\vec{\beta}\right)\delta\left(\vec{k}\cdot\vec{v} - \omega\right)\mathrm{d}^3\vec{\beta}\end{aligned} \tag{3.90}$$

Here, $\frac{(1-\beta_i)^2}{(1-\beta_s)^2} = \left(\frac{\omega_s}{\omega_i}\right)^2$ is obtained based on the definition of the refractive index as $n = c/v$ and the relationship between k, β and ω. In equation (3.90), $(\omega_s/\omega_i)^2$ represents the blue shift in the scattered spectrum, which can be taken out of the integral because it's independent of velocity. $\left\{1 - \frac{\beta_e^2(1-\hat{s}\cdot\hat{\imath})}{(1-\beta_i)(1-\beta_s)}\right\}^2$ dependent on β_e represents the depolarization term that affects the shape of the scattered spectrum in high-temperature conditions. Lastly, the quantity $1-\beta^2$ can be grouped with the classical electron radius r_e to form the modified electron radius r_e' as $r_e' = \frac{e^2}{4\pi\varepsilon_0 c^2 m_0/\sqrt{1-\beta^2}}$, which shows a smaller value compared with the pre-modified classical electron radius as a result of the relativistic increase in mass with velocity.

3.6.4 The analytical formula of Incoherent Thomson scattering spectrum

From the scattered power per solid angle per radian frequency given in equation (3.90), we define the spectral density function S as the spectral distribution of the scattered radiation per unit radian frequency interval as

$$S = \int_{\text{vel}} \left(\frac{\omega_s}{\omega_i}\right)^2 \left\{1 - \frac{\beta_e^2(1 - \hat{s}\cdot\hat{\imath})}{(1-\beta_i)(1-\beta_s)}\right\}^2 \times (1-\beta^2) f(\vec{\beta}) \delta(\vec{k}\cdot\vec{v} - \omega) \mathrm{d}^3\vec{\beta} \tag{3.91}$$

It can be noted that the form of the spectral density function is dependent on the electron velocity distribution function and the scattering angle $\theta(\cos\,\theta = \hat{s}\cdot\hat{\imath})$. However, it is difficult to derive an analytical expression for the spectral density function S in the general case of a high-temperature plasma unless the expression of the velocity distribution is specified. Normally, the Maxwellian electron velocity distribution is assumed in majority of fusion plasmas. With consideration of the effect brought by high-temperature conditions on the standard formula of the Maxwellian distribution, the standard formula for the Maxwellian distribution is modified to take account of relativistic effects as a relativistic Maxwellian velocity distribution, as shown as

$$f(\beta) = \frac{\alpha}{2\pi K_2(2\alpha)} \frac{\exp\left[-2\alpha(1-\beta^2)^{-\frac{1}{2}}\right]}{(1-\beta^2)^{\frac{5}{2}}} \tag{3.92}$$

where $K_2(2\alpha)$ is the modified second kind Bessel function of second order, α is equal to $m_0c^2/2k_BT$ where m_0c^2 is the rest mass of the electron, k_B is Boltzmann's constant, $\beta = v/c$ and T is the temperature.

Because the assumption of the electrons has a relativistic Maxwellian velocity distribution in the scattering volume, equation

(3.91) can be numerically integrated. Here a coordinate system to determine the scattered spectrum from the electrons within the scattering volume is established. This coordinate has three orthogonal axes, namely β_k parallel to the k direction, $\beta_{k\perp}$, orthogonal to β_k and in the same plane as $\overrightarrow{k_s}$ and $\overrightarrow{k_i}$. The final axis of this coordinate system, β_{kT}, is perpendicular to the plane of $\hat{s}$ and $\hat{\imath}$. The coordinate system is shown in Fig 3.6. From Fig 3.6, the relationships between β_i, β_s, β_e and β_k, $\beta_{k\perp}$ and β_{kT} can be obtained as follows[53,54].

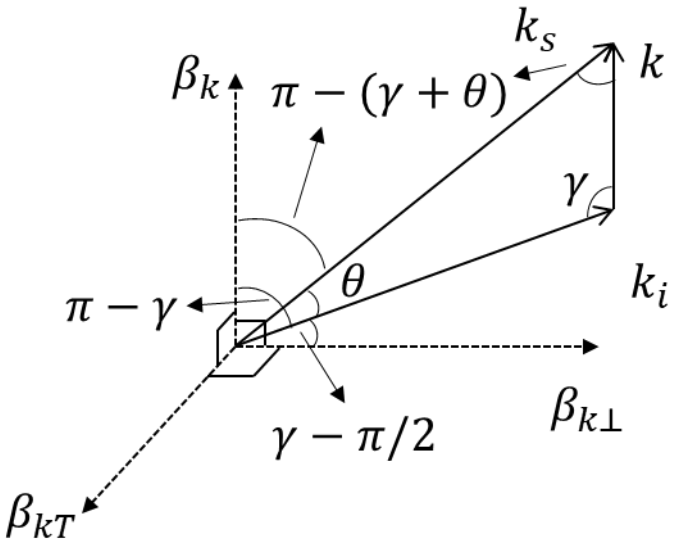

Figure 3.6: Coordinate system used to determine the scattered spectrum from the electrons within the scattering volume.

$$\beta_i = \beta_k \cos(\pi-\gamma) + \beta_{k\perp}\cos\left(\gamma-\frac{\pi}{2}\right) = -\beta_k \cos\gamma + \beta_{k\perp}\sin\gamma$$

$$\beta_s = \beta_k \cos[\pi-(\gamma+\theta)] + \beta_{k\perp}\cos\left[\left(\gamma-\frac{\pi}{2}\right)+\theta\right]$$

$$= -\beta_k \cos(\gamma+\theta) + \beta_{k\perp}\sin(\gamma+\theta)$$

$$\beta_e = \beta_{kT} \qquad (3.93)$$

Regarding the depolarization term $\left\{1-\frac{\beta_e^2(1-\hat{s}\cdot\hat{\imath})}{(1-\beta_i)(1-\beta_s)}\right\}^2$ in equation (3.91), it can be seen that it depends on β_e^2 which is a relativistic effect and thus it will have a stronger effect on the form of the spectral

density distribution in high-temperature plasma conditions. It has been confirmed that it has a negligible effect on the overall shape of the scattered spectrum but a significant reduction in the scattered intensity for very high-temperature plasmas[48,50,55].

When the depolarization term can be neglected, the analytical formula of the spectral distribution of the scattered radiation per unit radian frequency can be obtained by integrating the following equation over the velocity components,

$$S_Z = \iiint \left(\frac{\omega_s}{\omega_i}\right)^2 (1-\beta^2) f(\vec{\beta}) \delta(\vec{k}\cdot\vec{v}-\omega) \mathrm{d}^3\vec{\beta} \tag{3.94}$$

The derivation procedure is briefly summarized here based on the method proposed by Prunty's group[48,50,55].

Based on the property of the Dirac delta function, we have

$$\begin{aligned}\delta(\vec{k}\cdot\vec{v}-\omega) &= \delta(kv_k-\omega) = \delta(kc\beta_k-\omega) \\ &= \delta\left(kc\left(\beta_k-\frac{\omega}{kc}\right)\right) = \frac{1}{kc}\delta\left(\beta_k-\frac{\omega}{kc}\right)\end{aligned}$$

By substituting equation (3.92) into (3.94), we have

$$\begin{aligned}&\iiint \left(\frac{\omega_s}{\omega_i}\right)^2 (1-\beta^2) \frac{\alpha}{2\pi K_2(2\alpha)} \\ &\times \frac{\exp\left[-2\alpha(1-\beta^2)^{-\frac{1}{2}}\right]}{(1-\beta^2)^{\frac{5}{2}}} \frac{1}{kc}\delta\left(\beta_k-\frac{\omega}{kc}\right) \\ &\times \mathrm{d}\beta_k\, \mathrm{d}\beta_{k\perp} \mathrm{d}\beta_{kT} \\ &= \frac{\alpha}{2\pi K_2(2\alpha)}\left(\frac{\omega_s}{\omega_i}\right)^2 \frac{1}{kc} \iiint (1-\beta^2)^{-\frac{3}{2}} \\ &\times \exp\left[-2\alpha(1-\beta^2)^{-\frac{1}{2}}\right] \delta\left(\beta_k-\frac{\omega}{kc}\right) \\ &\times \mathrm{d}\beta_k\, \mathrm{d}\beta_{k\perp} \mathrm{d}\beta_{kT}.\end{aligned} \tag{3.95}$$

where $\beta^2 = \beta_k^2 + \beta_{kT}^2 + \beta_{k\perp}^2$. Due to the property of the Dirac delta function, the integration with respect to β_k can be obtained, the rest regarding to $\beta_{k\perp}$ and β_{kT} is shown as

$$S_Z = \frac{\alpha}{2\pi K_2(2\alpha)}\left(\frac{\omega_s}{\omega_i}\right)^2 \frac{1}{kc} \times$$

$$\int_{-\sqrt{1-\frac{\omega^2}{k^2}}}^{\sqrt{1-\frac{\omega^2}{k^2}}} \int_{-\sqrt{1-\frac{\omega^2}{k^2c^2}-\beta_{kT}^2}}^{\sqrt{1-\frac{\omega^2}{k^2c^2}-\beta_{kT}^2}} \left(1-\frac{\omega^2}{k^2c^2}-\beta_{kT}^2\right.$$

$$\left.-\beta_{k\perp}^2\right)^{-\frac{3}{2}} \exp\left[-2\alpha\left(1-\frac{\omega^2}{k^2c^2}-\beta_{kT}^2-\beta_{k\perp}^2\right)^{-\frac{1}{2}}\right] \mathrm{d}\beta_{k\perp}\mathrm{d}\beta_{kT} \quad (3.96)$$

The limits of integration are determined by the region of β as $-1 \leqslant \beta \leqslant 1$, the relasion of β as $\beta^2 = \beta_k^2 + \beta_{kT}^2 + \beta_{k\perp}^2$ and the sieving property of the Dirac delta function from $\delta\left(\beta_k - \frac{\omega}{kc}\right)$.

Defining $\eta = \omega/kc$, with the fact of $\omega = \omega_s - \omega_i$ and $kc = \sqrt{\omega_s^2 + \omega_i^2 - 2\omega_s\omega_i \cos\theta}$, the integration regarding to $\beta_{k\perp}$ can be calculated as

$$\int_0^{\sqrt{1-\eta^2-\beta_{kT}^2}} \left(1-\eta^2-\beta_{kT}^2-\beta_{k\perp}^2\right)^{-\frac{3}{2}} exp$$

$$\left[-2\alpha\left(1-\eta^2-\beta_{kT}^2-\beta_{k\perp}^2\right)^{-\frac{1}{2}}\right] \mathrm{d}\beta_{k\perp} \quad (3.97)$$

With several steps of variable substitutions, the latter equation can be written as

$$\frac{1}{A^2}\int_1^{\infty} \frac{e^{-\frac{2\alpha}{A}\zeta}\zeta \mathrm{d}\zeta}{\sqrt{\zeta^2-1}} = \frac{1}{A^2} K_1\left(\frac{2\alpha}{A}\right) \quad (3.98)$$

where $\zeta = Az$, $A^2 = 1-\eta^2-\beta_{kT}^2$ and $z = (A^2-\beta_{k\perp}^2)^{-1/2}$. $K_1\left(\frac{2\alpha}{A}\right)$ is a first-order modified Bessel function of the second kind.

Substituting the latter equation into equation (3.96), the integration inside equation (3.96) concerning β_{kT} can be written as

$$\int_0^{\sqrt{1-\eta^2}} \frac{1}{A^2} K_1\left(\frac{2\alpha}{A}\right) \mathrm{d}\beta_{kT} \quad (3.99)$$

With another several step of variable substitutions, equation (3.99) can be written as

$$\int_1^{\infty} \frac{K_1(2\mu\xi)\mathrm{d}\xi}{\sqrt{\xi^2-1}} = \frac{\pi}{4\mu} e^{-2\mu} \quad (3.100)$$

where $\mu = \alpha/\sqrt{1-\eta^2}$, $\xi = z\sqrt{1-\eta^2}$, $z = 1/A$ and $A^2 = 1-\eta^2-\beta_{kT}^2$.

Finally, equation (3.96) can be written as

$$S_Z = \frac{\alpha}{2\pi K_2(2\alpha)}\left(\frac{\omega_s}{\omega_i}\right)^2 \frac{4}{kc}\frac{\pi}{4\alpha}\exp\left(-\frac{2\alpha}{\sqrt{1-\eta^2}}\right)$$
$$= [2K_2(2\alpha)]^{-1}\frac{1}{kc}\exp\left(-\frac{2\alpha}{\sqrt{1-\eta^2}}\right) \qquad (3.101)$$

This analytic expression was firstly deduced by Zhuravlev and Petrov[53] although a mathmatical mistake termed as "finite transit time effect" was introduced. The detail of how finite transit time effect was found and corrected can be found in Kukushkin's work[56]. Furthermore, with $\eta = (\omega_s - \omega_i)/kc$ and $kc = \sqrt{\omega_s^2 + \omega_i^2 - 2\omega_s\omega_i\cos\theta}$, the scattered power per solid angle per unit radian frequency interval can be written as

$$\frac{\mathrm{d}^2P}{\mathrm{d}\Omega_s \mathrm{d}\omega_s} = r_e^2 \int_{\mathrm{vol}} \langle S_i\rangle n_e \,\mathrm{d}^3\vec{r}\,[2K_2(2\alpha)]^{-1} \times \frac{\tilde{\omega}^2}{\omega_i\sqrt{1+\tilde{\omega}^2-2\tilde{\omega}\cos\theta}} \times \exp\left[-2\alpha\sqrt{1+\frac{(\tilde{\omega}-1)^2}{2\tilde{\omega}(1-\cos\theta)}}\right] \qquad (3.102)$$

where $\tilde{\omega}$ is defined as $\tilde{\omega} = \omega_s/\omega_i$. The spectral density distribution function S involved can be written as

$$S(\tilde{\omega},\theta,2\alpha) = \frac{1}{2K_2(2\alpha)}\frac{\tilde{\omega}^2}{\sqrt{1+\tilde{\omega}^2-2\tilde{\omega}\cos\theta}} \times \exp\left[-2\alpha\sqrt{1+\frac{(\tilde{\omega}-1)^2}{2\tilde{\omega}(1-\cos\theta)}}\right] \qquad (3.103)$$

Based on the relationships of $\tilde{\omega} = \frac{1}{1+\varepsilon}$ and $\varepsilon = (\lambda_s - \lambda_i)/\lambda_i$, the spectral density distribution function S can be written in terms of normalized wavelength shift ε as

$$S(\varepsilon,\theta,2\alpha)=\frac{e^{-2\alpha x}}{2K_2(2\alpha)(1+\varepsilon)^3}\times[2(1-\cos\theta)(1+\varepsilon)+\varepsilon^2]^{-\frac{1}{2}} \quad (3.104)$$

where the quantity x is given by $x=\left[1+\frac{\varepsilon^2}{2(1-\cos\ \theta)(1+\varepsilon)}\right]^{\frac{1}{2}}$.

To the depolarization term, it can be given as the following fomular[48,50],

$$q(\varepsilon,\theta,2\alpha)=1+\frac{2x}{y^3}e^{2\alpha x}[y^2\int_x^\infty\frac{e^{-2\alpha\xi}}{(\xi^2+u^2)^{\frac{3}{2}}}\,\mathrm{d}\xi-3\int_x^\infty\frac{e^{-2\alpha\xi}}{(\xi^2+u^2)^{\frac{5}{2}}}\,\mathrm{d}\xi] \quad (3.105)$$

Where

$$\mathrm{x}=\left[1+\frac{\varepsilon^2}{2(1-\cos\ \theta)(1+\varepsilon)}\right]^{\frac{1}{2}}$$

$$\mathrm{u}=\frac{\sin\ \theta}{1-\cos\ \theta}$$

$$y=\frac{1}{(x^2+u^2)^{1/2}}$$

$$\varepsilon=(\lambda_s-\lambda_i)/\lambda_i$$

Therefore, the complete analytical formula of the spectral density distribution function can be written as

$$S_T(\varepsilon,\theta,2\alpha)=\mathrm{S}(\varepsilon,\theta,2\alpha)q(\varepsilon,\theta,2\alpha) \quad (3.106)$$

When the temperature is relatively low, the depolarization term can be neglected or approximated. An approximation obtained by a rational fraction approximation for the depolarization term with a relative error lower than 0.1% below 100keV can be found in previous work[53].

Chapter 4
Nd:YAG Laser Thomson Scattering Measurement System in Heliotron J

4.1 Introduction

The Thomson scattering system on Heliotron J is initially constructed for the investigation of the effect of the control of the plasma profile on helical devices on improving plasma confinement[20]. To successfully observe the improved confinement effected by controlling the plasma profile, measurement of the time evolution of the plasma profile including T_e and n_e is necessary. Meanwhile, the time resolution of the measurement cannot be too low because the improved confinement phenomena frequently accompany the rapid transition during the plasma discharge[57]. The Thomson scattering system on Heliotron J is a YAG Thomson Scattering(YAG-TS) utilizing an interference filter polychromator. Compared with other types of Thomson scattering systems, such as LIDAR (light detection and ranging) Thomson scattering system and TV Thomson scattering system, systems utilizing a high repetition rate Nd:YAG laser can realize a high repetition laser operation for a better time resolution in observation of rapid transition phenomenon. Because high-power ruby lasers as the probe are utilized in the LIDAR Thomson scattering systems and TV Thomson scattering systems, the high repetition laser operation is incapable to be achieved. In addition, to the nuclear fusion devices with a medium or small radius, the spatial resolution of LIDAR system about ~15cm also cannot meet the requirement of the

profile measurement on Heliotron J whose minor radius of plasma is only ~17cm. Under this circumstance, Nd:YAG laser type Thomson scattering system is adopted as the Thomson scattering system on Heliotron J.

The Thomson scattering system utilizing Nd:YAG lasers consists of three parts, which are incidence optics, light collection optics, and spectroscopic system. In this chapter, the incidence optics, the light collection optics, the spectroscopic system, and the data acquisition system are given in sections 4.2, 4.3, 4.4, and 4.5 respectively.

4.2 Incidence Optics

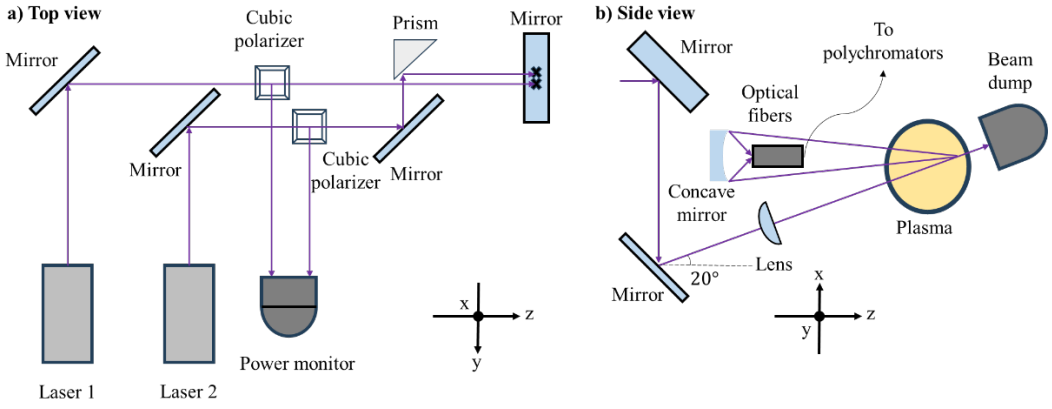

Fig 4.1: Schematic of the TS system on Heliotron J.

Incidence optics is used to guide laser beams into plasma to produce scattered light. To meet the requirements for profile measurement in the Heliotron J experiment, which has a typical discharge duration of 100-200 ms[58], a time resolution of 10 ms is desired. The Nd:YAG laser used for this purpose needs to have a repetition rate of greater than 100 Hz and deliver laser energy of at least 550 mJ per pulse. To fulfill these specifications using commercially available lasers, two 50 Hz Nd:YAG lasers manufactured by Continuum are chosen. The desired repetition rate of 100 Hz can be achieved by a timing controller[59] that controls these two lasers operating alternatively. The Nd:YAG laser will be operated in

four states in sequence after it receives the corresponding trigger signals from the timing controller. These four states are standby, flash, switch on, and shutter. In the standby state, power is supplied to the laser unit. In the flash state, the flash lamp is operating. In the Q switch state, the Q switch operation is started and a laser pulse with a length of 10 ns is generated. Lastly, the shutter of the Nd:YAG laser will be opened after the timing controller receives the plasma discharge trigger so that the laser can be injected into the optical path.

Table 4.1: System performance of the YAG-TS system in Heliotron J

Parameter name	Value
Laser wavelength	$1064\ \mathrm{nm}$
Laser pulse energy	$\sim 550\ \mathrm{mJ}$
Laser repetition frequency	$50\ \mathrm{Hz}$
Time interval of measurement	$10\mu\mathrm{sec} - 10\mathrm{msec}$
Measurement range of T_e	$10\mathrm{eV} - 10\mathrm{keV}$
Measurement range of n_e	$> 0.5 \times 10^{19}\ \mathrm{m}^{-3}$
Spatial points	25
Spatial resolution	$\sim 10\ \mathrm{mm}$

Fig 4.1 shows a schematic side view of the TS system on Heliotron J. The laser beams produced by these two lasers are guided into an optical path obliquely downward to upward where plasma is located at the middle of it. The reason for constructing such kind of oblique optical path is because of the configuration of Heliotron J where large helical coils are winding around the vacuum vessel, which severely limits the configuration of the components. Moreover, two large basement structures located above and below the vacuum vessel to

support the vertical coils and the inner vertical coil mounting around the central axis of the torus are also limiting the space for constructing

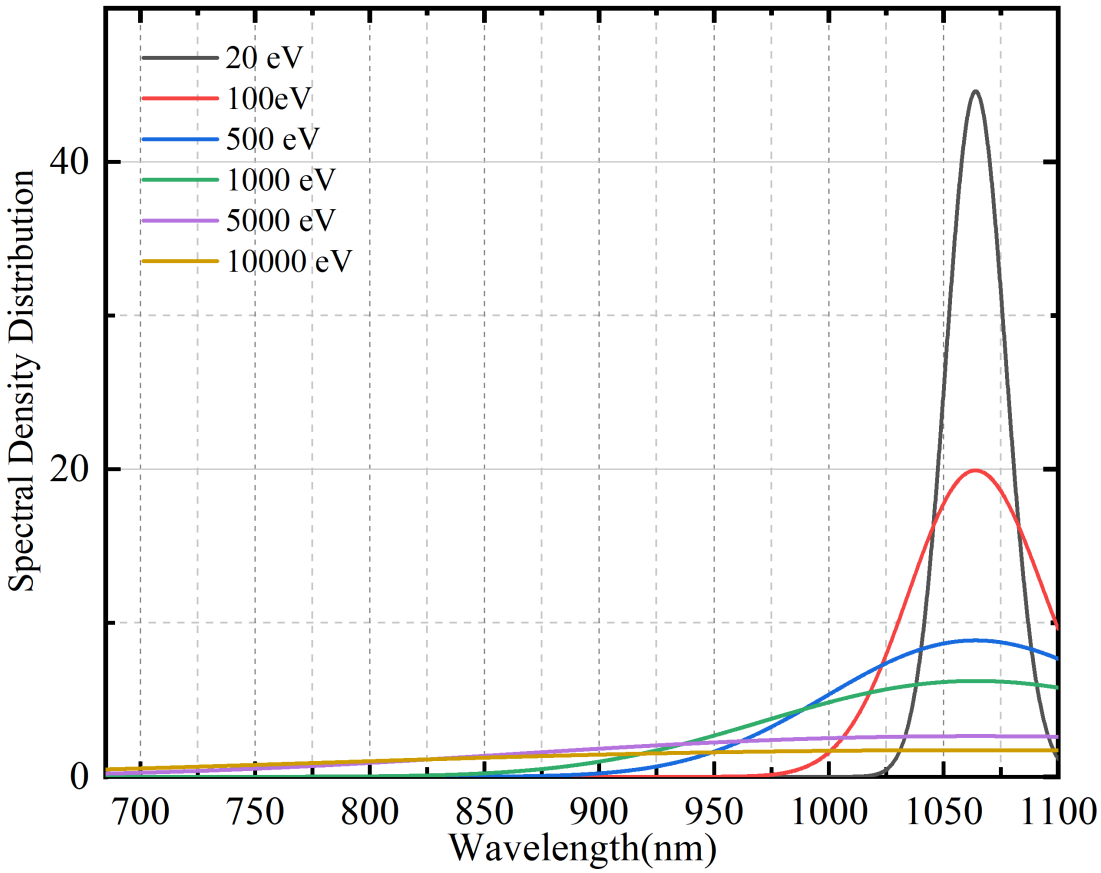

Fig 4.2: Thomson scattered spectra for 160° scattering.

the optical path. In this case, only such kind of oblique path can let the beams pass through plasma as much as possible without getting blocked by any objects. The laser beams will be focused by a plane-convex lens (f=2544mm) at the center of the plasma to improve the signal-to-noise ratio of the scattered light from the plasma. A 160° scattering is formed in such kind of configuration of the optical path. Such kind of large scattering also has the advantage that spectral density distribution is distributed more evenly on a wide range of wavelengths compared with 90° scattering. The typical Thomson scattered spectra for YAG wavelength(1064 nm) at 160° scattering from 20 eV to 10 keV are plotted in Fig. 4.2 with consideration of the depolarization effect. Before the beams reach the plasma and after the

beams pass through the plasma, they need to pass through a long vacuum pipe so that the stray light from reflections at the input and output vacuum windows of Heliotron J can be reduced. A carbon beam dump is installed on the top of Heliotron J to absorb the laser beams after the beams pass through the upside vacuum pipe of Heliotron J. The beam dump is set at a distance away from the vacuum pipe so that stray light can be reduced.

On the other hand, lasers' power is monitored by two power monitors respectively. After the beams are produced, a fraction of the lasers' power will be guided to a beam sampler and power monitors in sequence. The power monitor is made up of an integrating sphere and a silicon photodiode used for correcting the beam power fluctuation to the detected scattered light. The basic performance of this system is given in Table 4.1.

4.3 Light collection optics

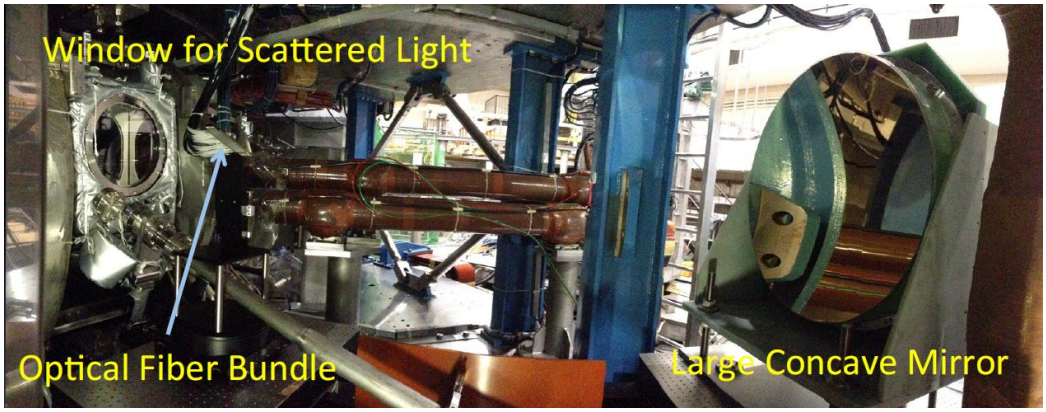

Fig. 4.3: Light collection optics of Heliotron J.

Light collection optics is used to collect scattered light produced from scattering volumes that are distributed along the optical path. It consists of a concave mirror and optical fiber bundle, as shown in Fig. 4.3. The scattered light is collected with a large concave mirror (D=800 mm, f=2.25) with a solid angle of ~80–100 msr. The collected scattered light is transferred to the 25 polychromators by the optical

fibers that one side is lined up on the image of the scattered light and another side is plugged into the polychromators. As shown in Fig. 4.4, each entrance of the fiber bundles is lined up in a staircase pattern, which is used to reduce the loss of a coupling of the fiber and the scattered light from the collected mirror. The main reason for the coupling loss is that the entrance of the optical fiber is partially covered by the next fiber. An aberration on the image is $1 \sim 2.5$ mm[20]. The required numerical aperture of the fiber is less than 0.3. Therefore, a polymer-clad optical fiber bundle made by Mitsubishi cable industries LTD (3 mm × 1.5 mm, $NA = 0.39$, number of core wires is 12) is chosen for the transformation of the scattered light. The NA is expressed as

$$NA = n\sin(\theta) \tag{4.1}$$

$$NA = \sqrt{n_1^2 - n_2^2} \tag{4.2}$$

where n_1 and n_2 are the refractive indices of the fiber core and the clad. The magnification of the image is $0.3 \sim 0.4$, then the plasma profile is measured with ~ 10 mm resolution if the 25 measuring points are set on the image.

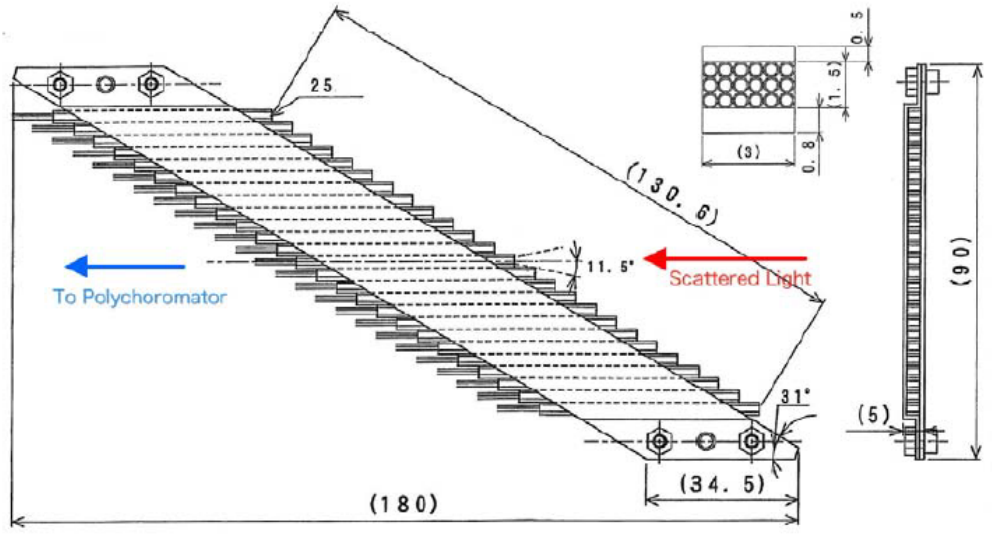

Fig. 4.4: Schematic of the optical fiber bundle in a staircase form for the collection system[60].

4.4 Spectroscopic system

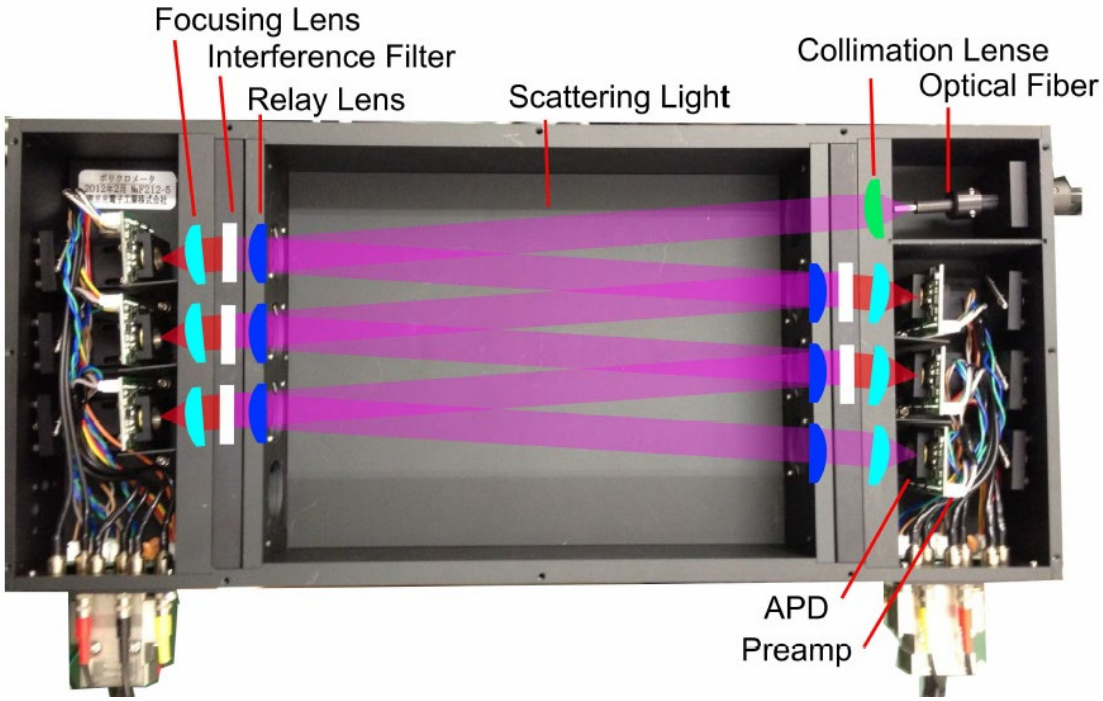

Fig. 4.5: The inner construction of the interference-type polychromator.

The spectroscopic system is used to detect scattered light for further analysis of T_e and n_e, which is made up of 25 polychromators. Each polychromator corresponds to one observation point in the plasma. The polychromator is an interference filter type, as shown in Fig. 4.5. Each of them consists of 5 channels to detect Thomson scattered light and 1 channel for calibration of Rayleigh scattering. Each channel is made up of an interference filter, avalanche photodiodes (APD; Hamamatsu photonics K.K., S 8890-30), optical fiber attachment, relay lens, focusing lens, and pre-amplifiers. After the scattered light is transmitted through the optical fiber, it is guided by the relay and focusing lenses to the 5 channels in sequence. Each filter set in front of the channel has a specific pass-waveband that only the scattered light with a wavelength matching it can pass through the filter and then be detected by the APD set behind the filter. When the scattered light passes through the filter and irradiates on the PN

junction of the APD working in a linear mode by applying reverse voltage, reverse current caused by photo-induced carriers can be produced. Because the equivalent circuit of an APD could be simplified as a first-order circuit, the waveform of the reverse current will follow an exponential law as the output of the first-order circuit. The circuit diagram of the APD pre-amplifier for the polychromator is shown in Fig. 4.6. The produced reverse current passing through a series resistor connected after the APD with a high resistance of 10 $k\Omega$ forms a voltage signal, which is used as the input of the preamplifier circuit. Finally, the preamplifier for each APD has two outputs: a directly coupled channel to measure the background light and a high-pass channel, which reduces the background light by using an RC filter, to measure the scattered laser pulses.

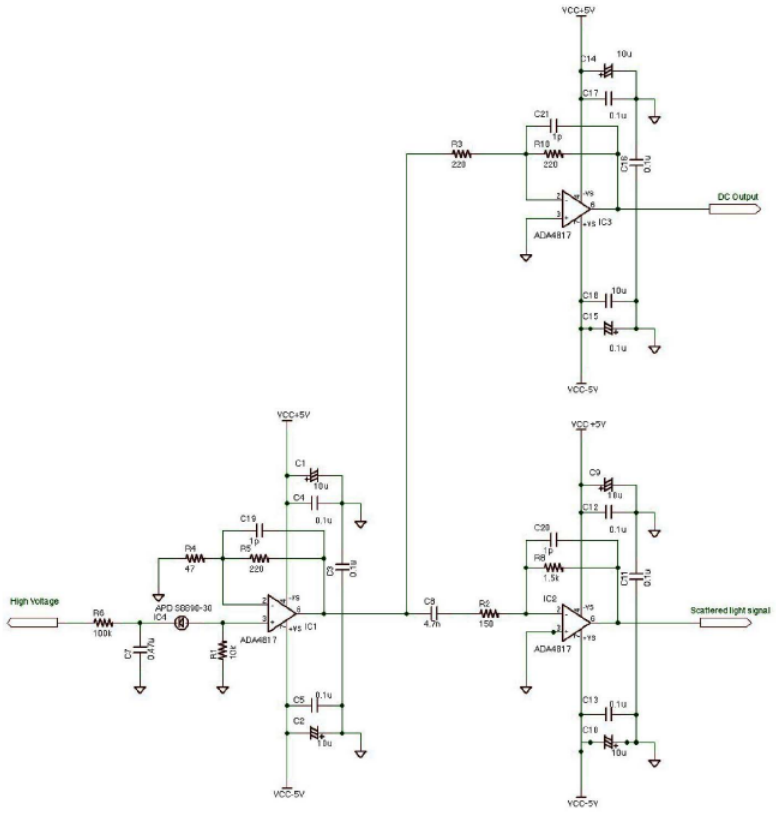

Fig. 4.6: Circuit diagram of the APD pre-amplifier for the polychromator[60].

The scattered power irradiated on the PN junction of the APD can be quantitatively described by the output signal of the APD. Also, this scattered power determines how many scattered photons get detected. The photon detected by channel i per second can be estimated, which is written as

$$N_i = n_e \Delta L \frac{\lambda_i E_i}{hc} \Delta\Omega_s \int_{\epsilon_{iL}}^{\epsilon_{iH}} S_T(\varepsilon, \theta, 2\alpha)\eta(\epsilon)T(\epsilon)d\epsilon \qquad (4.3)$$

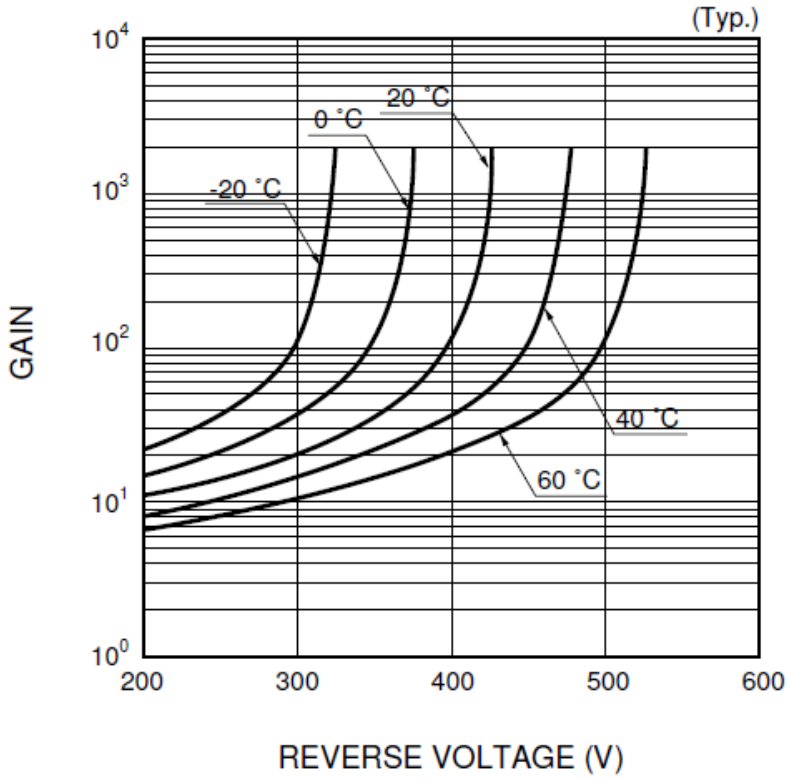

Fig. 4.7: Avalanche gain of the S8890 APD as a function of the reverse voltage at different temperatures.

where ΔL is the length of the scattering volume; Ω_S, solid angle of scattering; E_i, total energy of incident radiation; θ, scattering angle; h, Planck constant; c, speed of light; $\eta(\epsilon)$, quantum efficiency; $T(\epsilon)$ is total optical transmission; $\alpha = m_e c^2/2T_e$, and $S_T(\varepsilon, \theta, 2\alpha)$ represents the scattered power per unit solid angle per unit wavelength shift, which is calculated by equation (3.106). ϵ_{iL} and ϵ_{iS} are calculated as

$$\epsilon_{iL} = \frac{\lambda_{sL} - \lambda_i}{\lambda_i} \tag{4.4}$$

$$\epsilon_{iS} = \frac{\lambda_i - \lambda_{sS}}{\lambda_i} \tag{4.5}$$

where λ_i, λ_{sL}, and λ_{sS} are the wavelengths of incident light, the shortest passable wavelength of channel i, and the longest passable wavelength of channel i. The scattered signal in volts is proportional to the detected scattered photon number, which is given by

$$V_i = GN_i \tag{4.6}$$

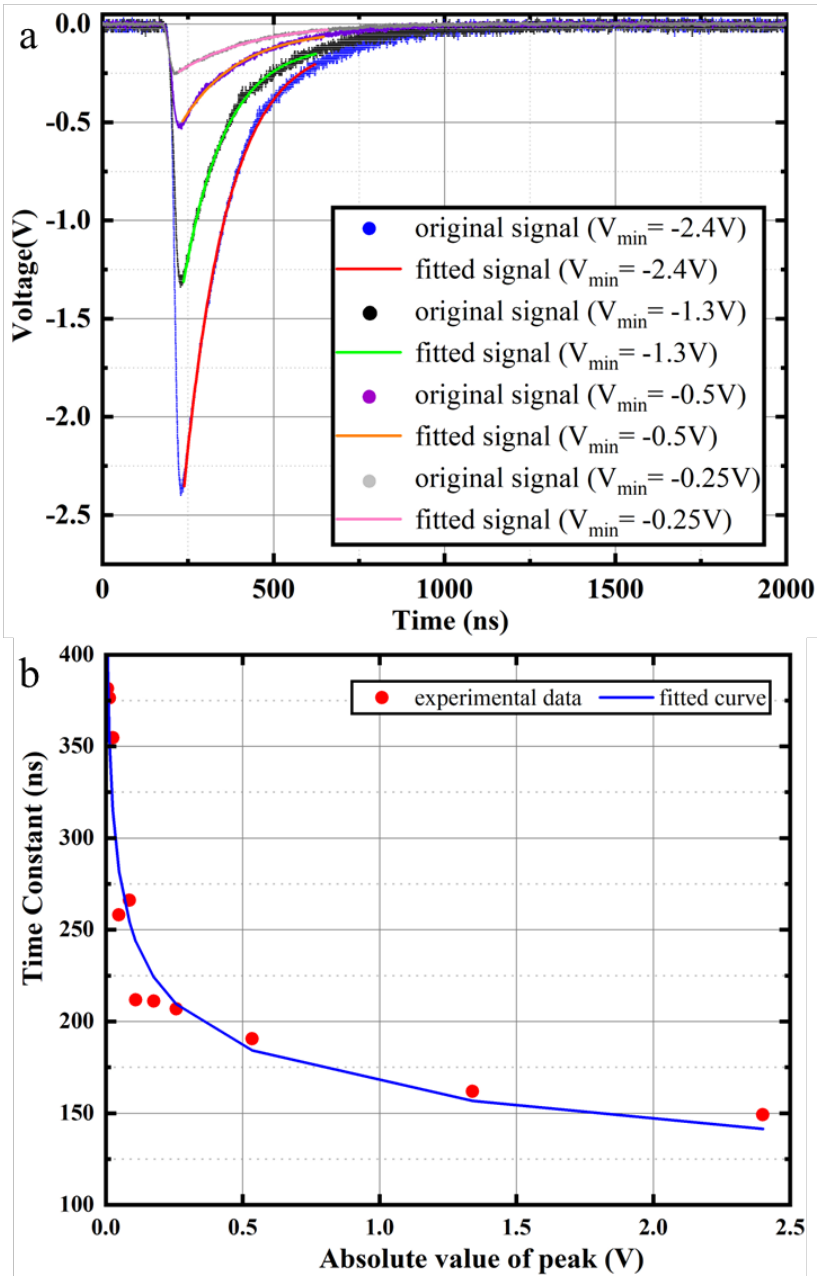

Fig. 4.8: a) The fit of the APD output signal by an exponential function. b) Relationship between the absolute value of the peak and the time constant.

where G is the gain of the APD. The gain of the APD is given by the manufacturer, as shown in Fig. 4.7. As mentioned above, the signal in terms of scattered photons per second is related to the digitizer signal in volts by the gain G of the combined detector system. Because this gain is highly dependent on the temperature, temperature-induced changes in the sensitivity by feedback control of the bias voltage from a regulator (Matsusada Precision Inc. HAPD-0.8PT) based on the temperature monitor are attached to the APD for compensation[39]. Based on the linearity of the APD sensitivity to a pulsed input, which has been confirmed in our previous work, the integration of the waveform caused by a scattering event is used to judge the intensity of the scattered power. With the existence of the regulator, linear APD sensitivity for a pulsed input can be better maintained, which makes the measurement more reliable.

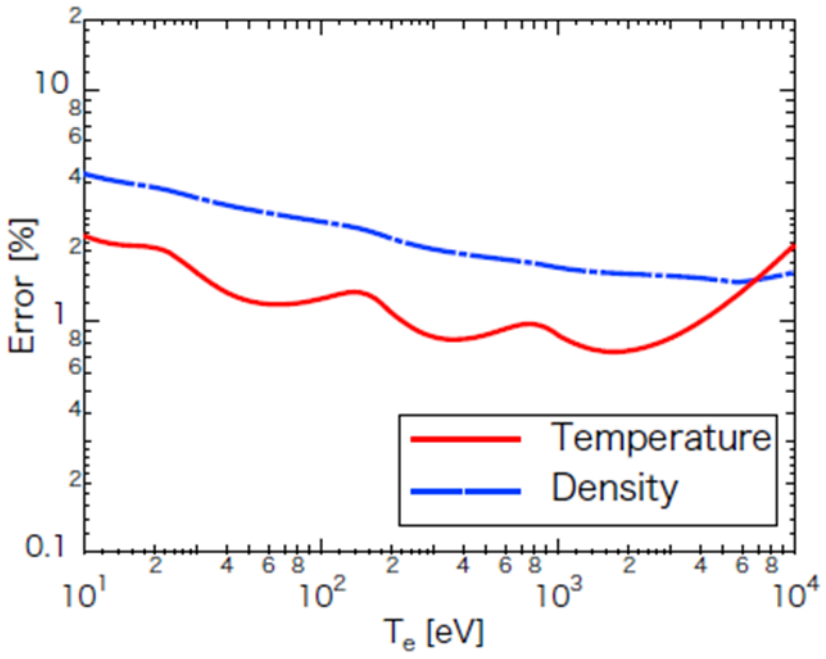

Fig. 4.9: Error of T_e and n_e as a function of T_e.

To calculate the integration of the output signal of a waveform, the integration period is necessary to be considered. To investigate the relationship between the peak of the waveform and the decay time of the signal, Nd:YAG laser pulses are damped by laser attenuators and guided to irradiate an APD inside the polychromators. From Fig. 4.8, it can be confirmed that the waveform of the output signal follows an exponential function form as the output signal is coming from the APD with an equivalent circuit as a first-order circuit. Moreover, it can be seen that the waveforms fitted from the peaks of the raw waveforms have a good agreement with the raw waveforms. The fitted equation of the waveform from the peak of a raw waveform is given as:

$$S_f(t) = a \cdot exp\left(\frac{t - T_{peak}}{\tau}\right) \tag{4.7}$$

where a is the magnitude of the signal, T_{peak} is the timing corresponding to the peak value. τ is the time constant of the signal. Fig. 4.8 b shows the relationship between the decay time and the absolute value of the peak. As the absolute value increases, the decay time becomes larger, which leads to a longer integration period for a complete waveform. A typical integration period of the output signal on our system is ~400 ns from the peak value.

In our system, the pass-waveband distribution of five channels in each APD is determined according to the expected T_e range (10eV-10keV) of Heliotron J[20]. The highest T_e that can be reached by Heliotron J in the core region of plasma is up to ~10 keV. On the other hand, the lowest T_e at the edge of plasma can be as low as ~10 eV. To optimize the distribution for T_e measurement with the T_e range that can be realized by Heliotron J, the following assumptions are made. The solid angle and scattered volume length are calculated as $\sim 80 - 100$msr and 300 mm, respectively. The amount of the background light is calculated from plasma bremsstrahlung. The plasma n_e is assumed to be 3×10^{19} m^{-3} that is a typical plasma in Heliotron J. The filter pass-waveband distribution is optimized as follows:

(1) channel 1: 700–845 nm;
(2) channel 2: 845–960 nm;
(3) channel 3: 960–1025 nm;
(4) channel 4: 1025–1050 nm;
(5) channel 5: 1050–1060 nm;

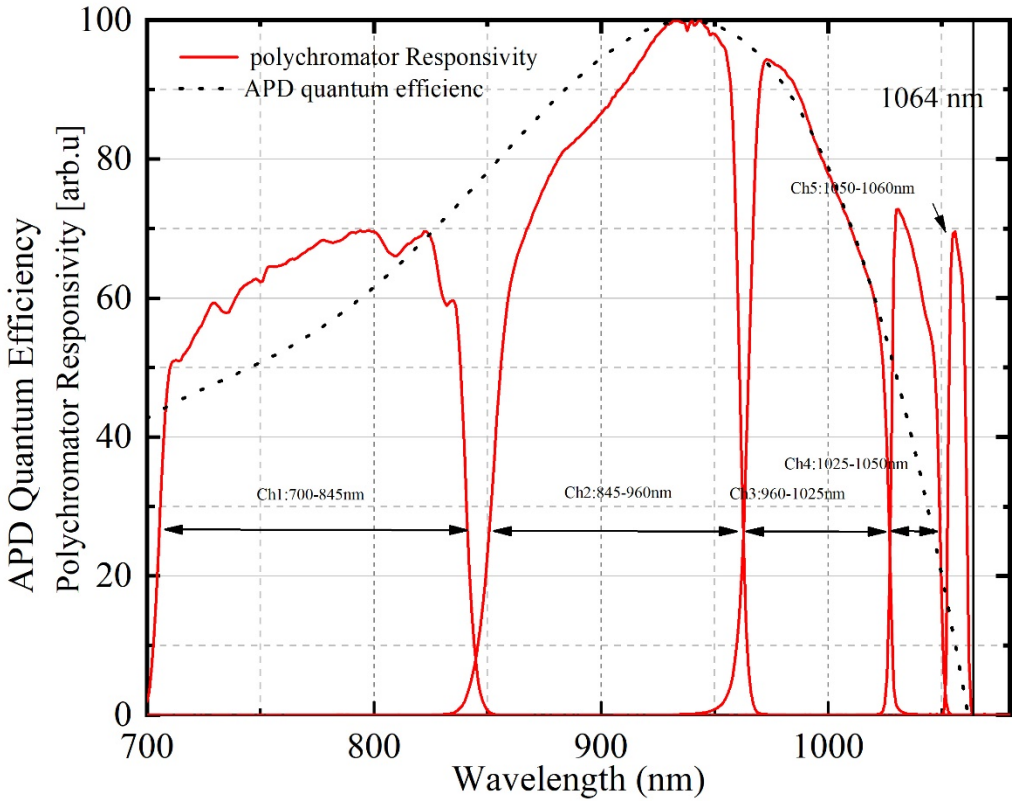

Fig. 4.10: The responsivity of the polychromator averaged by 25 polychromators.

The result of the perfo rmance estimation as a function of T_e is shown in Fig. 4.9. The error of the T_e measurement is below ~ 2% from this T_e range. Although the error of the n_e measurement (~ 3%) is larger than that of T_e, the value is enough for achieving our experimental objectives. The spectral responsivity of the five wavelength channels averaged by 25 polychromators is shown in Fig. 4.10. The polychromator responsivity is the combination of the quantum efficiency of APD and the total optical transmission. It can

be seen that all five filters are set on the blue-shift side because of the low quantum efficiency of the APD on the red-shift side.

4.5 Data Acquisition System

A real-time VME computer system is used for a data acquisition system. The VME bus, with a throughput of 30 Mbyte/sec, forms the basis of the system. The central processing units (CPUs) employed are Motorola 68060 running at a clock rate of 60MHz. The system operates using the CINOS (CHS Integrated No Operation System), initially developed for CHS data acquisition. CINOS functions as a system software rather than a multitasking operating system, allowing for time-invariant data acquisition without an OS. The acquired data is subsequently transferred to a computer via a LAN for immediate analysis following a plasma discharge. The voltage signal as the output of APD pre-amplifier circuit is transformed into ADC count for analysis.

Chapter 5

Design of a dual scattering angle multi-pass Thomson scattering system with signal separation function on Heliotron J

5.1 Overview

The motivations for constructing the MPTS system with signal separation function on Heliotron J are for anisotropy measurement and enhancement of scattering signal intensity from low-density plasmas. Except for realizing an enhancement of scattering signal intensity from low-density plasmas as a conventional MPTS system installed on other nuclear devices, this newly designed MPTS system solved a signal overlap problem existing on the MPTS system of Heliotron J by extending the incident interval between two adjacent incidences when the newly added signal separation function is under operation. Moreover, an over-expanded beam radius can be confined during the propagation of beams in the optical path. Additionally, the measurement accuracy of T_e corresponding to both scattering angles is enhanced simultaneously.

In this chapter, the development of a new dual scattering angle multi-pass Thomson scattering system with signal separation function on Heliotron J is described. The reason why signal overlap exists in the MPTS system on Heliotron J is explained in section 5.2. The design of the incidence optics and the spectroscopic system of this MPTS system are given in sections 5.3 and 5.4 respectively.

5.2 Signal overlap

The reason why a signal separation function is added to the MPTS system on Heliotron J compared with a traditional MPTS system without it is given in this section. It's mainly used to solve the signal overlap existing in the MPTS system of Heliotron J so that anisotropy measurement can be carried out. In the original design of the MPTS system on Heliotron J[61], as shown in Fig. 5.1, one 50 Hz Nd:YAG laser is used as the probe; The reason why only one laser is used here instead of two used in the single-pass system is that our MPTS system is a polarization controlled type that the Pockels cells used in our system can only be aligned for one laser. As same as the single-pass system, the laser beam is guided upward into a vacuum vessel with a 20º angle to the horizontal plane to keep the optical path of the laser beam away from the helical coils twisting around the vacuum vessel. In such a configuration, the beam is obliquely upwardly guided into plasma and produces a backward scattering with a scattering angle equal to ~160º during the interaction with plasma. After the incident beam passes through plasma, it is immediately reflected towards the plasma, following the same optical path, but in the opposite incident direction by a mirror set atop Heliotron J. The reflected beam transmits through the plasma obliquely downward, to produce a forward scattering with a 20º scattering angle. Because the optical paths of the normal and the reflected beams are aligned coaxially, scattered lights are produced from the same scattering volume where the normal or reflected beam interacts with plasma. Both the scattered light corresponding to the 160º and 20º scattering is collected by the concave mirror and sent to a polychromator via optical fibers. After the scattered light is transmitted into a polychromator, it is finally detected by the APD and output as a voltage signal. However, the decay time of the scattered light signal with an exponential function waveform is much longer than the incident interval of tens of nanoseconds between an upward

incidence corresponding to backward scattering with 160º scattering angle, and a downward incidence corresponding to forward scattering with 20º scattering angle. The decay time of the scattered light waveform is proportional to the time constant and the time constant reflects how fast the scattered light signal waveform reduces from peak to 0. The value of this time constant is the product of the capacitance in an equivalent circuit of the APD and the resistance of a series resistor connected with the APD. It can be evaluated by measuring the dependence of the time constant on the peak voltage of the waveform. The time constant of a voltage signal transformed by a series resistor as a function of the peak voltage of the scattered light signal has been fitted as a non-linear curve. This curve shows that the time constant is approximately 250–400 ns when the peak voltage is approximately 0.01–0.1 V, this is a normal value as seen in our previous experiment[20,39,60] as shown in Fig. 4.8. The APD in our system develops a large time constant because of the 10 $k\Omega$ resistance of the series resistor connected after APD, as shown in Fig. 4.6. The purpose of choosing a large resistance is to achieve a high signal-to-noise ratio even when noise is introduced by the secondary amplifier circuit later. Because our system has a very high time constant, in this case, before the waveform of the scattered light signal corresponding to the input laser beam decays to 0, the scattered light corresponding to the reflected laser beam irradiates on APD, and the signal corresponding to this forward scattering overlaps with the waveform of the former. Therefore, the signal corresponding to either scattering direction cannot be analyzed separately.

As an attempt to analyze the overlapping signals, one solution for overcoming this issue is extending the length of the optical path because scattering events can be produced in a delayed time and so are corresponding scattered light signals. However, the layout space provided for TS is limited and the extension of the optical path to realize a longer incidence interval for separated analysis on scattered

light signals is not easy. To extend an incident interval of 100 ns, the length of the optical path must be 30 m as a simple geometric relationship between traveling distance and speed of light, which is an impossibly long distance to set up atop Heliotron J. Therefore, to extend the incident interval but not simply extend length of optical path, a polarization-based MPTS system with signal separation function is constructed on Heliotron J to realize an extended optical path by a compact layout in a limited room.

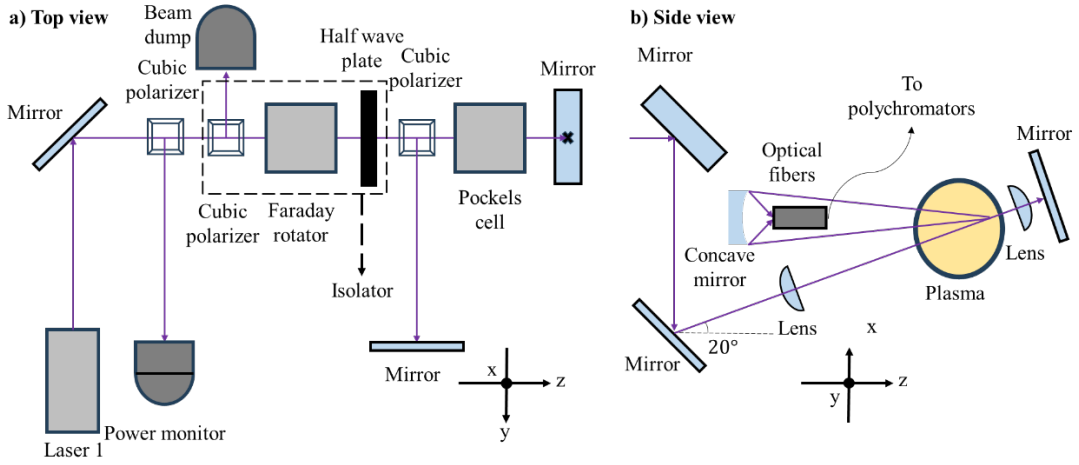

Fig. 5.1: Schematics diagram of the original MPTS system based on polarization-controlled devices on Heliotron J[61].

5.3 Incidence optics

Incidence optics of this new MPTS system with signal separation function is used to build optical path so that the laser beam can be guided into plasma, confined in a specific optical path, and recycled. It is made up of a polarization optical system, a trigger system, and two image relay systems[61].

5.3.1 Polarization optical system

The polarization optical system is used to confine the laser beam in a specific optical path to realize the multi-pass function or signal

separation function. Optical components including one isolator, three polarizers, and two Pockels cells (PC) are set in the optical path to realize these two functions. The function of these components is given below.

Isolator

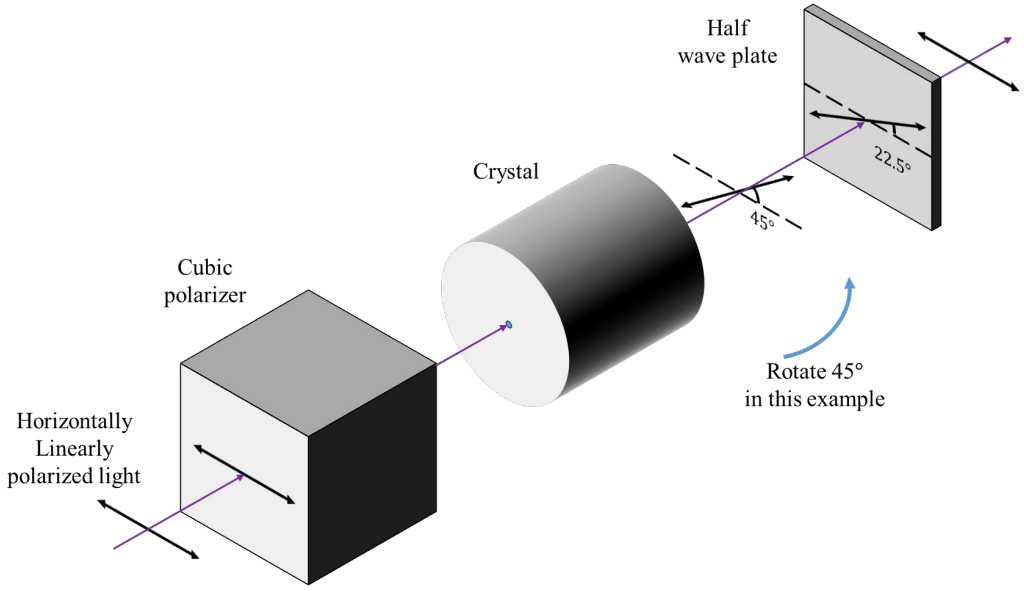

Fig. 5.2: An example of how an isolator changes the polarization status of a linearly polarized light.

An isolator is made up of a Faraday rotator, polarizers, and a half-wave plate. The Faraday effect of an isolator can be used to realize polarization-controlled behavior. The Faraday effect causes a rotation of the plane of light polarization when a light beam passes through a material in the presence of an axial magnetic field. Compared with the effect of optical activity, the rotation angle is not dependent on the direction of propagation through the medium. Light passing one way through the medium will be seen by an observer as having its polarization axis rotated through a clockwise angle for example[62]. If the light is retro-reflected back through the same medium however, the same observer would again see the light polarization axis rotate through an additional, equal clockwise angle (whereas in an optically active medium, the light would have undergone first a clockwise then

an equal anti-clockwise rotation returning it to its original state). How an isolator changes the polarization status of a linearly polarized light is depicted schematically in Fig. 5.2.

Half-wave plate

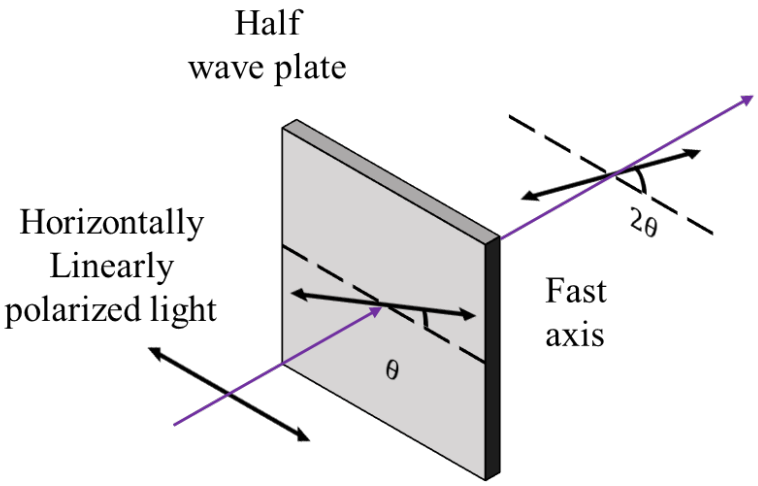

Fig. 5.3: An example of how a half-wave plate changes the polarization status of linearly polarized light.

A half-wave plate is an optical device that can alter the polarization state of light. It consists of a birefringent material, such as quartz or calcite, which introduces a phase difference of half a wavelength between the two orthogonal polarization components of incident light. This phase shift causes a change in the polarization direction of the light. The orientation of the fast axis of the half-wave plate determines the direction and amount of the polarization rotation. If we decompose linearly polarized light into two orthogonal components based on the fast axis, the phase difference between o-ray and e-ray is 0 before the linearly polarized light passes through a half-wave plate. After passing through the half-wave plate, phase difference between o-ray and e-ray is expressed as

$$\delta = \frac{2\pi}{\lambda_0}(n_0 - n_e)d \qquad (5.1)$$

where n_o and n_e represent the principal refractive indices of the crystal for the o-ray and e-ray, respectively, with a vacuum wavelength of λ_o. d is the thickness of the half-wave plate that both rays pass through.

Polarizer

A polarizer is an optical device that selectively transmits light waves of a specific polarization while blocking or attenuating light waves with other polarizations. It is commonly used to control the polarization state of light. A polarizer consists of a material or optical element that has a preferred transmission axis. Light waves aligned with this axis can pass through the polarizer with minimal loss, while light waves polarized in perpendicular directions are absorbed or scattered, resulting in their attenuation. In this study, cubic polarizers are utilized so that a beam can be guided to a specific direction after its polarization direction got changed.

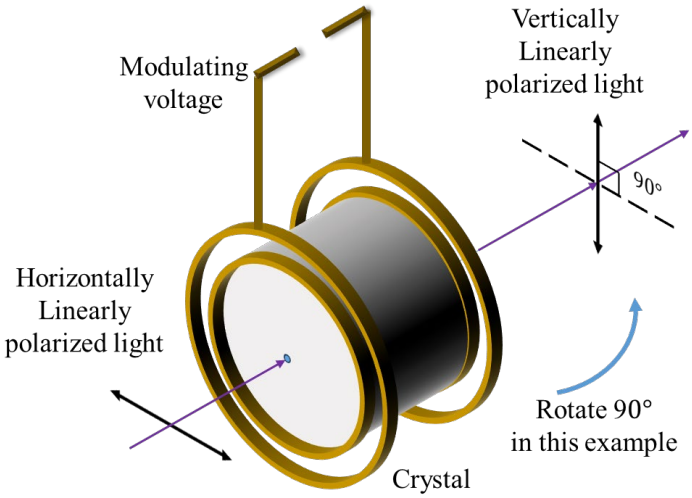

Fig. 5.4: An example of how a Pockels cell changes the polarization status of linearly polarized light.

From the characteristics mentioned above, by setting a polarizer, a Faraday rotator, and a half-wave plate in sequence, a linearly polarized light can be guided to another optical path compared with the original optical path that the light first passes through. In this work, a PAVOS

Ultra Optical Isolator produced by Electro-Optics Technology with an 8 mm diameter is utilized.

Pockels cell

A Pockels cell is an optical device that uses the Pockels effect to control the polarization state of light by applying an electric field. The Pockels effect is an electro-optic phenomenon exhibited by certain crystals, such as lithium niobate (LiNbO3) and potassium dihydrogen phosphate (KDP). When an electric field is applied to these crystals, their refractive index changes proportionally to the applied voltage. This change in refractive index affects the polarization state of light passing through the crystal. In a Pockels cell, a crystal is placed between two electrodes. When an electric field is applied across the crystal, it modifies the polarization state of the incident light. The inner construction of a Pockels cell is shown in Fig. 5.5. By adjusting the voltage applied to the Pockels cell, the polarization of the transmitted light can be controlled. Therefore, a Pockels cell also can be treated as a dynamic retarder. In this study, a Pockels cell (Q1059P12SG-1064, FastPulse Technology) and a high-speed signal generator (series 5046ER E-O system, FastPulse Technology) are utilized.

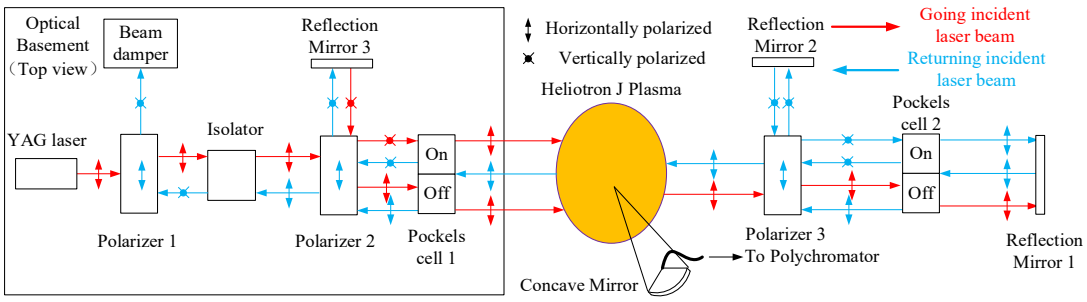

FIG. 5.5: The schematic of the polarization optical system of the MPTS system with signal separation function.

After describing the function of the optical components, the schematic of the polarization optical system of the MPTS system with signal separation function is given in Fig. 5.5. A horizontally polarized laser beam plotted in the red solid line is defined as the incident laser

beam. It is produced by one 50 Hz Nd:YAG laser with a power of approximately 550 mJ and pulse duration of 10 ns measured at its full-width half maximum. It is guided to pass through polarizers 1 and 2 with horizontal transmission direction, isolator, and the 1st Pockels cell at off-state in sequence. During this optical path, although the Faraday rotator causes the polarization direction of linearly polarized light to be at a 45° angle with the horizontal plane., by setting the fast axis of the half-wave plate inside the isolator with 22.5°to the horizontal plane, the polarization direction of the laser beam will be transformed back to parallel to the horizontal plane again after the laser beam passes through the isolator. A Pockels cell (FastPulse, Q1059P12SG-1064), currently operated at off-state, does not affect the polarization status of the laser beam when the beam first passes through it. After passing through the 1st Pockels cell, the beam is obliquely upwardly guided into the plasma at an angle of 20º with the horizontal plane. A laser beam passing through plasma from the left side to the right side causes a scattering with a scattering angle (θ) equal to 160º.

After interacting with plasma, the going incident beam will be guided to polarizer 3 with a horizontal transmission direction and subsequently to the 2nd Pockels cell at off-state. Finally, the beam reaches reflection mirror 1. After being reflected by mirror 1, the laser beam is defined as the returning incident laser beam and plotted by a blue solid line. It is not guided into plasma immediately. Instead, the laser beam will be reflected by polarizer 3 to reflection mirror 2 because the polarization direction of the laser beam is changed from horizontal to vertical, which is realized by switching on the 2nd Pockels cell before the returning incident laser beam reaches it. In our system, two Pockels cells are applied with appropriate voltage to change the polarized direction of the laser beam orthogonally when they are switched on. Under this circumstance, the laser beam is confined in the optical path between reflection mirrors 1 and 2 for several reciprocating trips to extend the incident interval. The optical path

between mirrors 1 and 2 is defined as a signal separation system whose function is extending incident interval so that two overlapping scattered light signals can be separated to some extent. Finally, when two overlapping signals are separated to a certain degree, the 2nd Pockels cell is switched off so that the laser beam can be guided into the plasma again. The returning incident beam causes a 20º scattering (θ = 20º). After the beam passes through the plasma, its polarization direction is again changed to 90º by switching on the 1st Pockels cell so that the beam can be redirected to the plasma. As a result, the returning incident beam cannot pass through polarizer 2 and is reflected to reflection mirror 3. After being reflected by mirror 3, the laser beam is redefined as the going incident beam because it will interact with plasma later to produce a 160º scattering. This process is repeated until the energy carried by the beam is significantly reduced due to the power loss caused by optical components in the optical path. Finally, the beam is guided to the beam dump by switching off the 1st Pockels cell.

Jones calculus is adopted to concisely express the polarization transformation processes mentioned above. It's a mathematical formalism used to describe the polarization state of light and the interaction between optical elements. It is based on the vector representation of light, where the polarization state is represented by a complex two-dimensional vector called the Jones vector. The Jones vector consists of two components that represent the amplitude and phase of the light. The Jones matrices of the half-wave plate (HWP), Faraday rotator (FR), Polarizer (P), and Pockels cell during the operation period (PC) are listed below.

$$P = \begin{bmatrix} 1 & 0 \\ 0 & 0 \end{bmatrix} \tag{5.2}$$

$$FR = \begin{bmatrix} \cos\left(-\frac{\pi}{4}\right) & \sin\left(-\frac{\pi}{4}\right) \\ -\sin\left(-\frac{\pi}{4}\right) & \cos\left(-\frac{\pi}{4}\right) \end{bmatrix} \tag{5.3}$$

$$HWP = \begin{bmatrix} \frac{1}{\sqrt{2}} & \frac{1}{\sqrt{2}} \\ \frac{1}{\sqrt{2}} & -\frac{1}{\sqrt{2}} \end{bmatrix} \tag{5.4}$$

$$PC = \begin{bmatrix} \cos 2\theta & \sin 2\theta \\ \sin 2\theta & -\cos 2\theta \end{bmatrix} \tag{5.5}$$

where θ is equal to 45°, and the polarization status of laser light before passing through polarizer 1 is defined as P0 with the polarization direction parallel to the horizontal plane, which is $\begin{bmatrix} 1 \\ 0 \end{bmatrix}$.

The polarization states in a complete journey from Polarizer 1-Mirror 1-Polarizer 1 can be written as

$$\mathrm{P1} \cdot \mathrm{FR} \cdot \mathrm{HWP} \cdot \mathrm{P2} \cdot \mathrm{P3} \cdot \prod_{1}^{N} \cdot \left[\mathrm{P3} \cdot \mathrm{PC1} \cdot \mathrm{PC1} \cdot \mathrm{P3} \cdot \prod_{1}^{n} (\mathrm{PC2} \cdot \mathrm{PC2} \cdot) \right] \cdot \mathrm{P3} \cdot \mathrm{P2} \cdot \mathrm{HWP} \cdot \mathrm{FR} \cdot \mathrm{P1} \cdot \mathrm{P0} = \begin{bmatrix} 0 \\ 0 \end{bmatrix} \tag{5.6}$$

Where *N* and *n* are how many times the laser beam reciprocates in the optical path between mirrors 1 and 3 and the optical path between mirrors 1 and 2. The outcome is $\begin{bmatrix} 0 \\ 0 \end{bmatrix}$ which means the beam is reflected to the beam dump and nothing passes through Polarizer 1 anymore.

Fig. 5.6 shows the scattering configuration of going incidence with a scattering angle equal to ~160° and returning incidence with a scattering angle equal to ~20° respectively. Noted that the spectral density distribution function of scattered light is deduced from equation (3.94) based on the coordinate system shown in Fig. 3.6. Therefore, scattered light produced from the going incidence and returning incidence can reflect the electron velocity in the direction of vector *k*. Moreover, when the ideal conditions for measurement are satisfied, which are the sum of the two scattering angles is 180°, and the magnetic field is parallel to the bisector of the angle formed by the

direction of laser propagation and the line of sight or is perpendicular to this bisector. One of the spectra of scattered light predominantly reflects the electron temperature parallel to the magnetic field, and the other spectrum predominantly reflects the electron temperature perpendicular to the magnetic field[63].

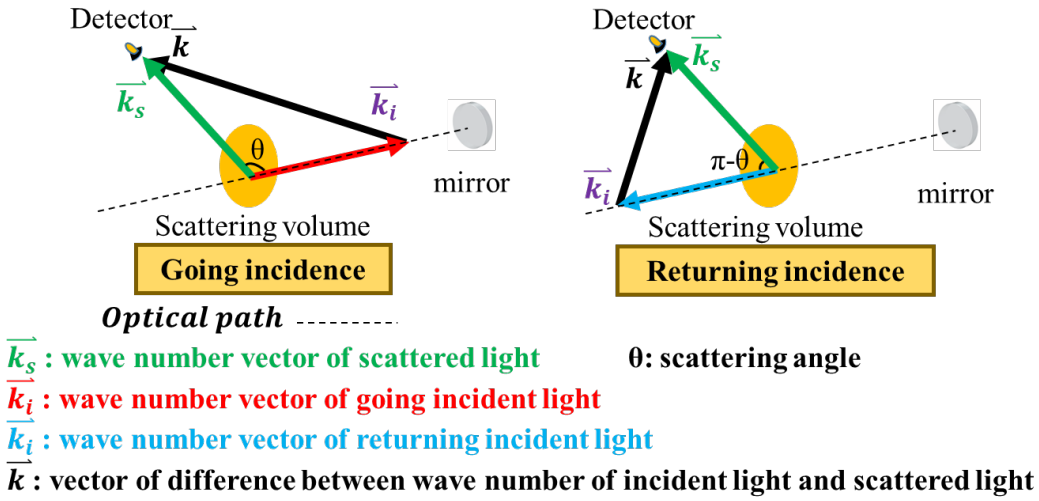

Fig. 5.6: Scattering configuration of the MPTS system on Heliotron J.

By controlling the operation period of the 1st Pockels cell, the traditional function of MPTS systems can be realized when the laser beam is confined in the optical path between mirrors 1 and 3. Conversely, by controlling the operating period of the 2nd Pockels cell, the duration of confining the laser beam to the optical path between mirrors 1 and 2 can be controlled, which allows for extending the incident interval between the going incidence and its successive returning incidence. In this study, the incident interval is extended up to the sum of the time taken by the laser to transmit between plasma and mirror 1 and the time taken by the laser to transmit in the round trip between mirrors 1 and 2. The incident interval t_i can be calculated as

$$t_i = \frac{\left(2 \times D_{plasma\ to\ M1} + n \times 2 \times D_{M1\ \mathrm{to}\ M2}\right)}{c} \qquad (5.7)$$

where $D_{plasma\ to\ M1}$ and $D_{M1\ \mathrm{to}\ \mathrm{M2}}$ are the distance from plasma to mirror 1 and the distance from mirror 1 to mirror 2 respectively. c is the speed of light. n has the same meaning as shown in equation (5.6) how many times the laser beam reciprocates in the optical path between mirrors 1 and 2.

5.3.2 Trigger system

The trigger system is used to control the optical components in the polarization optical system so that the laser beam can be confined in the specific optical path to realize multi-pass or longer incident intervals. Because a beam can propagate in meter level distance in an optical path within nanosecond level time. A wrong or unprecise trigger timing can lead the beam guided into the beam dump directly instead of realizing multi-pass travel. As a result, the correct trigger timing for switching on or off Pockels cells in MPTS systems becomes very important to avoid energy loss. Among the optical components of the MPTS system, only the laser and the Pockels cells can be controlled remotely by external triggers. The connection of the trigger system and the names of the signals are shown in Fig. 5.7. During a plasma discharge, the Nd:YAG laser and Pockels cells operate Synchronizly under the control of the timing controller. The Nd:YAG laser will be operated in four states in sequence after it receives the corresponding trigger signals from the timing controller[59]. These four states are standby, flash, switch on, and shutter. In the standby state, power is supplied to the laser unit. In the flash state, the flash lamp is operating. In the Q switch state, the Q switch operation is started and a laser pulse with length of about 10 ns and frequency of 50 Hz is generated. Lastly, the shutter of the Nd:YAG laser will be opened after the timing controller receives the plasma discharge trigger so that the laser can be injected into the optical path.

The Q switch signal is used to synchronize the Nd:YAG laser machine and the Pockels cell. To trigger the Pockels cells existing in the optical path switch on or off at the right timing, the Q switch signal is also sent to the signal generator DG535 (Stanford research system). After receiving the Q switch signal from the timing controller, the DG535 will send a signal to activate the 5046ER as the controller of the Pockels cell. After receiving the trigger from the DG535, the 5046ER will send a high voltage on or off signal to the Pockels cell for switching on and off. After receiving on signal, the Pockels cell will be switched on until it receives an off signal.

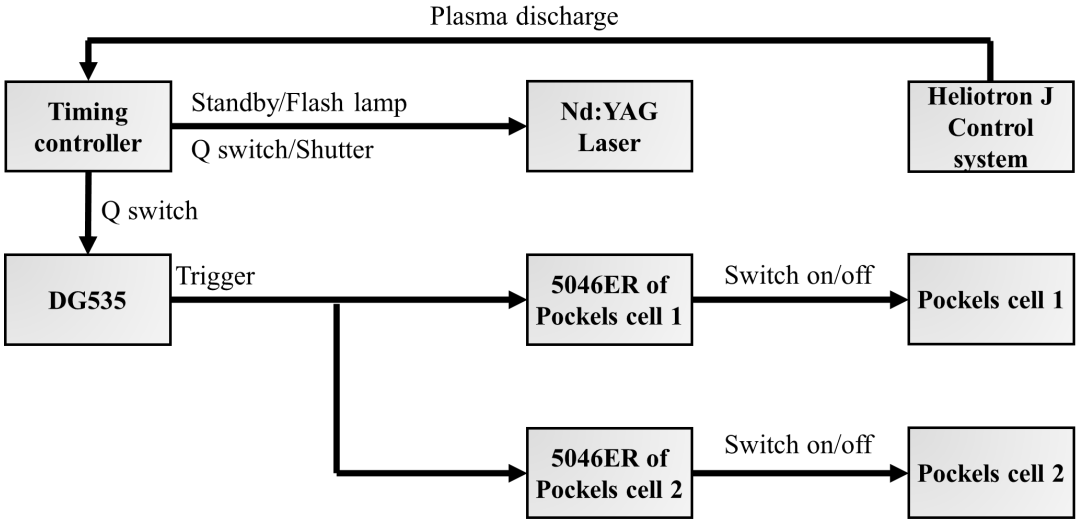

Fig. 5.7: The connection of the trigger system.

The timing of switching on or off the Pockels cells is the key issue to avoid energy loss, which is determined by the position of the Pockels cells in optical path. That's because the position of Pockels cells determines how long time laser beam or trigger signal can be transferred to it. The position of Pockels cells is further determined by the pulse width of laser machines and the response time of signal generators. Due to the existence of pulse width, in this system which is 10 ns, each Pockels cell can't be set too near to mirror 1. That's because, in a vacuum or air, where the refractive index is approximately 1, the laser will travel approximately 3 meters in the

optical path during a 10 ns pulse. Therefore, to avoid the energy loss of a laser beam, the length of a round trip of the optical path between any Pockels cell and mirror 1 should be kept over 3 m because the propagation of the Nd:YAG laser beam existing in the optical path is 3 m. On the other hand, due to the existence of the response time of signal generators, how long time signal can be transferred to Pockels cells needs to be considered with the time the laser beam travels from laser export to Pockels cells. Although the response time of each controllable device is nanosecond level, a beam can propagate a distance at a meter level in the optical path. The response time of the Q switch in the laser machine, DG535, 5046ER is measured by an oscilloscope, which are ~655 ns, ~77ns, and ~100ns respectively. As we see the laser machine has the longest response time, which is also the reason why we don't let the Q switch signal produced by the timing controller directly send to the 5046ER. Because the long response time of the Q switch in the laser machine is larger than the sum of the response time of 5046ER and the longest delay time settable by the 5046ER, the trigger signal will be sent to the Pockels cells in advance of the arrival of the laser beam at the Pockels cells, which results in an advance operation of the Pockels cells and energy loss. Therefore, the DG535 is utilized to extend the transfer time of the Q switch signal from the timing controller to the Pockels cells because it can provide a delay time achievable from picosecond level to thousand second level.

After roughly determining the position of two Pockels cells based on the pulse width and the response time of each signal generator, the trigger sequence of the system can be qualitatively determined. The trigger sequence, response time, and operating period of each Pockels cell are provided in Fig. 5.8. It should be noticed that specific values can only be determined after Gaussian beam analysis, which is given in the next section. The trigger timing for each Pockels cell is chosen as the tail of the beam leaves the Pockels cell for the first time. Refer

to Fig. 5.5 and equation (5.6), the operating period of each Pockels cell are determined by N and n, which are how many pass number realized by the system and how many reciprocating trips traveled by the laser beam in the optical path between mirror 1 and 2. D means the distance between two optical components described in the subscript. All of these parameters have the same meaning as mentioned in equation (5.7). It should be noticed that the transmission time consumed in cables is not indicated in Fig. 5.8. The time consumed in the transmission in a cable is ~5ns per meter, which should be considered depending the length used in the system.

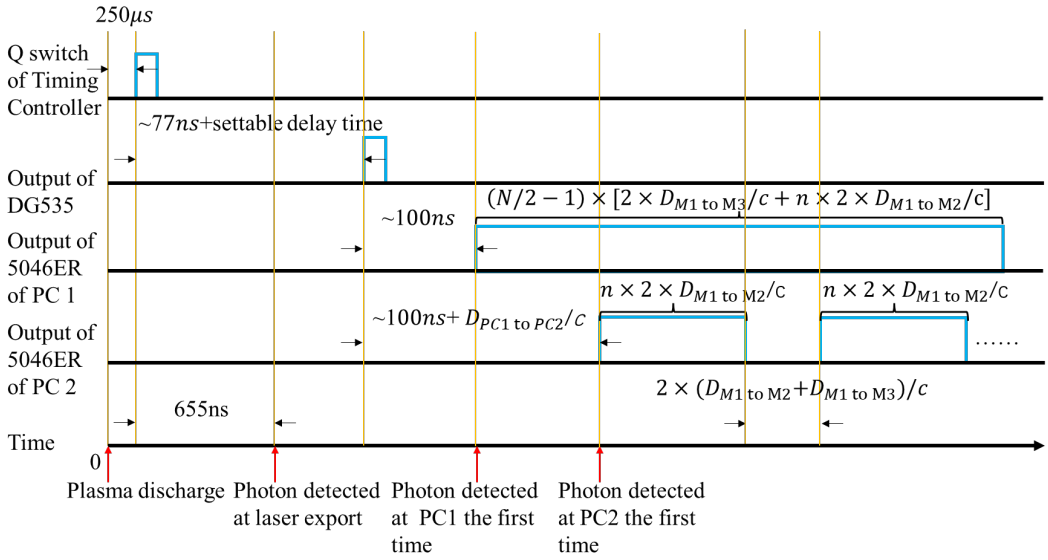

Fig. 5.8: Trigger sequence of the MPTS system with signal separation function on Heliotron J.

Two functions that are multi-pass function and signal separation function can be realized by adjusting the parameters N and n as shown in Fig. 5.8 so that the laser beam can be confined in the specific optical path indicated in Fig. 5.5. When N is set as an even number and n is set as 0, only multi-pass function can be realized that beam will reciprocate in the optical between mirror 1 and 3. In this case, incident interval between a going incidence and a returning incidence will not be extended. When N is set 0 and n is set as an even number, only

signal separation function can be realized that the returning incident beam defined in Fig. 5.5 and Fig. 5.7 won't be injected into plasma directly but reciprocating in the optical path between mirror 1 and 2. When both *N* and *n* are set as an even number, both multi-pass mode and signal separation mode can be realized.

5.3.3 Image relay system

The image relay system is used to confine the beam radius or density power so that these parameters will not over the limit of optical components. The evolution of spot size and power density of the laser beam are two preconditions that must be calculated before determining the position of the optical components in the optical path. The spot size of the beam is defined as the radial distance from the center point of maximum irradiance to $1/e^2$ of the maximum irradiance. Because the laser beam follows the characteristics of a Gaussian beam during its propagation, the spot size varies continuously and expands following the profile of hyperbolic shape. The evolution of the spot size and radius of curvature of the laser beam as a function of the distance of its propagation (after it leaves the output of laser head) are given below:

$$w^2 = w_0^2 \times \left[1 + \left(\lambda_i \times \frac{(z - z_0)}{\pi \times w_0^2}\right)^2\right] \tag{5.8}$$

$$R = z \times \left[1 + \left(\pi \times \frac{w_0^2}{\lambda \times (z - z_0)}\right)^2\right] \tag{5.9}$$

where, z and z_0 are the distance of the beam's propagation from the laser head and position of the waist radius, respectively, w and w_0 are the spot radius at distance z and waist radius of the Gaussian beam, respectively; and R is the radius of curvature at position z.

During propagation through a long optical path proposed by our system, the spot size of the laser beam expands to a much larger size than its original size at the output of the laser head. As a result, it may not only exceed the entrance size of a few optical components used for

controlling the polarization status of the laser beam, such as Pockels cell with an 8 mm diameter entrance and isolator of 6 mm diameter as proposed in our system, but also result in a poor signal-to-noise ratio when detecting scattered light signal. The reason behind the latter phenomenon is that the enlargement of scattering volume brings more background light caused by bremsstrahlung but no enhancement of laser power. Moreover, the power density of the cross-section of the laser beam varies with varying spot size, which should be measured so that it does not exceed the power threshold of any optical component existing in the optical path and cause damage. In addition to causing damage to the optical components, a high power density existing in a non-vacuum area may cause a spark, which consumes the energy carried by the beam and consequently reduces the signal-to-noise ratio.

To avoid the expansion of spot size during propagation, which damages the fragile inner crystal of optical components and reduces the signal-to-noise ratio of the scattered light signal, it is important to understand the spot size evolution of the laser beam during propagation. Using a beam profiler, the spot size at several positions after the beam leaves the laser head can be measured and the evolution of the spot size as the beam propagates in the optical path can be fitted based on equations (5.8) and (5.9). If the fitted spot size exceeds the entry diameter of any optical component existing in the optical path, we incorporate an image relay system into the optical path for relaying the image of the laser beam in multi-pass propagation to avoid damage caused by over-expansion of the spot size. The image relay system consists of a pair of lenses. The radius of curvature and spot size of the laser beam before and after passing through a thin lens can be expressed as:

$$\frac{1}{R'} = \frac{1}{R} - \frac{1}{f} \tag{5.10}$$

$$w' = w \tag{5.11}$$

Here, *R'* and *w'* are the radius of curvature and spot size of the beam after it passes through a thin lens, respectively. From equations (5.10) and (5.11), the w_0 and z_0 after the beam passes through a thin lens can be obtained by substituting *w'* and *R'* into equations (5.8) and (5.9).

The optical layout of the image relay system is shown in Fig. 5.9. To explain what happens when the light propagates from IP1 to IP2, ABCD matrix formalism is utilized. ABCD matrix formalism is a mathematical method used to analyze the behavior of optical systems. Based on ABCD matrix formalism, the transformation of a Gaussian beam as it propagates through an optical system can be compactly represented. Each optical element in the system is characterized by its own ABCD matrix, which represents its effect on the Gaussian beam. By multiplying the ABCD matrices of the individual components in the order of their arrangement, the overall ABCD matrix of the optical system can be obtained. This matrix can then be used to calculate the beam parameters at any position within the system, such as the beam waist size, position, and divergence.

Based on the propagation rule given in equations (5.8)–(5.11), if the laser beam is guided to pass through a pair of lenses with the same focal length and 2 times of focal length away from each other in sequence, the laser beam propagation, which ranges from the end from which the laser is emitted to the other end (after passing through the two lenses), can be expressed as

$$\begin{bmatrix} 1 & f-a \\ 0 & 1 \end{bmatrix} \begin{bmatrix} 1 & 0 \\ -\frac{1}{f} & 1 \end{bmatrix} \begin{bmatrix} 1 & 2f \\ 0 & 1 \end{bmatrix} \begin{bmatrix} 1 & 0 \\ -\frac{1}{f} & 1 \end{bmatrix} \begin{bmatrix} 1 & f-a \\ 0 & 1 \end{bmatrix} \begin{bmatrix} r_i \\ s_i \end{bmatrix} = \begin{bmatrix} -r_j \\ -s_j \end{bmatrix} \tag{5.12}$$

Here, subscripts *i* and *j* denote the two positions located outside a pair of lenses with the same focal length *f*; *a*, which is a non-negative value, is the distance between the position located at the laser emitting end and the lens that the laser passes through first; *f-a* is the distance

between the points corresponding to the end that the laser reaches after passing through both lenses and the 2nd lens that the laser has passed through; r is the transverse offset; and s is the offset angle. Furthermore, a pair of lenses is defined as an image relay system. IP1 and IP2 are defined as terminals of the image relay system. From equation (5.12), it can be indicated that the transverse offsets r and offset angles s have the same magnitude but inversed images at the two positions corresponding to the distance a and f-a. This implies that the beam quality is maintained at both terminals of the image relay system during the beam's propagation.

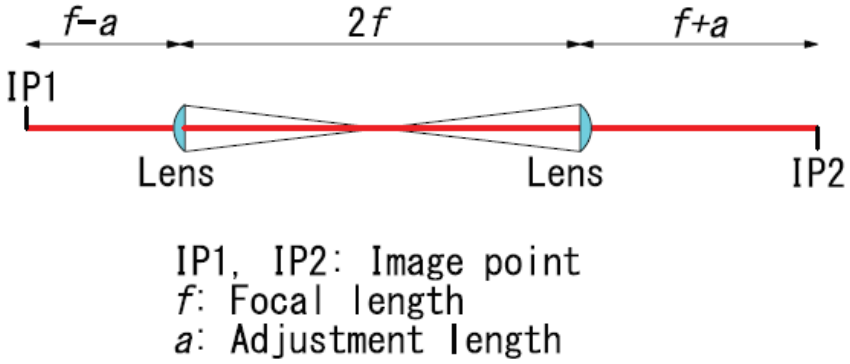

Fig. 5.9: Optical layout of the image relay system[16].

In addition, from spot size evolution, power density can be deduced by assuming the cross-section of a laser beam as a circle. The power density evolution can be another reference to judge whether the power density of a laser beam exceeds the power threshold of optical components given by the manufacturer. Specifically, to avoid the production of a spark caused by the high power density of the laser beam when it passes through the position near the focus of lenses, a vacuum pipe can be set to envelop the focus of two lenses of IRS in vacuum condition.

By measuring the spot size at several positions after the beam leaves the laser head, the evolution of spot size as the beam propagates

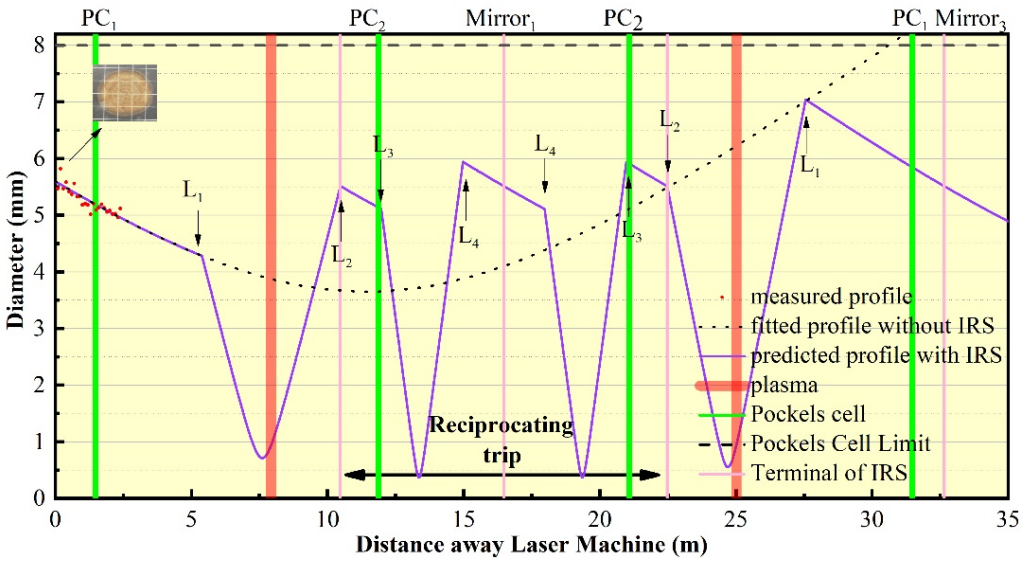

Fig. 5.10: The beam diameter evolution of the MPTS system with signal separation function.

in the optical path of our proposed system can be fitted using equation (5.8) as a hyperbolic curve. As shown in Fig. 5.10, the spot size is measured from the burn pattern. Based on the spot size measured at several positions after the laser beam leaves the laser machine, the spot size evolution deduced from equation (5.8) demonstrates that the gradually expanding spot size will exceed the acceptable threshold diameter (8 mm) for the beam to pass through a Pockels cell after the beam propagates 31 m away from laser output. Therefore, we set a pair of lenses, lenses 1 and 2, with the same focal length of 2.544 m on both sides of the plasma to maintain the laser spot size during the laser propagation between mirror 3 and lens 2 mentioned in Fig. 5.5. The layout of the image relay system is shown in Fig. 5.11. Here, lenses 1 and 2 are defined as the 1st image relay system. The foci of lenses 1 and 2 are located near the center of plasma to shrink the laser's spot size below 1.5 mm when the beam passes through plasma inside the vacuum vessel, which can avoid expansion of the spot size that increases the scattering volume, and maintain a good signal-to-noise ratio. Lenses 3 and 4 with the same focal length of 1.5 m are set in the optical path after the beam passes through plasma, between mirrors 1

and lens 2, to maintain the laser spot size during the laser's propagation there. Lenses 3 and 4 are defined as the 2nd image relay system. Here, one terminal of the 1st image relay system and one terminal of the 2nd IRS are both set to the position of lens 2. In this case, the spot size of the laser leaving lens 2 as a terminal of the 1st image relay system can be kept the same as that entering the 2nd image relay system. With the existence of two image relay systems, the spot size evolution shown in Fig. 5.10 as the purple solid line can be maintained within 6 mm in the optical path between mirror 1 and lens 2, and 7 mm in the optical path between mirror 3 and lens 2.

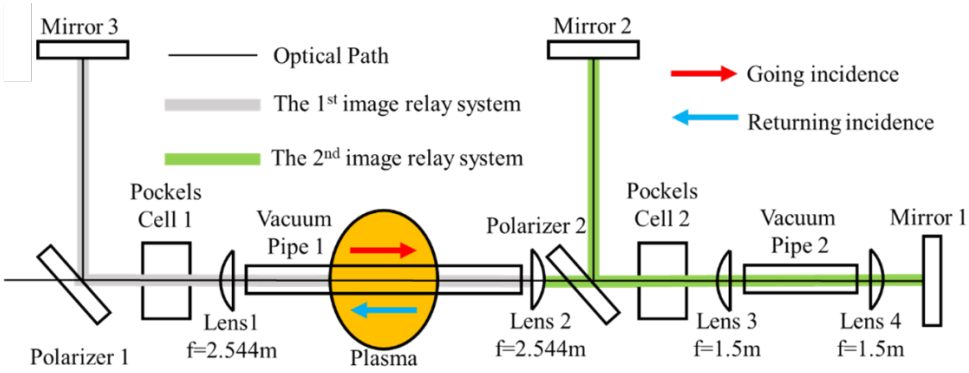

Fig. 5.11: Layout of the image relay systems, Pockels cells, vacuum pipes, and plasma.

Based on this fitted spot size evolution shown in Fig. 5.10, the power density evolution of the beam with 550 mJ per pulse was deduced by assuming the cross-section of the laser beam as a circle with evenly distributed power, as shown by the black dotted line in Fig. 5.12. It can be seen that due to the existence of two image relay systems, the power density reaches a very high value near the focus of the lenses, as shown by the solid purple line in Fig. 5.12. Therefore, vacuum pipe 2 is built to envelop the optical path where the power density of the laser beam exceeds 50×10^3 J/m^2 as one-third of the power threshold of windows installed on both sides of the vacuum pipe. In Fig. 5.12 the vacuum area of vacuum pipe 2 in our proposed system

is indicated by gray color and windows are indicated by vertical blue solid lines. The length of vacuum pipe 2 is 1.9 m.

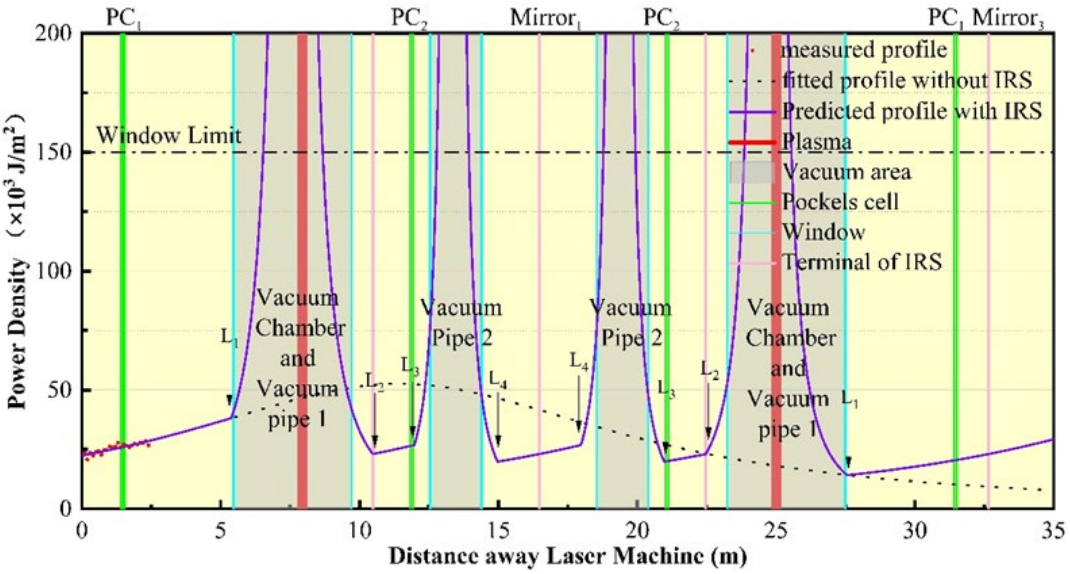

Fig. 5.12: The power density evolution of the MPTS system with signal separation function.

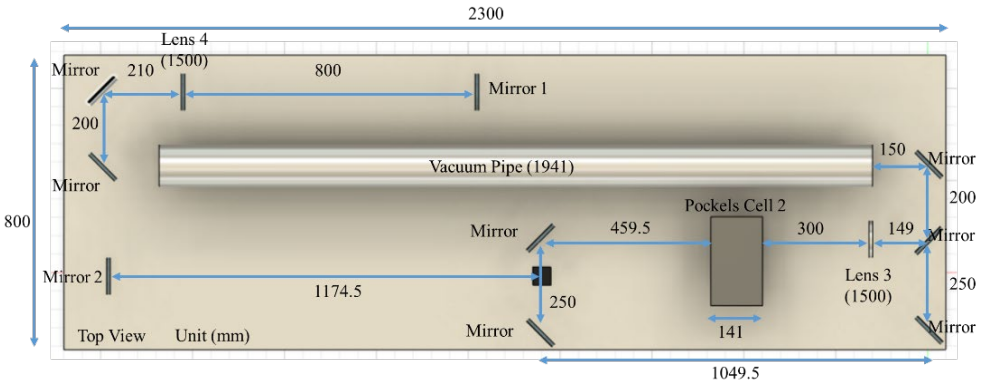

Fig. 5.13: The optical path of the 2nd image relay system located on the top of Heliotron J.

Based on the result of Gaussian beam analysis, the laser beam spot size is successfully maintained by the 1st image relay system during propagation of MPTS where the laser beam passes through plasma every time between mirror 3 and lens 2. During the propagation in the signal separation system, the spot size can be maintained by the 2nd image relay system in the optical path between mirror 1 and lens 2.

The reason behind the presence of two image relay systems in our optical path is that an extremely long distance is needed for the layout of the optical path and it is difficult to find lenses that can be used for image relay within dozens of meters. Contrastingly, the optical path where a high power density exists has been vacuumed to avoid the production of a potential spark.

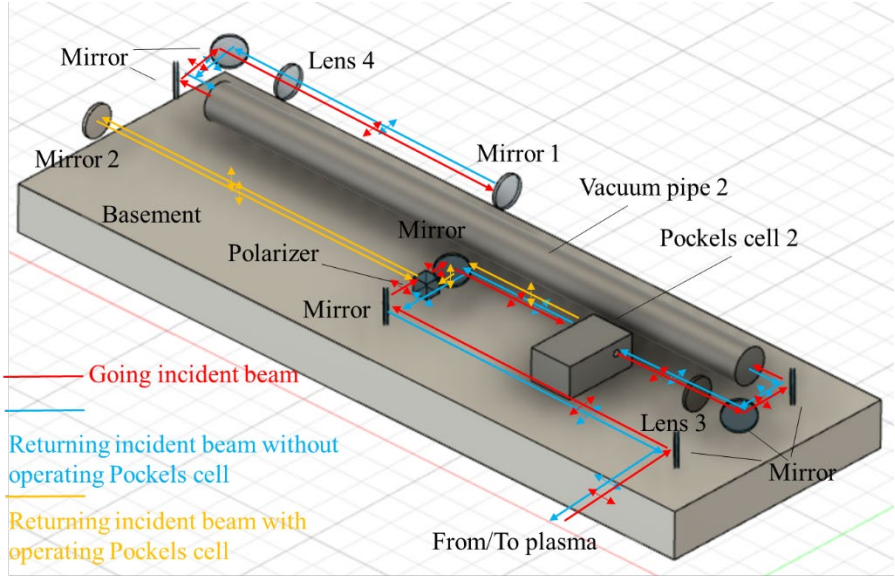

Fig. 5.14: The polarization status of laser beam in the optical path of the 2nd image relay system.

Based on the above simulations, the position of optical components, such as mirror, lens, Pockels cell, and isolator, can be determined, which are provided in Fig. 5.10 and Fig. 5.12. The results show that with the addition of the image relay system, the spot size and power density of the beam in the entire optical path will not exceed any threshold of the optical components. The optical path of the 2nd image relay system located on the top of Heliotron J is shown in Fig. 5.13. All of the optical components are set on an optical basement (2.3m × 0.8m). How the polarization status changes is shown in Fig. 5.15.

5.4 Spectroscopic system

The development of the spectroscopic system aims to improve the T_e measurement accuracy of the MPTS system on Heliotron J with a dual scattering angle. More specifically, the observation of anisotropic phenomena requires a high measurement accuracy to distinguish the difference between components corresponding to different directions in EVD. When applying interference filter polychromators to a TS system for the detection of scattered light, a combination of pass waveband of filter plays a key role in the measurement accuracy of a system because the pass waveband of filter sets in front of a channel determines the number of scattered light photons and background photons that can be detected as signal and noise, respectively. The number of scattered photons corresponding to a specific wavelength band is determined using the TS scattering spectrum as a function of scattering angle, T_e and EVD. Essentially, if the EVD obeys Maxwellian distribution, the optimization of the filter combination corresponding to minimum T_e measurement error on a specific range of T_e and n_e is determined primarily by the scattering angle of the system.

To investigate anisotropic phenomenon by MPTS system upgraded from TS system with scattering angle unequal to 90º, such as Heliotron J (approximately 160º), filter combinations should be optimized for both scattering angles simultaneously. The reason is that a new scattering angle will be produced after upgrading the MPTS system, as a supplementary angle of the previous scattering angle corresponding to the single-pass system. Because the scattering angle influences the profile of the scattered spectrum, some channels may detect different amounts of scattered photons corresponding to the new scattering angle. Consequently, this may result in a low signal-to-noise ratio if the background light keeps at the same level. Therefore, an optimization of filter combinations inside the polychromator is

necessary for reaching a high accuracy in T_e measurement corresponding to both scattering angles simultaneously.

Furthermore, the range of T_e is another preliminary parameter that should be determined prior to optimizing filter combinations. To understand edge transport physics, such as L-H transitions, the following is required. The high T_e measurement of plasma produced in Heliotron J (up to approximately 10 keV), prospected as maximum T_e in the core of Heliotron J plasma, requires passing waveband of filters as sparse as possible in a wide waveband. The low T_e measurement (as low as approximately 50 eV) requires passing waveband of filters as concentrated as possible near the original laser wavelength. Conversely, the plasma density in Heliotron J can be at rather low, densities of 0.5×10^{19} m^{-3} as the threshold line-averaged density of the H-mode in ECH and NBI operation[64] and at high densities greater than 10×10^{19} m^{-3} produced by combining a low toroidicity configuration with high-intensity gas-puff fueling. Therefore, the following three T_e ranges are regulated as optimizing parameters of filter combination for both scattering angles with n_e in the range of $0.5–10 \times 10^{19}$ m^{-3}. A low T_e range corresponding to values lower than 0.5 keV, a middle T_e range corresponding to 0.5–6 keV, and a high T_e range corresponding to 6–10 keV. The goal of filter optimization for both scattering angles is to find the filter combination that can provide the minimum value for the sum of the average T_e measurement errors corresponding to 2 scattering angles in these three T_e ranges and n_e region of $0.5–10 \times 10^{19}$ m^{-3}.

In the TS system applying an interference filter polychromator, the error of T_e measurement is relevant to scattered light, radiation from plasma, and noise brought by the detector and circuit. The scattered light signal is proportional to the detected photon number, which is a combination of the scattered photon number, the quantum efficiency of APD, and the total optical transmission of the entire system. How

the scattered photon number detected by channel *i* can be deduced has been described in Eq (4.3).

From the scattered photon number, T_e can be deduced by calculating the ratio between the intensity of the scattered light signal measured by two channels. The estimation of the variance from the mean values of the measured T_e can be made using approximate formulas:

$$Var(T_{eij}) = \left(\frac{\partial T_{eij}}{\partial N_i}\right)^2 \times (\delta N_{si})^2 + \left(\frac{\partial T_{eij}}{\partial N_j}\right)^2 \times (\delta N_{sj})^2 \quad (5.13)$$

$$Var(T_e) = \frac{1}{\sum_{i,j=1;i\neq j}^{i,j=5;i\neq j}\left(\frac{1}{Var(T_{eij})}\right)} \quad (5.14)$$

where $Var(T_{eij})$ is the variance of T_e deduced from the ratio between the scattered photon number detected by channels *i* and *j* ($i \neq j$); δN_{si} is the standard deviation of scattered photon number in channel *i;* and $\sum N_{si}$ is the sum of scattered photon number detected by all channels. Note that $Var(T_e)$ is the variance of T_e with consideration of the weight of each $Var(T_{eij})$.

The standard deviation of the measured number of photoelectrons in channel *i* can be expressed as the following equation as the standard deviation of photon number detected by APD follows Poisson distribution and the scattering signal is usually obtained by subtracting background signal from the total intensity;

$$\delta N_{si} = \sqrt{k \times \left(N_{S,i} + 2 \times N_{b,i}\right) + N_o} \quad (5.15)$$

where k is the APD excess noise factor; N_s is the scattered photon number; N_b is the number of photons produced by bremsstrahlung, and N_o is the contribution of detector and amplifier noise. Bremsstrahlung from background plasma is considered the major noise source. Spectral emissions such as D_α is not considered in this estimation. Factor 2 before $N_{b,i}$ is caused by the fact that both the signal and background channels contain the bremsstrahlung.

The total number of bremsstrahlung photons per unit frequency collected in a time Δt is as follows[40]:

$$N_b(\omega) = d\Delta L\Delta\Omega_s D \sin\theta\Delta t\left(\frac{Cn_e^2 Z_{eff}2\pi}{T_e^{\frac{1}{2}}h\omega}\right) \tag{5.16}$$

where D is the effective path length of the plasma; Δt, the pulse width; Z_{eff}, effective charge number and ω is angular frequency. The light collected by the collection optics from a region of dimension ΔL along the laser beam and d perpendicular to it is assumed as the source of the bremsstrahlung. The d is just the laser beam diameter when the beam passes through this region. The coefficient C is defined as

$$C = \left(\frac{e^2}{4\pi\epsilon_0}\right)^3 \frac{4}{3m_e^2c^3}\sqrt{\frac{2m_e}{3\pi}}\,\overline{g_{eff}} \tag{5.17}$$

where m_e is the electron mass; ϵ_0, the permittivity of free space, and $\overline{g_{eff}}$ is the Gaunt factor for the free-free radiation. In Eq. (5.16), $2\pi Cn_e^2 Z_{eff}/h\omega T_e^{1/2}$ represents the bremsstrahlung photon number per unit frequency from per unit volume into per unit solid angle. Therefore, by multiplying it by the collection volume, time, and solid angle, bremsstrahlung photon number can be obtained by Eq. (5.16). A channel i with the longest wavelength and shortest wavelength can be detected as λ_{sl} and λ_{ss} can detect the bremsstrahlung light within the range of $\epsilon_{iS} < \epsilon < \epsilon_{iL}$ as

$$N_{b,i} = d\Delta L\Delta\Omega_s D sin\,\theta\Delta t\frac{2\pi Cn_e^2 Z_{eff}}{T_e^{\frac{1}{2}}h}\int_{\epsilon_i}^{\epsilon_j}\frac{\eta(\epsilon)T(\epsilon)K(\epsilon)}{1+\epsilon}d\epsilon \tag{5.18}$$

Here, we introduce an enhancement factor $K(\epsilon)$, which represents the difference between the theoretical and measured bremsstrahlung intensities[65]. The appearance of $1+\epsilon$ is because Eq (5.16) is the bremsstrahlung photons number per unit frequency instead of per normalized wavelength. In actual cases, the contribution of

bremsstrahlung should be integrated along the line of sight. Therefore, Eq. (5.18) is replaced by the| following equation:

$$N_{b,i} = \frac{2}{D} \int dAL\Delta\Omega_s D sin\ \theta\Delta t \frac{2\pi C n_e^2(\rho) Z_{eff}}{T_e^{1/2}(\rho) h} \int_{\epsilon_i}^{\epsilon_j} \frac{\eta(\epsilon) T(\epsilon) K(\epsilon)}{1+\epsilon} d\epsilon dl$$

where l is the length along the line of sight, and ρ is the normalized plasma minor radius ρ. Since the contribution of the bremsstrahlung is mainly from the core plasma, the above equation can be approximated as[65,66]

$$N_{b,i} = 2dAL\Delta\Omega_s D\ sin\,\theta\Delta t \frac{2\pi C n_e^2(core) Z_{eff}}{T_e^{\frac{1}{2}}(core) h} \int_{\epsilon_i}^{\epsilon_j} \frac{\eta(\epsilon) T(\epsilon) K(\epsilon)}{1+\epsilon} d\epsilon \qquad (5.19)$$

The parameters included in Eqs (4.3), (5.13-15), and (5.19) that were used for the optimization of the filter combination are listed in Table 5.1. Only bremsstrahlung is considered as the radiation from plasma in this estimation. The remaining power percentage of the returning beam is approximated as 1 because this value is strongly determined by the quality of beam alignment. The overall transmission factor of the optical system, the spectral function of the collection optics, and the characteristic of spectral channel *i* are approximated as 0.1 in Eq (4.3) and Eq(5.19). The APD excess noise factor is proportional to APD gain and the ionization rate ratio between ionization rate of electrons and ionization ratio of holes. Excess noise factor *k* can be approximated as the following equation based on the McIntyre formula[67,68]:

$$k = 2 + iM \qquad (5.20)$$

Where *i* is ionization ratio and *M* is gain of the APD. Based on the McIntyre formula and the specification of HAMAMATSU (S8890 series), *M* is equal to about 100 at room temperature, and *k* is approximated as 2.5 in our calculation[69].

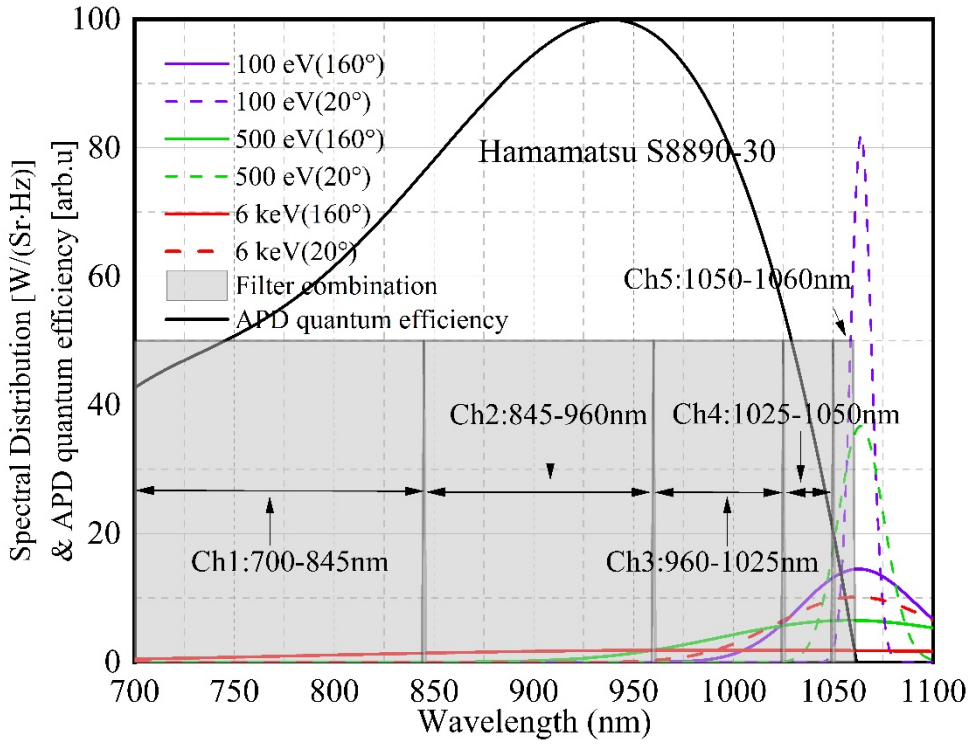

Fig. 5.15. Spectral distribution corresponding to two scattering patterns, quantum efficiency of APD, and previous filter combination.

Finally, optimization equations for calculating the number of scattered photons detected and the value of variance in each channel can be determined by setting the upper cut wavelength and lower cut wavelength of the pass waveband of each filter as variables. Filter combination producing the minimum T_e measurement error corresponding to the two scattering angles in the three T_e ranges can be obtained by applying the Newton-Raphson method, which can gradually approach the minimum value through successive iterations, that is, the solution of the equations. Our preliminary goal is to maintain the T_e measurement errors corresponding to both scattering angles lower than 10 % when T_e is higher than 100 eV and n_e is higher than 1×10^{19} m^{-3}. Additionally, the constrains of optimization equations are determined by Fig. 5.15, which shows the profile of quantum efficiency of APD. Furthermore, the distribution of current filter combination with 5 filters indicated by gray rectangles is shown in Fig. 5.15; it can be noticed that the lowest cut wavelength and

highest cut wavelength of pass waveband among current filter combination bounded on the blue and red side are at 700 nm and 1060 nm, respectively, which are to avoid the influence of radiation of Hα lines and low quantum efficiency of APD, respectively. Also shown in Fig. 5.15 are the scattered spectra at 100, 500, and 6000 eV corresponding to scattering angles (160º and 20º) of MPTS system on Heliotron J demonstrating the necessity of simultaneous filter optimization for both scattering angles. Scattered spectra show that the trend of blue shift corresponding to 160º is stronger as T_e rises, compared to that of 20º scattering. Under this circumstance, ch1 and ch2 of current 5 filters with pass waveband far away from the original laser wavelength keep on blind until T_e enhances to 6 keV. Meanwhile, the filter combination optimized only for 160º scattering may not be suitable for 20º scattering in the low T_e range due to the small blue shift of 20º scattering. The detected scattered photon number corresponding to the 160º and 20º scattering at a typical electron density in Heliotron J with $n_e \sim 2 \times 10^{19}$ m^{-3} are shown in Fig. 5.16. In the original filter combination, it can be seen that as T_e gradually rises, at least two channels can each detect 4000 photons when T_e is higher than 100 eV for 160º scattering. However, for 20º scattering, the same detected photon number can be obtained until ~500eV, which means in low T_e measurement, the reliability of the 20º scattering measurement is not satisfied. Moreover, no TS scattered photons can be detected in the two channels with the shortest pass wavebands, which confirms that they are keeping blind during the whole T_e measurement range. Based on these considerations, the accuracy of T_e measurement by applying 20º scattering should be verified.

The performance of T_e measurement corresponding to 2 scattering angles as a function of T_e from 10 eV to 10 keV and n_e from 0.5×10^{19} m^{-3} to 10×10^{19} m^{-3} are given in Fig. 5.17. The T_e measurement errors corresponding to 160º and 20º scattering angles estimated by current 5-filter combination (i.e., ch1: 700–845 nm; ch2: 845–960 nm; ch3:

960–1025 nm; ch4: 1025–1050 nm; and ch5: 1050–1060 nm) are plotted in Fig. 5.17 (a). Because the current 5-filter combination is initially optimized only for 160º scattering, T_e measurement error corresponding to 20º scattering performs poorly in the low T_e range with an error higher than 10 % when T_e is below 100 eV. To reduce T_e measurement error corresponding to 20º scattering in low T_e and n_e regions, a 5-filter combination optimized for both scattering angles simultaneously is made (ch1: 702–947 nm; ch2: 952–1020 nm; ch3: 1020–1043 nm; ch4: 1043–1055 nm; ch5: 1055–1060 nm). Its performance is shown in Fig. 5.17 (b). It successfully reduces the T_e measurement error corresponding to the 20º scattering angle to lower than 10 % when T_e is lower than 100 eV and n_e is higher than 1×10^{19} m^{-3}. Conversely, the T_e measurement error corresponding to 160º scattering becomes double for the high T_e region because more filters with pass waveband are distributed near the Nd:YAG laser wavelength in order to improve T_e measurement accuracy corresponding to 20º scattering with weaker blue shift. Therefore, to maintain a high T_e measurement accuracy corresponding to 160º scattering and reduce the measurement error corresponding to 20º scattering in low density and T_e region, a 6-filter combination optimized for both scattering angles simultaneously is made by introducing one more filter. As shown in Fig. 5.17 (c), the T_e measurement error estimated by the 6-filter combination optimized for both scattering angles reduces the error corresponding to 20º scattering at low T_e range to at least one-half as compared to that of the 5-filter combination; additionally, it maintains the accuracy level as compared to the 5-filter combination optimized only for 160º scattering in high T_e range. The specification of the 6-filter combination optimized for both scattering angles is given below:

(1) channel 1: 700–845 nm;

(2) channel 2: 845–950 nm;

(3) channel 3: 950–1020 nm;

(4) channel 4: 1020–1043 nm;
(5) channel 5: 1043–1056 nm;
(6) channel 6: 1056–1061 nm;

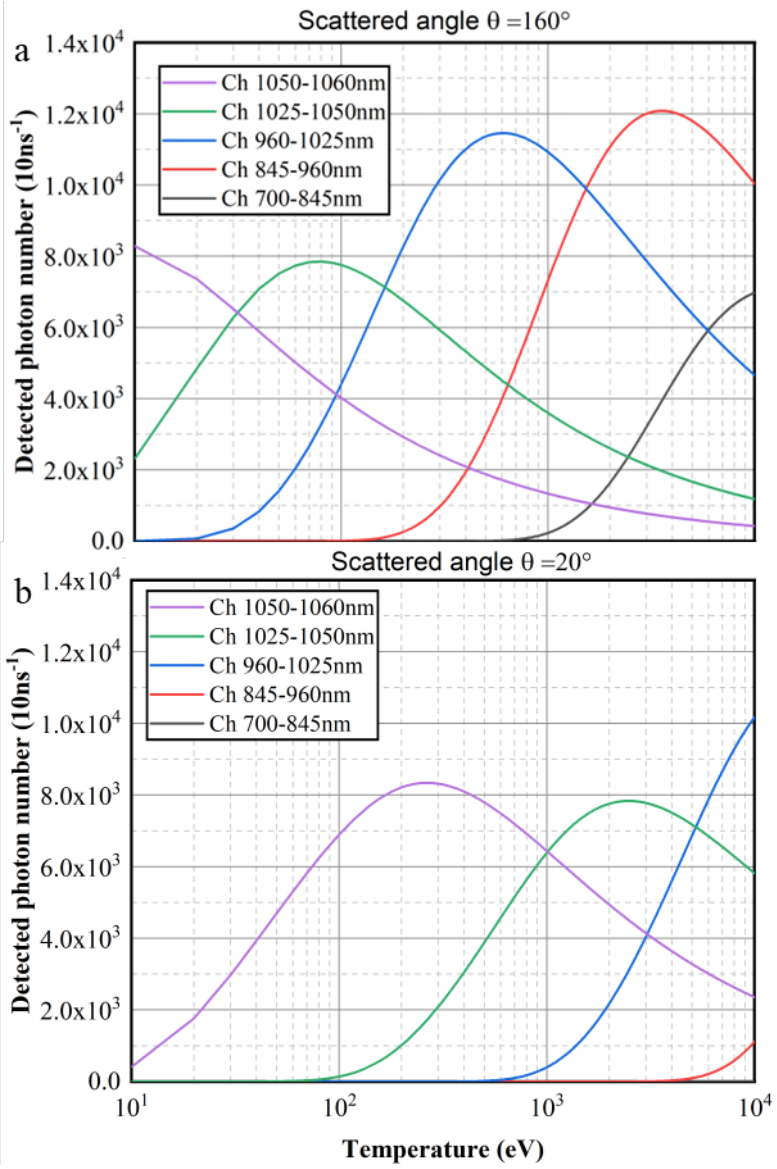

Fig. 5.16. Estimation of scattered photons for each pass waveband as a function of Te in a) 160º scattering and b) 20º scattering.

The performance of 160º scattering is better than that of 20º scattering in almost the entire temperature and electron density range. This is because the spectral width is longer and the spectrum in most T_e and n_e regions correspond to a higher quantum efficiency of the APD so that more scattered photons can be detected. Conversely,

errors of T_e corresponding to both scattering angles have a downward trend as n_e increases because more scattered photons are produced in the scattered volume, which corresponds to a higher signal-to-noise ratio. T_e measurement error obtained for both scattering angles using this new 6-filter combination can be reduced to lower than 10 % after the T_e reaches 60 eV and n_e reaches 1×10^{19} m^{-3}, which can provide acceptable reliability for anisotropic temperature observation.

TABLE 5.1. Heliotron J MPTS system parameters.

System parameter	Value
T_e	50 eV–10 keV
n_e	0.5–10 × 10^{19} m^{-3}
Scattering volume length (L)	~ 1 cm
Scattering angle (θ)	160º/20º
Solid angle (Ω_s)	80–100
Plasma diameter	~ 0.24 m
Laser power	~ 500 mJ/pulse
Pulse width	10 ns
Remaining power percentage	100 %
Production of overall transmission factor of the optical system, spectral function of the collection optics and characteristic of a spectral channel	0.1
APD excess noise factor (k)	2.5

Besides, it should be noted that strong line radiation has not been considered in this optimization due to the absence of a diagnostic method on the waveband from 700 nm to 1064 nm. Later, if additional strong lines get detected, they will have to be blocked out using rejection filters and their impact on the characteristic of the spectral channel and the filter combination should be re-considered.

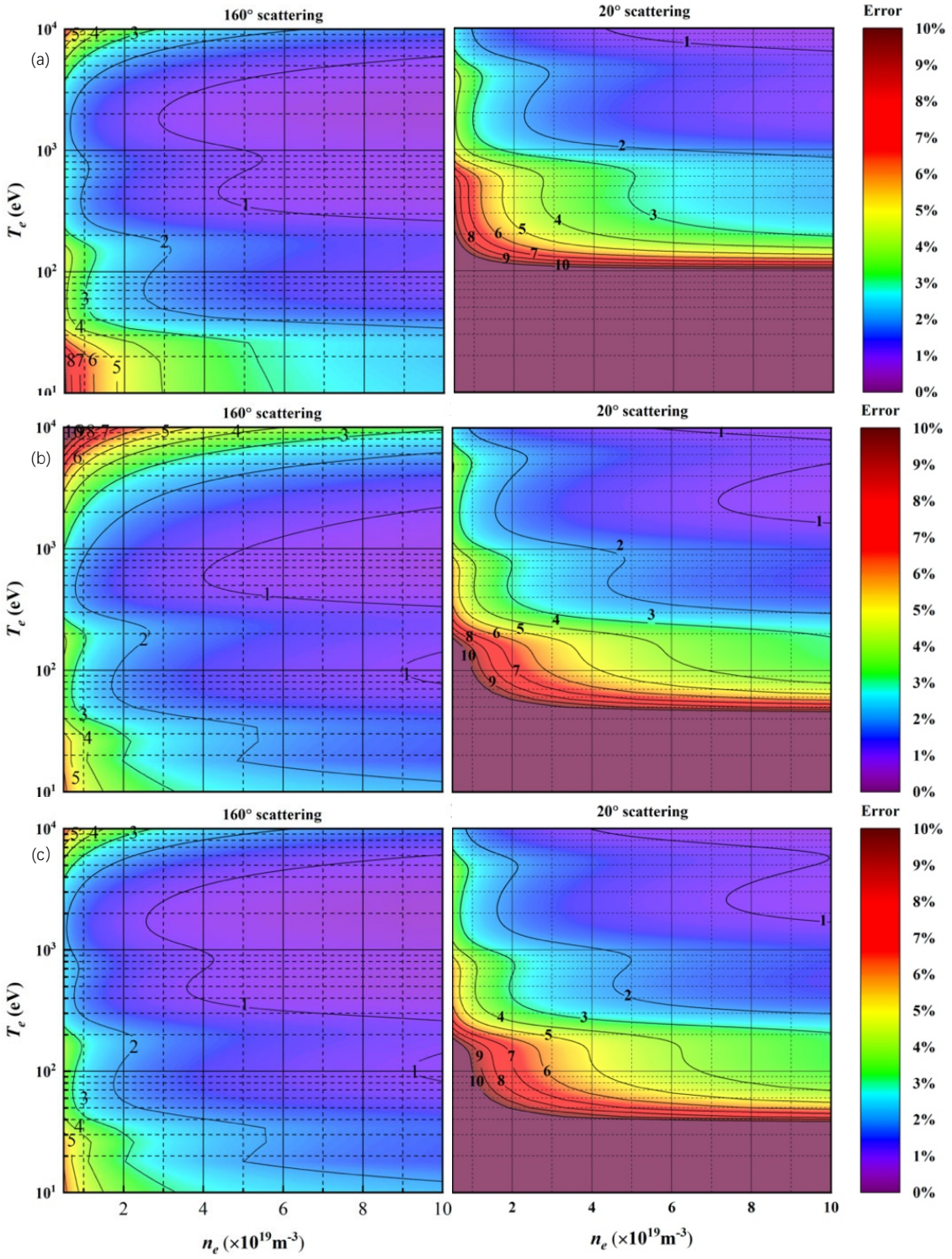

Fig. 5.17. Estimated errors of Te measurement corresponding to 160º and 20º scattering, respectively, as a function of Te and ne by utilizing a) current 5 filters optimized for 160º scattering, b) New 5 filter combination optimized for both 160º and 20º scattering, and c) New 6 filter combination optimized for both 160º and 20º scattering.

5.5 Summary

A design of dual scattering angles MPTS with signal separation function is proposed in this section. Compared to simply extending the length of the optical path, the layout of the optical path for TS on Heliotron J can be significantly optimized using the proposed system by reaching a 120 ns signal separation or longer than the performance of our current system, which realizes a compact system configuration. With the operation of the trigger system, two Pockels cells can be triggered so that the polarization status of the laser beam in the optical path can be changed for multi-pass or anisotropy measurement. To the design of the optical path, As the length of the optical path of such a system is significantly increased, two IRSs are designed to constrain the expansion of the laser spot size within 7 mm during beam propagation and they successfully prevent any damage to the Pockels cell crystal from being caused. Based on the evolution of spot size, the evolution of power density is simulated and the areas where high power density exists are vacuumed to avoid laser-induced breakdown.

The filter combination is optimized for both scattering angles existing in the MPTS on Heliotron J simultaneously. By applying a 6-filter combination, the T_e measurement error in the newly added 20º scattering angle by upgrading to MPTS is reduced to at least one-half of the error estimated by applying the current 5-filter combination when T_e is lower than 100 eV.

In general, it can be said that based on this design, overlapping signals can be separated by using the signal separation function with a compact optical path layout. Additionally, the accuracy of the MPTS system will become more reliable for both scattering angles, which provides more reliability for the investigation of the anisotropic phenomenon.

Chapter 6
Experimental Results

6.1 Overview

To confirm the effect of the signal separation system and the enhancement of signal intensity, in this chapter, system performance is tested by the Raman scattering signals, which is given in section 6.2 to demonstrate the extended incident interval between two adjacent incidences and the increased signal intensity. In section 6.3, an anisotropy T_e measurement was done in an ECH plasma. The signal process method is discussed and the preliminary result is provided.

6.2 System performance

6.2.1 Theory of Raman scattering

When light interacts with atoms or molecules, most of the scattered photons have the same frequency as the incident light, which is known as Rayleigh scattering. Besides, there are also scattered photons with frequencies higher or lower than the incident light due to changes in the vibrational or rotational energy states of the molecules. This phenomenon is called Raman scattering. Raman scattering occurs at specific wavelengths around the wavelength of the incident light λ_i and can occur in two forms: Stokes and anti-Stokes scattering. The specific form depends on the changes in the vibrational and rotational states of the scattering molecule. In Stokes scattering, if the molecule absorbs energy, it emits a photon of lower energy or frequency than the incident photon, resulting in a shift towards the red side of the incident spectrum. In anti-Stokes scattering, the molecule loses energy,

causing the incident photons to shift towards the blue side of the spectrum. One significant advantage of Raman scattering over Rayleigh scattering, particularly in Thomson scattering applications, is that the scattered light does not occur at the same wavelength as the laser used. This eliminates the issue of contamination of the signals with stray laser light, enhancing the accuracy of the measurements.

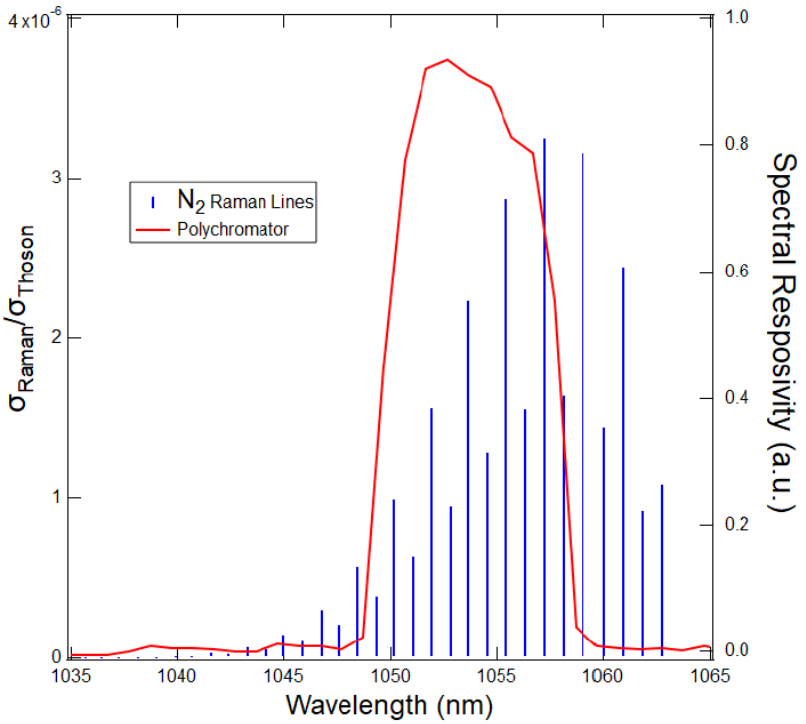

Fig. 6.1: Normalised Raman spectrum showing anti-stokes lines from a nitrogen filled vessel at ~300 K.

To calibrate the MPTS system for Raman scattering, a calibration procedure is performed using a N_2-filled vessel at a known gas pressure and temperature. Typically, the calibration covers a range of 0-400 Torr with a step size of 100 Torr at room temperature. Based on these parameters, the expected wavelengths and spectral intensities of the anti-Stokes lines can be determined and are depicted in Figure 6.1. Consequently, the total signal within a specific spectral channel is obtained by summing all significant Raman contributions within that

channel. Hence, the signal level resulting from a Raman scattering event, measured in volts, can be expressed as follows:

$$V_R = (GT(\lambda_L)\Delta\Omega L)\left(\frac{1}{\frac{hc}{\lambda_i}} r_e^2 \sum_j \eta_j(\lambda_s) T_j(\lambda_s) \frac{S_{\mathrm{R}}}{\lambda_i}\right) E_{laser} \frac{P_{gas}}{k_B T_{gas}} \quad (6.1)$$

where S_R is the spectrum of Raman scattering. The number of N_2 molecules is given by $n_{gas} = \frac{P_{gas}}{k_B T_{gas}}$. Therefore, for a given gas pressure and temperature the system constants can be evaluated.

6.2.2 Signal separation function

To evaluate the performance of the signal separation system, the extended incident interval mentioned expressed by Eq (5.7) needs to be confirmed. The incident interval can be verified by both TS signal and Raman scattering signal. However, the background light caused by bremsstrahlung and strong line radiation during Thomson scattering may disrupt the TS signal and even overwhelm it, especially in low-density conditions. Therefore, nitrogen Raman gas scattering experiments were carried out to evaluate the performance of the signal separation system on extending incident interval to avoid the disruption of background light.

Fig. 6.2 shows Raman scattering signals corresponding to one going incidence and its successive returning incidence, to demonstrate an increased incident interval between these two incidences by operating the signal separation system. $T_{going\ incidence}$ and $T_{returning\ incidence}$ are appearance timing of scattered light signal corresponding to a going incidence and its successive returning incidence respectively. The value of $T_{going\ incidence}$ minus $T_{returning\ incidence}$ is incident interval, as the interval between a going incidence and its successive returning incidence, which is highlighted by orange vertical lines. Fig. 6.2 (a) shows the Raman scattered light signal obtained by our multi-pass TS system before building the signal separation system. A complete

overlapping of the signal of going incidence and returning incidence exists there with a very short incident interval equal to 22 ns, which means only the

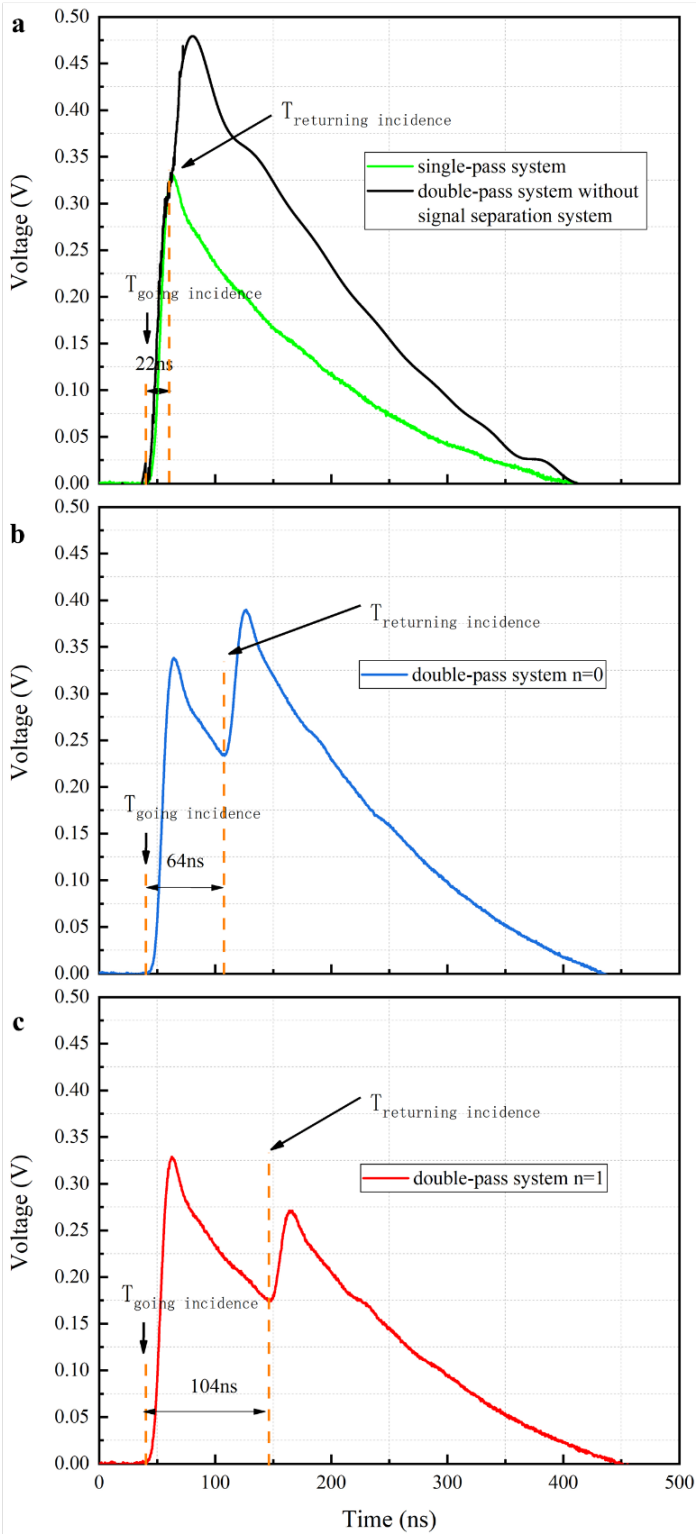

FIG. 6.2 (a) Raman scattering signals observed in CH. 1050-1060 nm by multi-pass TS system without signal separation system. (b) measured by multi-pass TS system with signal separation system when n is equal to 0. (c) measured by multi-pass TS system with signal separation system when n is equal to 1.

signal corresponding to going incidence during this 22 ns is non-overlapped with the signal corresponding to the successive returning incidence. A scattered light signal plotted by a green solid line corresponds to a single-pass mode of the MPTS system where no returning incidence occurs. Fig. 6.2 (b) and (c) show the scattered light waveform with the existence of a signal separation system where the beam reciprocates in the optical path of the signal separation system 0 times (n=0) and once (n=1) respectively. The Raman scattered light signal corresponding to returning incidence starts to appear after the appearance of the signal corresponding to going incidence with the incident interval equal to 64 ns (n=0) and 104 ns (n=1) respectively. As shown in Fig. 6.2 (b) and (c), incident interval extended by operating signal separation system shows a good coincidence with the value calculated from Eq (5.7) that the time consumed in one round trip between mirror 1 and 2 is 40 ns.

Consequently, the Raman signal verifies the signal separation system can significantly separate scattered light signals corresponding to a going incidence and its following returning incidence. The scattered light signal corresponding to the going incidence is no more overlapping with that corresponding to the returning incidence from $T_{going\ incidence}$ to the timing equal to $T_{going\ incidence}$ plus incident interval shown in Fig. 6.2 (b) and (c).

6.2.3 Improvement of signal intensity

To perform the multi-pass experiment on T_e measurement, the enhancement of the signal intensity corresponding to the multi-pass number needs to be evaluated. Raman scattering is also chosen here

because of the merits mentioned in the last section. The Raman scattering signals at room temperature measured in February 2021 are shown in Fig. 6.3. The single-pass (black solid line) and multi-pass signals (red and blue solid lines) of channel 1050-1060nm shown are measured by a Yoshikawa oscilloscope. It can be clearly distinguished the four-pass scattering signals in the MPTS system. In the MPTS system, the scattered signals from the first through fourth laser passes are added. The pass number is corresponding to the *N* mentioned in Eq (5.7). The signal separation system is not in operation in this experiment, which means *n* is 0. The integrated scattering intensity of the multi-pass is shown in Fig. 6.4, which is about 2.5 times larger than that of the single-pass.

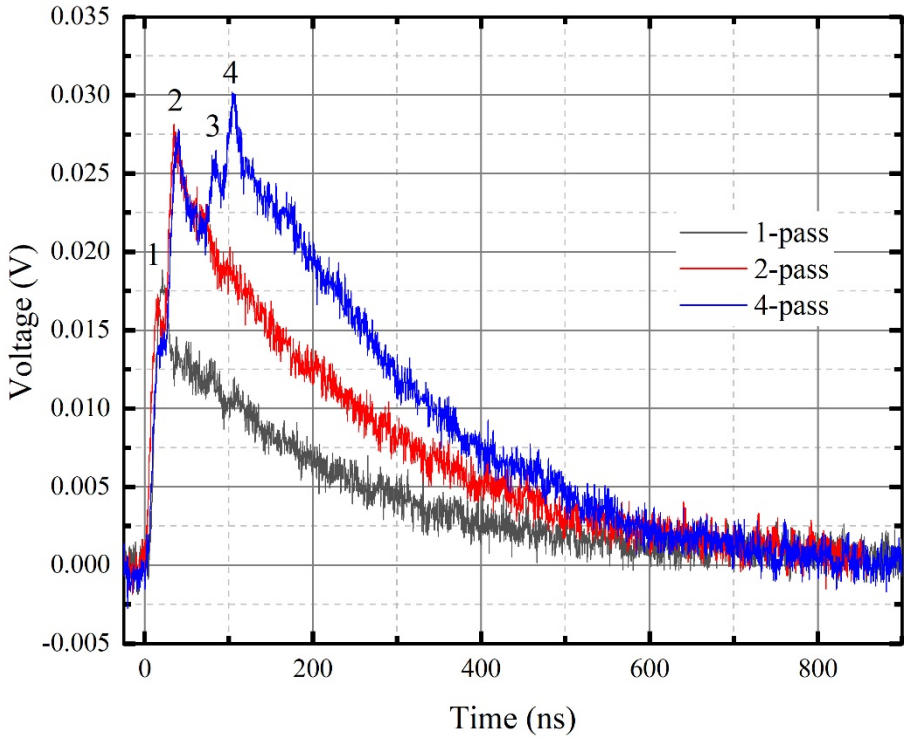

Fig. 6.3: Raman scattering signals observed in CH. 1050-1060 nm by MPTS system without operation of the signal separation system.

Another stray light was recorded in November 2020 that a 18-pass signal could be distinguished, which is shown in Fig. 6.5. This result also has good agreement with our theoretical calculated value that 66

ns is consumed in a round trip of the optical path of the 1st image relay system (f_{L1}=f_{L2}=2.544m). The light alignment of the polarization optical system and the trigger timing of the trigger system are important to the pass number realized finally. Moreover, the more pass number is, the higher intensity of scattered light can be detected. Therefore, a good light alignment and right trigger timing are critical to the MPTS system.

6.3 Anisotropy Te measurement

6.3.1 Signal process

To deduce the T_e measured by the going and the returning incidences respectively, it's necessary to analyze the value of the integration of the whole waveform corresponding to each incidence because it can reflect the intensity of the scattered light power related to the incidence. After operating the signal separation system, part of the going incidence scattered light signal is still overlapping with the returning incidence scattered light signal. Therefore, to calculate the integration of the whole waveform corresponding to the going incidence and the returning incidence respectively, a fitting method is used to construct the waveform of the going incidence that is still overlapping with the successive waveform corresponding to the returning incidence. By fitting the whole Thomson scattered light waveform corresponding to a going incidence based on the Thomson scattered light waveform separated by the signal separation system, the integration of the whole Thomson scattered light waveform of the going incidence can be evaluated. Further, the integration of the Thomson scattered light waveform corresponding to the successive returning incidence can be deduced by using the integration corresponding to the whole Thomson scattered light waveform

including both going and returning incidence minus the evaluated integration corresponding to the going incidence.

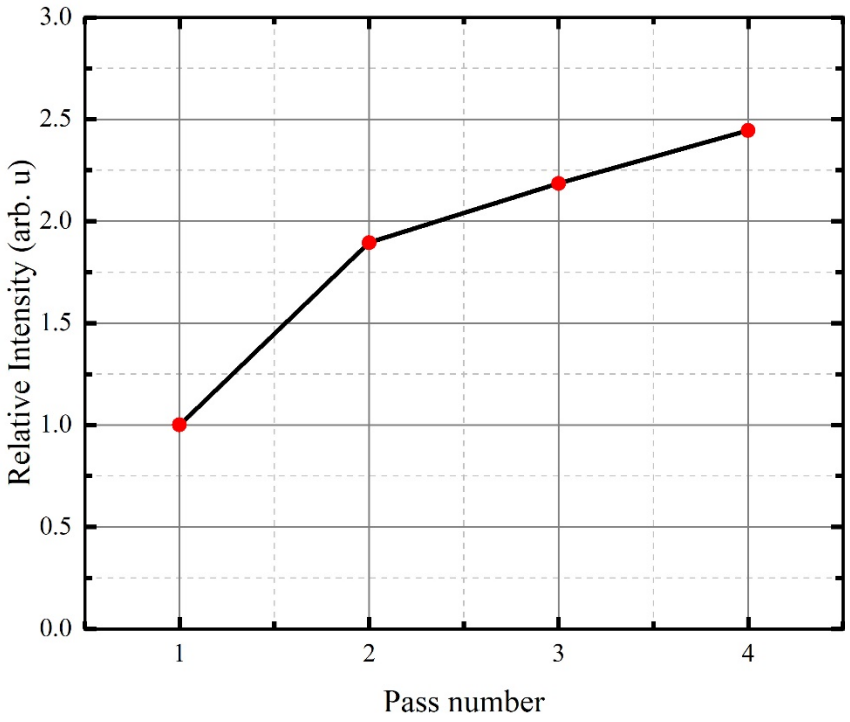

Fig. 6.4: Enhanced intensity of the MPTS Raman scattering signals.

Fig. 6.6 shows how a raw Thomson scattered light signal corresponding to a going incidence is fitted. The orange dotted line is the average waveform of 4 sets of waveforms measured at intervals of 20 ms before plasma is produced. It's used to analyze the offset of the waveform and the influence of the stray light. 0 s is the time when the laser is produced. The average of the waveform from $-1\times10^{-7}\sim 0$ s is used to determine the offset. On the other hand, the integration of the waveform from $0 \sim 5\times10^{-7}$ s with offset removed is used to evaluate the integration of stray light. It can be seen that there's no obvious fluctuation after 0s, which is because the responsivity of the filter in front of each channel inside the polychromator is around 10^5 times that of light with a wavelength near 1064 nm. As a result, stray light can be significantly mitigated. The Black solid line is the raw Thomson scattered light signal of one measurement after plasma is produced.

The influence of background light can be evaluated by the integration of the raw scattered light waveform from -1×10^{-7} ~ 0 s with offset removed. $T_{appearing}$ and T_{peak} are the time when the going incident signal appears and its peak appears respectively. The red dashed line is its fitted scattered light waveform based on the waveform from the timing that the going incident signal appears to the timing that the returning incident signal appears. Here the waveform corresponding to the going incidence from the peak value of the waveform is fitted as an exponential function described by Eq (4.7). The fitted equation of waveform from the peak of the going incident waveform is expressed as:

$$S_f(t) = a \cdot exp\left(\frac{t - T_{peak}}{\tau}\right) \tag{6.2}$$

where a is the magnitude of the signal, T_{peak} is the timing corresponding to the peak value. τ is the time constant of the signal.

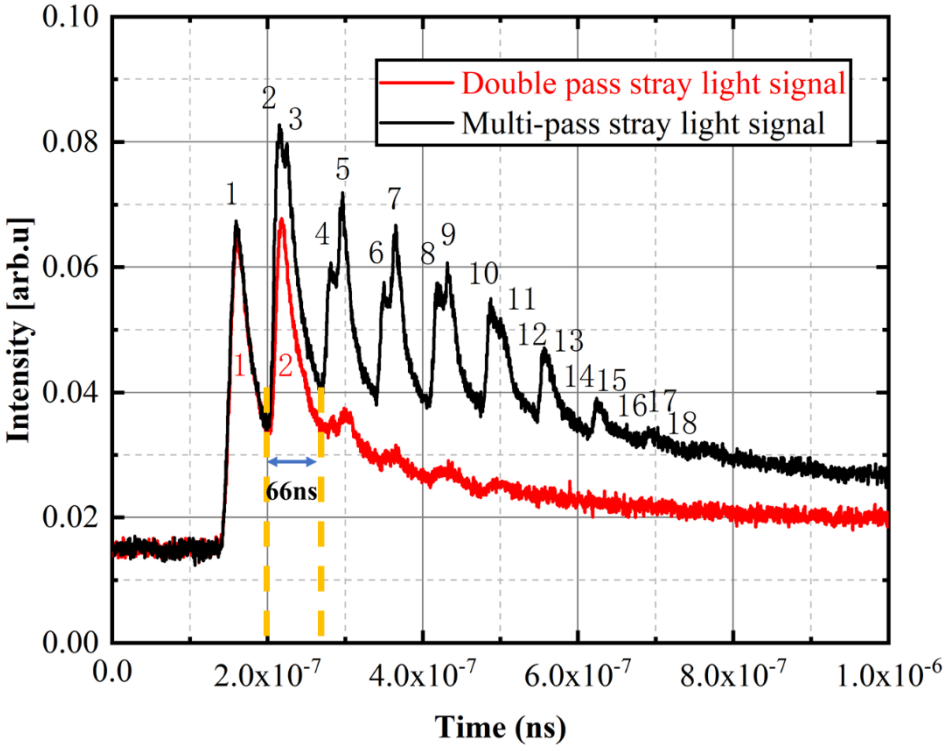

Fig. 6.5: Stray light signals observed by an APD(November 2020).

The waveform provided for calculating the parameters a, $T_{peak,}$ and τ in Eq (6.2) is the section of the waveform from T_{peak} to $T_{fit\ ending}$. $T_{fit\ ending}$ is the appearance timing of the returning incidence signal, which can be determined by the sum of the appearance timing of the going incident scattered light signal $T_{appearing}$ and the incident interval shown in Fig. 6.2.

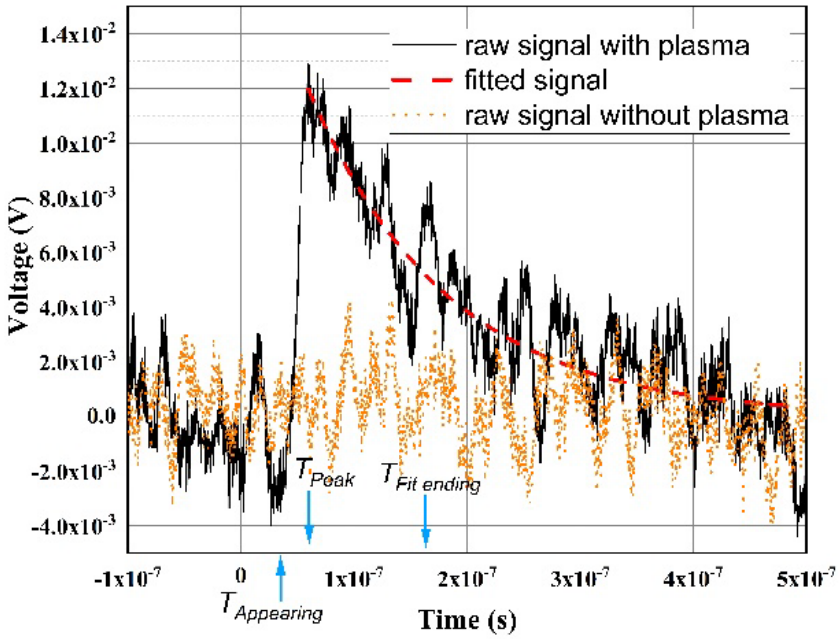

Fig. 6.6: Raw and fitted Thomson scattered light signal measured by a single pass mode (only going incidence occured).

The average fitting error of a whole going incidence signal based on waveform separated by different incident intervals is provided in Fig. 6.7 where 500 single-pass TS scattering signal waveforms with different peak values chosen from our previous experiment are analyzed. Fig. 6.7 shows the error of integrated value of whole scattered light signal corresponding to going incidence obtained by fitting scattered light signal based on separated waveform of going incidence compared with an integrated value of raw signal corresponding to going incidence. The fitting error can be expressed as

$$Error = \frac{\int S_r dt - \int S_f(t) dt}{\int S_r dt} \tag{6.3}$$

where S_r and S_f are raw and fitted scattered light waveform corresponding to going incidence from peak value. $S_f(t)$ is the waveform fitted as eq (6.2) based on separated signal waveform corresponding to the period from T_{peak} to $T_{fit\ ending}$. The incident interval as the difference between $T_{appearing}$ and $T_{fit\ ending}$ are 22ns, 64ns and 104ns respectively, corresponding to the verified incident interval shown in Fig. 6.2 (a-c).

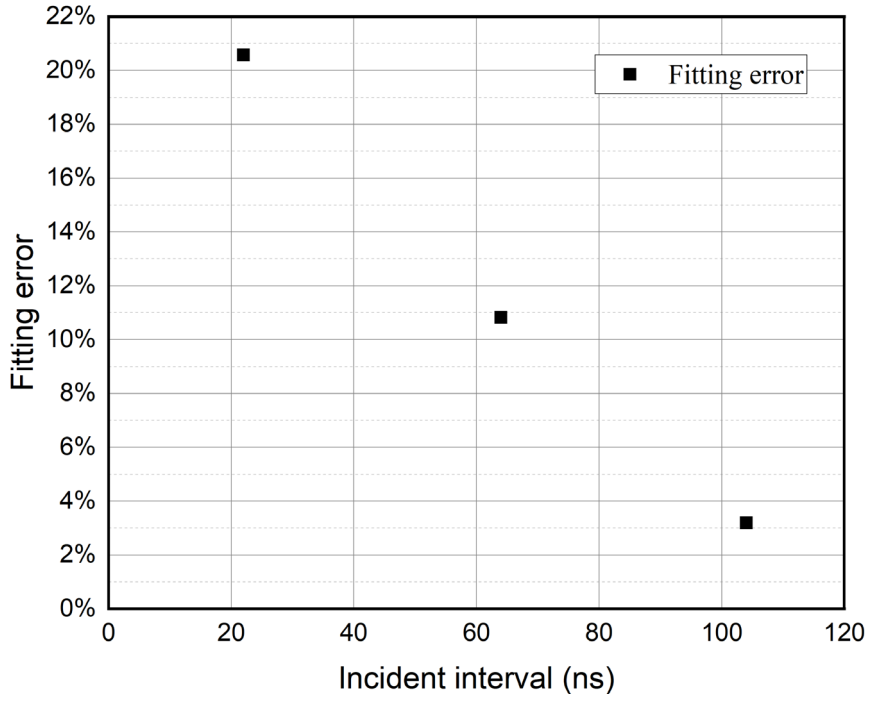

Fig. 6.7: Fitting error of integrated value of scattered light signal corresponding to different incident intervals.

It can be seen that the fitting error corresponding to an incident interval equal to 22 ns has a very large value. The reason is that influence of multiplication gain due to the avalanche effect at initial irradiation. When the incident interval is extended to 64 ns, the fitting error can be significantly reduced below 11%. When an incident interval is further extended to 104 ns, the fitting error goes down below 4%. These results prove that fitting error can be reduced by increasing

incident interval. Further, by minus the integrated value corresponding to going incidence based on fitting from the integrated value of the whole signal including both going incidence and returning incidences, the integrated value of scattered light signal corresponding to returning incidence can be obtained. As a result, T_e corresponding to two incidences can be deduced by constructing their spectrums.

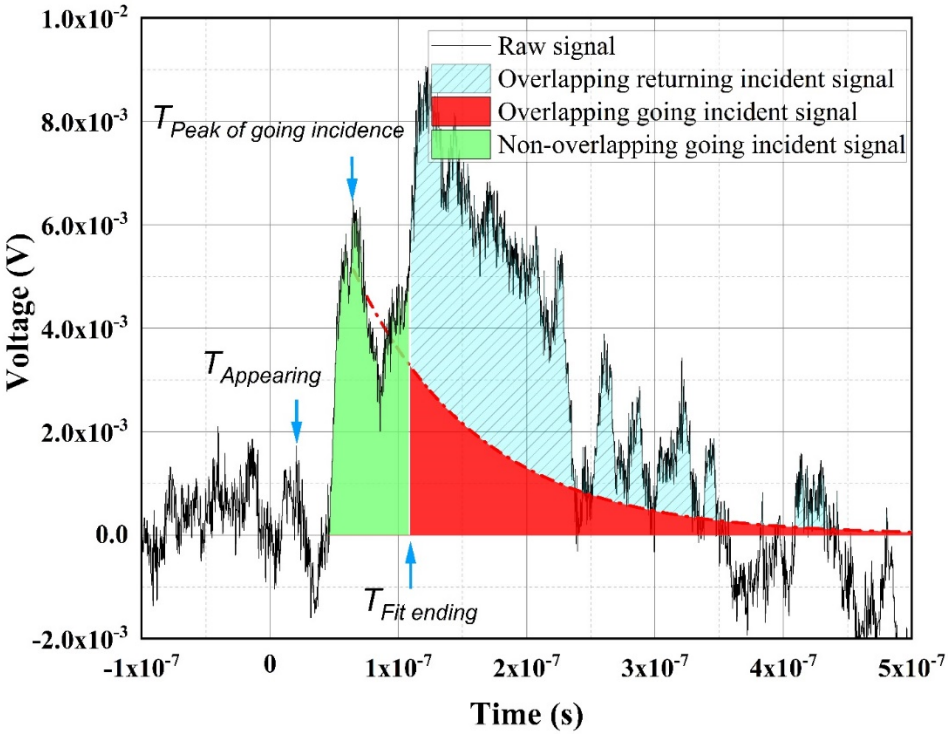

Fig. 6.8: Fitting error of integrated value of scattered light signal corresponding to different incident intervals.

The double-pass TS signal is shown in Fig. 6.8. The areas plotted by different colors correspond to the TS signal caused by a going or returning incidence. The intensity of TS signal caused by the going incidence includes the areas plotted by green that has been separated and the red that has been fitted. The intensity of TS signal caused by a returning incidence can be deduced by using the whole signal waveform integration minus the The intensity of TS signal caused by the going incidence. As mentioned above, the longer the incident

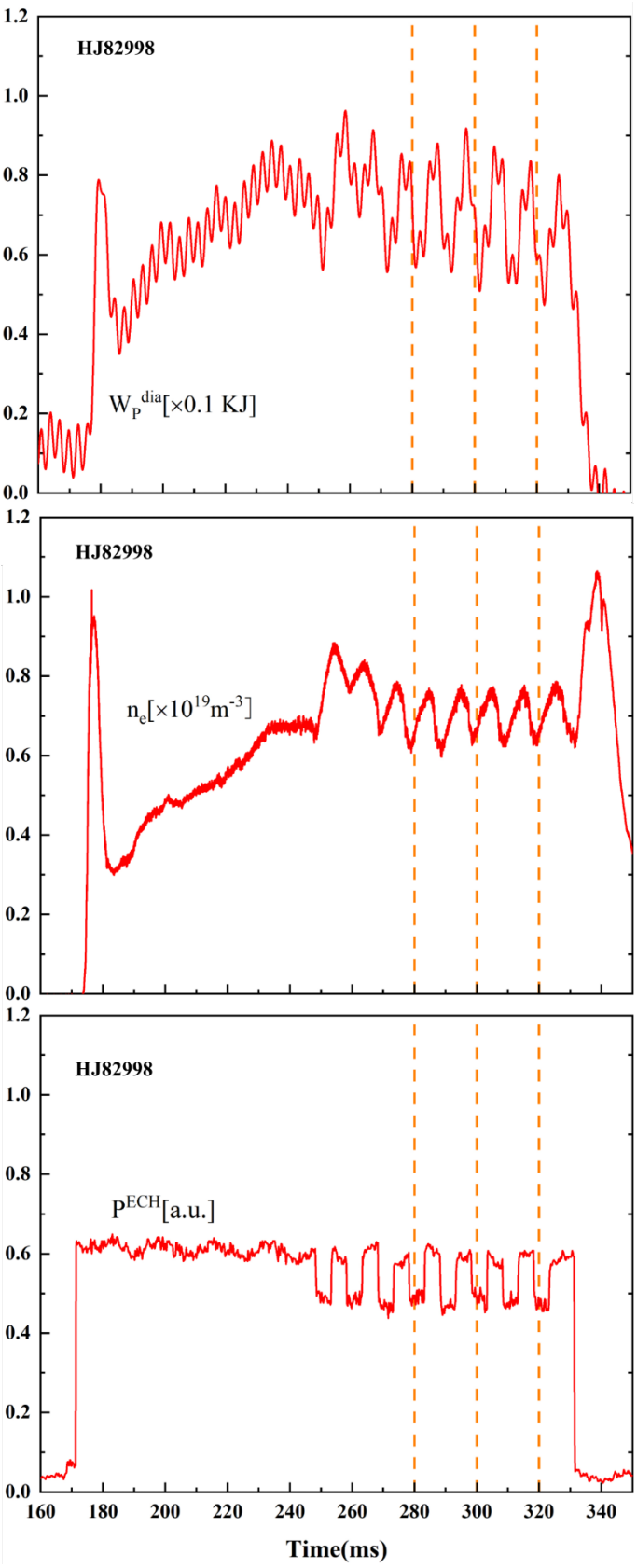

Fig. 6.9: Time traces of line-averaged density, stored energy in the plasma, and power evolution of ECH.

interval is, the more separated waveform we can get, which brings about a higher reliability of the intensity value.

6.3.2 ECH plasma experiment

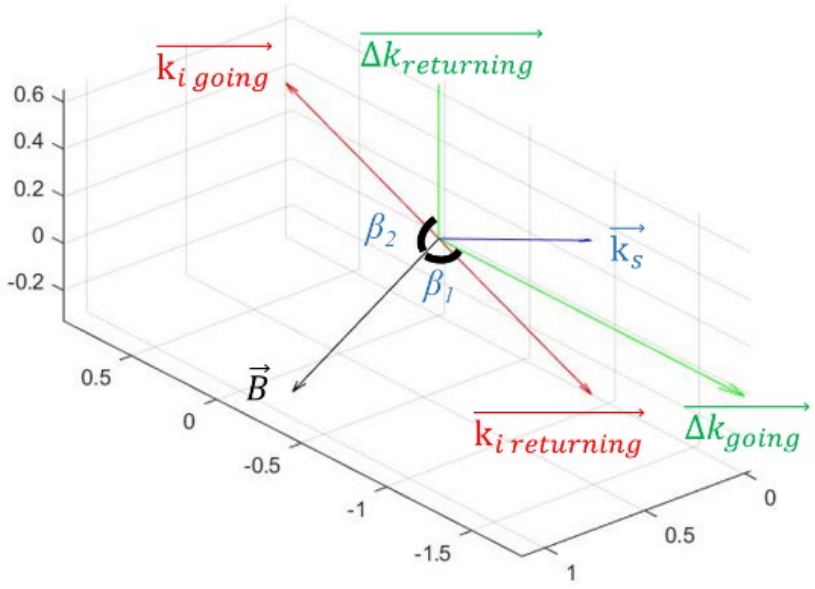

Fig. 6.10: Information of local magnetic field and scattering configurations corresponding to 160º and 20º scattering.

An anisotropy T_e measurement was done in a plasma generated by ECH. Fig. 5 shows the time evolution of the line-averaged density n_e, ECH power, and the stored energy W_p in the ECH plasma. The plasma is initiated by ECH ($N_{\|} = 0.38$) from 170 ms and maintained only by electron cyclotron heating until 330 ms. The power of ECH is about 247 kW. The power of ECH fluctuates from 250 ms to 330 ms since it's under modulation. Because the line-averaged density n_e is quite low, three shots (shot.82995, 82996, and 82998) with good plasma reproducibility are averaged as a fixed experiment.

The relationship between the scattering plane and the local magnetic field is shown in Fig. 6.10. Measured position is at the core plasma (r/a~0.26). $\Delta\overrightarrow{k_{going}}$ and $\Delta\overrightarrow{k_{retruning}}$ are defined as $\overrightarrow{k_s} - \overrightarrow{k_i}$,

where $\overrightarrow{k_s}$ and $\overrightarrow{k_i}$ are the vector of the wave number of going and returning incident beams respectively. The angle between the local magnetic field and $\Delta\overrightarrow{k_{going}}$ and $\Delta\overrightarrow{k_{retruning}}$ are defined as β_1 equal to 83.9° and β_2 equal to 111.7° respectively.

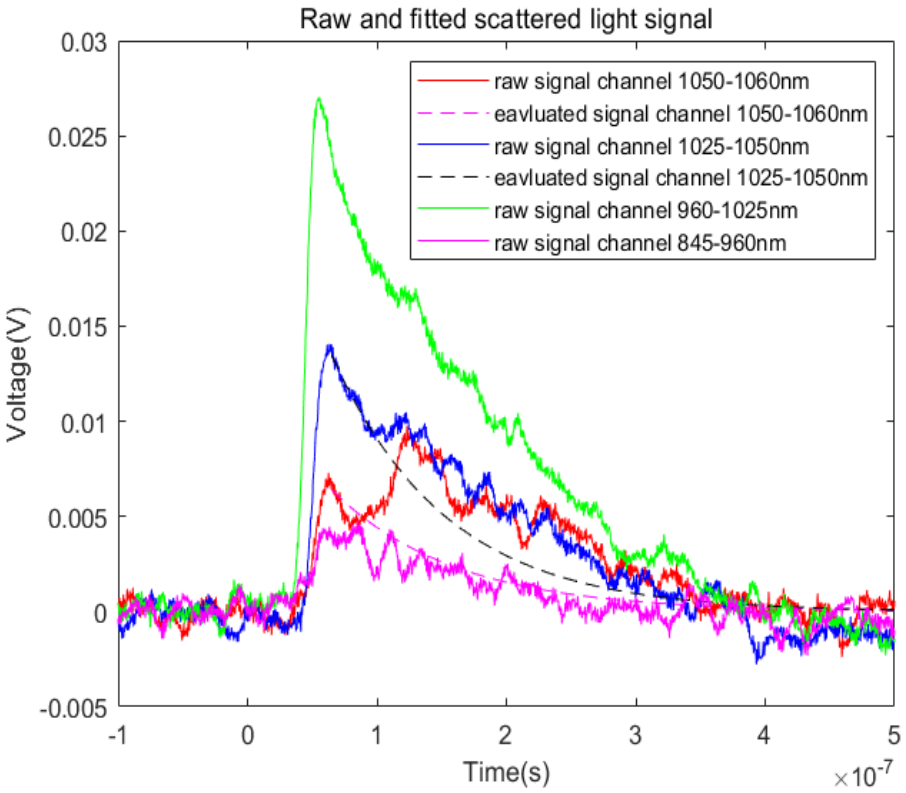

Fig. 6.11: Raw 2-pass signals and fitted signals at 280 ms.

The raw signal of the 2-pass and the fitted signals are shown in Fig. 6.11. It can be seen that the TS signals corresponding to 20° scattering only appear in channel 1050-1060nm and channel 1025-1050nm. The reason is basically two, which is that the T_e is relatively low in this experiment and the spectrum of 20° scattering has a much weaker blue-shift compared with that of 160° scattering.

T_e corresponding to 160° scattering and 20° scattering separately measured at core plasma (r/a~0.26) by the multi-pass system with signal separation system for three timings are shown in Fig. 6.12: t = 280 ms, t = 300 ms, and t = 320 ms with a slightly decreasing

diamagnetic field. The values of $< (T_{e\ 160º} - T_{e\ 20º})/T_{e\ 160º} >$ at 300 ms and 320 ms are 6%±26% and 14%±17% respectively, which does not show obvious isotropic breaking in this experiment.

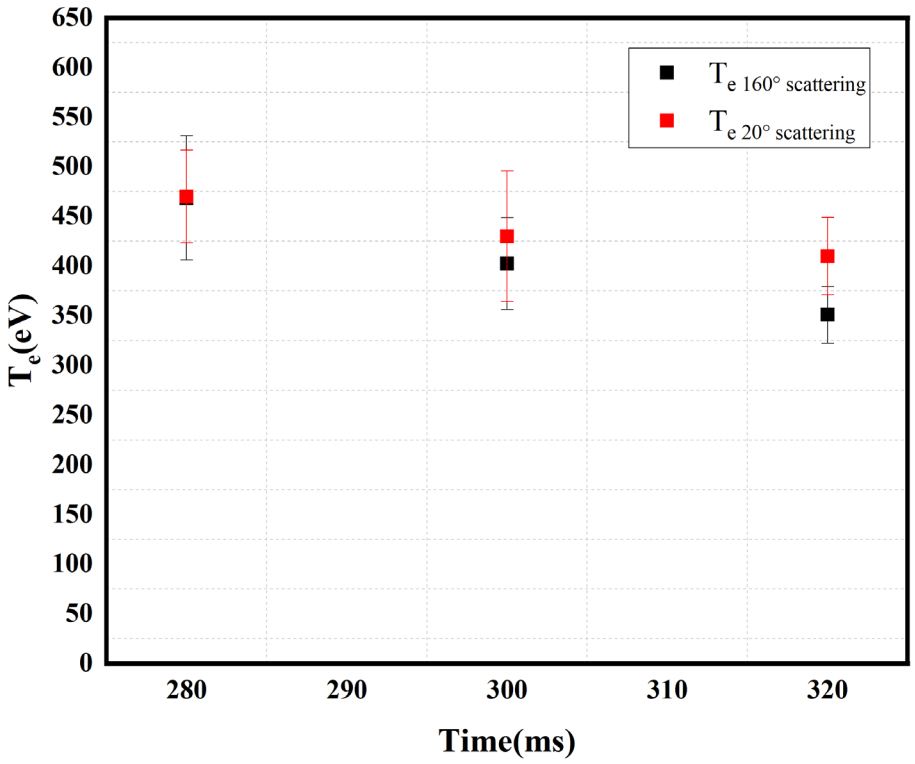

Fig. 6.12: Te anisotropy measurement at 280, 300, and 320 ms.

Conclusions

A design of dual scattering angles multi-pass Thomson scattering system with signal separation function is proposed in this work. This newly proposed system can not only realize the function of traditional multi-pass Thomson scattering systems that the photons produced by one laser shot can be recycled to increase the intensity of scattered light signals but also separate the overlapping scattered light signals corresponding to two adjacent incidences. The performance, including the multi-pass function and the signal separation function, has been confirmed by Raman scattering.

This new MPTS system is constructed based on a Nd:YAG laser Thomson scattering system that can realize T_e and n_e measurements from scattered light produced by the single-pass of a laser beam. Compared with the old system, a polarization optical system, trigger system, and image relay system are added for realizing the multi-pass function and signal separation function. The polarization optical system is used to control the polarization status of the laser beam. In the polarization optical system, compared to the traditional MPTS system where only one Pockels cell is utilized, our new proposed system utilizes two Pockels cells. One Pockels cell is utilized to realize the traditional multi-pass function and another one is used for the signal separation function. The signal separation function realized by the newly added Pockels cell can extend the incident interval between two adjacent incidences with the advantage of a compact optical path so that this design can have a good deal with the layout of MPTS systems in a limited room. The trigger system is used to control the operating period of the two Pockels cells so that they can work at the precision of nano sec level with the laser during plasma discharge in synergy. The image relay systems are utilized to maintain the laser during its propagation in the optical path because the spot size

evolution of the laser is following a Gaussian beam. Because the optical path length of the proposed system is significantly increased, two IRSs are designed to constrain the expansion of the laser spot size within 7 mm during beam propagation and they successfully prevent any damage to the Pockels cell crystal from being caused. Based on the evolution of spot size, the evolution of power density is simulated and the areas where high power density exists are vacuumed to avoid laser-induced breakdown.

Optimization of filter combinations inside the polychromators has been done to improve the measurement accuracy of T_e for analysis of the anisotropy phenomenon. Because the scattering angle significantly determines the shape of the spectrum and the MPTS system on Heliotron J is a dual scattering angles system. The filter combination is optimized for both scattering angles existing in the MPTS system on Heliotron J simultaneously. By applying a 6-filter combination, the T_e measurement error in the newly added 20º scattering angle by upgrading to MPTS is reduced to at least one-half of the error estimated by applying the current 5-filter combination when T_e is lower than 100 eV.

The proposed design of the MPTS system with signal separation function has been constructed on Heliotron J and the system performance has been confirmed. For the multi-pass function, at most 18-pass can be confirmed by a stray light experiment. In a Raman scattering experiment, a 4-pass signal has been observed and the intensity of the 4-pass signal is over 2.5 times larger than the signal produced by a single-pass system. For the signal separation function, compared to a conventional MPTS system without the signal separation function, the incident interval between two adjacent incidences can be extended to 104 ns by a compact optical path with a 6 m length of the optical path by verification of Raman scattering signal. Compared to simply extending the length of the optical path, the layout of the optical path for the MPTS system on Heliotron J can

be significantly optimized by using the proposed system, which realizes an extended incident interval 1.7 times more than the performance of our previous system in a compact optical path layout.

With the newly constructed system, we made the T_e anisotropy measurement in a low-density plasma generated by ECH. The scattered light corresponding to two incidences has been successfully separated for further analysis. The results show that a slight difference between T_e measured by two different scattering angles appeared at the core plasma.

In general, it can be said that based on this design, overlapping signals can be separated by using a compact optical path. The Raman scattering results verify the extended incident interval with the operation of the signal separation system and the fitting error corresponding to the longer incident interval extended by the signal separation system shows a lower error. Additionally, the accuracy of the MPTS system will become more reliable for both scattering angles, which provides more reliability for the investigation of the anisotropic phenomenon. A difference between T_e measured by different scattering angles is observed in an ECH plasma but no obvious isotropic breaking in this experiment.

Acknowledge

First, I would like to express my heartfelt gratitude to my advisor, Associate Professor Takashi Minami, for his unwavering support throughout my Ph.D. study and research. As my supervisors, I have always relied on his guidance and insightful discussions. Without his invaluable support, I would not have been able to complete this dissertation.

I would like to express my sincere gratitude to my advisor Professor Shigeru Inagaki for the continuous support of my Ph.D. study and related research. He gave me a lot of valuable instructions for improving my manuscripts.

I would also like to extend my appreciation to Associate Professor Shinichiro Kado for helping me revise my first paper published during my Ph.D. study and Assistant Professor Naoki Kenmochi for his generous help in discussing with me the detail of the Thomson scattering system on Heliotron J, and Associate Professor Ryo Yasuhara for his valuable advice on the development of the multi-pass Thomson scattering system. My sincere thanks go to Professor Kazunobu Nagasaki, Professor Tohru Mizuuchi, Associate Professor Hiroyuki Okada, Assistant Professor Shinji Kobayashi, Assistant Professor Satoshi Yamamoto, and Assistant Professor Shinsuke Ohshima for their helpful comments and suggestions on this study.

I am grateful to the YAG-TS group in Heliotron J for their tremendous support, including Takashi Nishide, Masahiro Miyoshi, Yutai Yamanaka, Ryo Matsutani, Yusuke Toba, and Ryoga Shinotsuka. My time at Kyoto University was made enjoyable by their presence. I would also like to thank the technical and administrative staff of Heliotron J for their assistance, including T. Senju, Y. Ijiri, K. Yaguchi, K. Tohshi, K. Sakamoto, M. Shibano, K. Kumabe, S. Watanabe, and H. Yokota.

Furthermore, I am grateful to my parents, grandmother, and aunt for their generous financial support throughout my studies. Last but not least, I would like to express my heartfelt appreciation to my wife for her patience and unwavering support during this journey.

Achievements

Published papers

The main parts of this thesis are constructed from the following papers.

Chapter 5:

Qiu D, Minami T, Nishide T, et al. Design of compact multi-path Thomson scattering diagnostic with signal delay system in Heliotron J[J]. Plasma and Fusion Research, 2020, 15: 2401044-2401044.

Qiu D, Minami T, Kado S, et al. Design of a dual scattering angle multi-pass Thomson scattering system with signal separation function on Heliotron J[J]. Review of Scientific Instruments, 2023, 94(1): 013503.

Chapter 6:

Qiu D, Minami T, Kado S, et al. Increased signal separation upgrade permits preliminary electron anisotropy measurements with Heliotron J multi-pass Thomson diagnostic[J]. Review of Scientific Instruments, 2023, 94(2).

The following papers are irrelevant to the main parts of this thesis but with contribution of the author.

1. Minami T, Qiu D, Nishide T, et al. Current status and plan of development of Nd: YAG laser Thomson scattering system in Heliotron J[J]. Journal of Instrumentation, 2020, 15(02): C02011.

2. P. Zhang, S. Ohshima, H. Zhao, C. Deng, S. Kobayashi, S. Kado, T. Minami, R. Matoike, A. Miyashita, A. Iwata, Y.Kondo, D. Qiu, C. Wang, M. Luo, S. Konoshima, S.Inagaki, H. Okada, T. Mizuuchi, K. Nagasaki. “Development and initial results of 320 GHz interferometer system in Heliotron J”, Review of Scientific Instruments, 93(11) (2022).

3. P. Zhang, S. Ohshima, H. Zhao, S. Kobayashi, S. Kado, T. Minami, F. Kin, A. Miyashita, A. Iwata, Y.Kondo, D. Qiu, C. Wang, M. Luo, S. Konoshima, S.Inagaki, H. Okada, T. Mizuuchi, K. Nagasaki. “Characterization of a retroreflector array for 320-GHz interferometer system in Heliotron J” Accepted by Review of Scientific Instruments.

4. S. Ohshima, P. Zhang, H. Kume, C. Deng, A. Miyashita, S. Kobayashi, H. Okada, T. Minami, S. Kado, P. Adulsiriswad, D. Qiu, M. Luo, R. Matoike, T. Suzuki, S. Konoshima, T. Mizuuchi, and K.Nagasaki. “Development of a multi-channel 320 GHz interferometer for high density plasma measurement in Heliotron J”, Review of Scientific Instruments, 92(5) (2021).

5. S. Ohshima, T. Suzuki, R. Matoike , G. Motojima, S. Kado, A. Mori , A. Miyashita , S. Kobayashi , T. Minami , A. Iwata , D. Qiu , C. Wang , M. Luo , P. Zhang , Y. Kondo , N. Nishino , T. Mizuuchi, H. Okada, S. Konoshima , S. Inagaki & K. Nagasaki. “Three-dimensional dynamics of fuctuations appearing during pellet ablation process around a pellet in a fusion plasma experiment”, Scientific Reports, 2022,12(1), 14204.

Participated conferences

2019:

28th International Toki Conference(ITC-28), Poster session.

2020:

4th Asia-Pacific Conference on Plasma Physics, Poster session.

2021:

第 12 回エネルギー理工学研究所国際シンポジウム, Poster session.

2022:

High-Temperature Plasma Diagnostics Conference 2022, Poster session.

第 14 回核融合エネルギー連合講演会, Poster session.

プラズマ・核融合学会 第 39 回年会, Oral session.

Reference

1. Stacey Jr, W. M. Fusion plasma analysis. (1981).
2. Chen, F. F. & others. *Introduction to plasma physics and controlled fusion*. vol. 1 (Springer, 1984).
3. Wesson, J. & Campbell, D. J. *Tokamaks*. vol. 149 (Oxford university press, 2011).
4. Bowden, M. D. *et al.* Thomson scattering measurements of electron temperature and density in an electron cyclotron resonance plasma. *J. Appl. Phys.* **73**, 2732–2738 (1993).
5. Kantor, M. Yu. & Kuprienko, D. V. Laser multipass probing in Thomson plasma diagnostics. *Tech. Phys. Lett.* **23**, 321–323 (1997).
6. Kantor, M. Y., Donné, A. J. H., Jaspers, R., Van Der Meiden, H. J., & TEXTOR Team. Thomson scattering system on the TEXTOR tokamak using a multi-pass laser beam configuration. *Plasma Phys. Control. Fusion* **51**, 055002 (2009).
7. Kantor, M. Yu. & Kouprienko, D. V. High repetition rate probing laser for Thomson scattering diagnostics. *Rev. Sci. Instrum.* **70**, 780–782 (1999).
8. Hiratsuka, J., Ejiri, A., Takase, Y. & Yamaguchi, T. Feasibility of a Multi-Pass Thomson Scattering System with Confocal Spherical Mirrors. *Plasma Fusion Res.* **5**, 044–044 (2010).
9. Hiratsuka, J. *et al.* Development of a Double-Pass Thomson Scattering System in the TST-2 Spherical Tokamak. *Plasma Fusion Res.* **6**, 1202133–1202133 (2011).

10. Hiratsuka, J. *et al.* Off-Axis Temperature Anisotropy Measurement by Double-Pass Thomson Scattering Diagnostic System on TST-2. *Plasma Fusion Res.* **7**, 2402092–2402092 (2012).

11. Hiratsuka, J. *et al.* Simultaneous Measurement of Plasma Pressure Anisotropy with a Double-Pass Thomson Scattering Diagnostic System on the TST-2. *Plasma Fusion Res.* **10**, 1402007–1402007 (2015).

12. Togashi, H. *et al.* Note: Multi-pass Thomson scattering measurement on the TST-2 spherical tokamak. *Rev. Sci. Instrum.* **85**, 056103 (2014).

13. Togashi, H. *et al.* Demonstration of improvement in the signal-to-noise ratio of Thomson scattering signal obtained by using a multi-pass optical cavity on the Tokyo Spherical Tokamak-2. *Rev. Sci. Instrum.* **85**, 11D846 (2014).

14. Hatae, T., Nakatsuka, M. & Yoshida, H. Improvement of Thomson Scattering Diagnostics Using Stimulated-Brillouin-Scattering-Based Phase Conjugate Mirrors. *J. Plasma Fusion Res.* **80**, 870–882 (2004).

15. Hatae, T., Naito, O., Nakatsuka, M. & Yoshida, H. Applications of phase conjugate mirror to Thomson scattering diagnostics (invited). *Rev. Sci. Instrum.* **77**, 10E508 (2006).

16. Yasuhara, R. *et al.* Design of the polarization multi-pass Thomson scattering system. *Rev. Sci. Instrum.* **83**, 10E326 (2012).

17. Yoshikawa, M. *et al.* Development of polarization-controlled multi-pass Thomson scattering system in the GAMMA 10 tandem mirror. *Rev. Sci. Instrum.* **83**, 10E333 (2012).

18. Yoshikawa, M. *et al.* First results of electron temperature measurements by the use of multi-pass Thomson scattering system in GAMMA 10. *Rev. Sci. Instrum.* **85**, 11D801 (2014).

19. Yoshikawa, M. *et al.* Improvement in multipass Thomson scattering system comprising laser amplification system developed in GAMMA 10/PDX. *Rev. Sci. Instrum.* **92**, 033515 (2021).

20. Minami, T. *et al.* Design of a new high repetition rate Nd:YAG Thomson scattering system for Heliotron Ja). *Rev Sci Instrum* (2014).

21. Fujisawa 等 - 1998 - Discovery of Electric Pulsation in a Toroidal Heli.pdf.

22. Kenmochi, N. *et al.* Characteristics of electron internal transport barrier in Heliotron J. *Plasma Phys. Control. Fusion* **59**, 055013 (2017).

23. Wagner, F. Topics in toroidal confinement. *Plasma Phys. Control. Fusion* **39**, A23 (1997).

24. Fujiwara, M. *et al.* Overview of LHD experiments. *Nucl. Fusion* **41**, 1355 (2001).

25. Iiyoshi, A. & Wakatani, M. Heliotron E Results and Large Helical Project. *J. Nucl. Sci. Technol.* **26**, 204–208 (1989).

26. Fumimichi, S. *et al.* Experimental Program of Heliotron J.

27. Wakatani, M. & Sudo, S. Overview of Heliotron E results. *Plasma Phys. Control. Fusion* **38**, 937 (1996).

28. Obiki, T. *et al.* Goals and status of Heliotron J. *Plasma Phys. Control. Fusion* **42**, 1151 (2000).

29. Mizuuchi, T. *et al.* Edge fluctuation studies in Heliotron J. *J. Nucl. Mater.* **337–339**, 332–336 (2005).

30. Sano, F. *et al.* H-mode confinement of Heliotron J. *Nucl. Fusion* **45**, 1557 (2005).

31. Sano, F. *et al.* Observation of H-Mode Operation Windows for ECH Plasmas in Heliotron J. *Fusion Sci. Technol.* **46**, 288–298 (2004).

32. Shidara, H. *et al.* A 70-GHz Electron Cyclotron Resonance Heating System for Heliotron J. *Fusion Sci. Technol.* **45**, 41–48 (2004).

33. Zang, L. G. *et al.* Observation of a beam-driven low-frequency mode in Heliotron J. *Nucl. Fusion* **59**, 056001 (2019).

34. Kobayashi, S. *et al.* Plasma startup using neutral beam injection assisted by 2.45 GHz microwaves in Heliotron J. *Nucl. Fusion* **51**, 062002 (2011).

35. Okada, H. *et al.* Configuration Control Experiment in Heliotron J. (2008).

36. Zhang, P. *et al.* Development and initial results of 320 GHz interferometer system in Heliotron J. *Rev. Sci. Instrum.* **93**, 113519 (2022).

37. Ohshima, S. *et al.* Development of a multi-channel 320 GHz interferometer for high density plasma measurement in Heliotron J. *Rev. Sci. Instrum.* **92**, 053519 (2021).

38. Luo, M. *et al.* Measurement of Electron Temperature Profile and Fluctuation with ECE Radiometer System in Heliotron J. *Plasma Fusion Res.* **15**, 2402038–2402038 (2020).

39. Kenmochi, N. *et al.* First measurement of time evolution of electron temperature profiles with Nd:YAG Thomson scattering system on Heliotron J. *Rev. Sci. Instrum.* **85**, 11D819 (2014).

40. Hutchinson, I. H. Principles of plasma diagnostics. *Plasma Phys. Control. Fusion* **44**, 2603–2603 (2002).

41. Currie, W. M. Elementary Nuclear Physics. (1965).

42. Pechacek, R. E. & Trivelpiece, A. W. Electromagnetic Wave Scattering from a High-Temperature Plasma. *Phys. Fluids* **10**, 1688–1696 (1967).

43. The incoherent scattering of radiation from a high temperature plasma - IOPscience. https://iopscience.iop.org/article/10.1088/0032-1028/14/8/003/meta.

44. Lorrain, P. & Corson, D. R. Electromagnetic fields and waves. (1970).

45. Jackson, J. D. Classical electrodynamics. (1999).

46. Heald, M. A. & Marion, J. B. *Classical Electromagnetic Radiation*. (Courier Corporation, 2012).

47. Reitz, F. J., Milford, J. R. & Christy, R. D. *Foundations of Electromagnetic Teory*. (2003).

48. Prunty, S. L. A primer on the theory of Thomson scattering for high-temperature fusion plasmas. *Phys. Scr.* **89**, 128001 (2014).

49. Rosser, W. G. V. An introduction to the theory of relativity. (1964).

50. Beausang, K. The consistency of electron temperature measurements by Thomson scattering at the JET tokamak.

51. Froula, D. H. *Plasma scattering of electromagnetic radiation: theory and measurement techniques*. (Academic Press, 2011).

52. Salpeter, E. E. Electron Density Fluctuations in a Plasma. *Phys. Rev.* **120**, 1528–1535 (1960).

53. Naito, O., Yoshida, H. & Matoba, T. Analytic formula for fully relativistic Thomson scattering spectrum. *Phys. Fluids B Plasma Phys.* **5**, 4256–4258 (1993).

54. Matoba, T., Itagaki, T., Yamauchi, T. & Funahashi, A. Analytical Approximations in the Theory of Relativistic Thomson Scattering for High Temperature Fusion Plasma. *Jpn. J. Appl. Phys.* **18**, 1127–1133 (1979).

55. Lynch, C. P. A. LIDAR Incoherent Thomson Scattering at Relativistic Velocities.

56. Kukushkin, A. B. Incoherent scattering of light by a finite volume of relativistic plasma. **7**, 110–118 (1981).

57. Fujisawa, A. *et al.* Discovery of Electric Pulsation in a Toroidal Helical Plasma. *Phys. Rev. Lett.* **81**, 2256–2259 (1998).

58. Obiki, T. *et al.* First plasmas in Heliotron J. *Nucl. Fusion* **41**, 833 (2001).

59. Kenmochi, N. *et al.* Development of a Laser Timing Controller for the High Time-Resolution Nd:YAG Thomson Scattering System in Heliotron J. *Plasma Fusion Res.* **8**, 2402117–2402117 (2013).

60. Minami, T. *et al.* Present Status of the Nd:YAG Thomson Scattering System Development for Time Evolution Measurement of Plasma Profile on Heliotron J. *Plasma Sci. Technol.* **15**, 240–243 (2013).

61. Minami, T. *et al.* Current status and plan of development of Nd:YAG laser Thomson scattering system in Heliotron J. *J. Instrum.* **15**, C02011–C02011 (2020).

62. Hecht, E. *Optics*. (Pearson Education, Inc, 2017).

63. Yatsuka, E., Hatae, T. & Kusama, Y. Principles for local measurement of anisotropic electron temperature of plasma using incoherent Thomson scattering. *Nucl. Fusion* **51**, 123004 (2011).

64. Sano, F. *et al.* H-mode confinement of Heliotron J. *Nucl. Fusion* **45**, 1557 (2005).

65. Kajita, S., Hatae, T. & Naito, O. Optimization of optical filters for ITER edge Thomson scattering diagnostics. *Fusion Eng. Des.* **84**, 2214–2220 (2009).

66. Kajita, S., Hatae, T. & Kusama, Y. Design study of polychromators for ITER edge Thomson scattering diagnostics. *Rev. Sci. Instrum.* **79**, 10E726 (2008).

67. McIntyre, R. J. Multiplication noise in uniform avalanche diodes. *IEEE Trans. Electron Devices* **ED-13**, 164–168 (1966).

68. Avalanche Photodiode: A User Guide.

69. s8890_series_kapd1010e.pdf.